Observation of a Persistent Non-Equilibrium State in an Extremely Isotropic Harmonic Potential

by

D. S. Lobser

B.A., University of Colorado, Boulder, 2009

M.S., University of Colorado, Boulder, 2012

A thesis submitted to the
Faculty of the Graduate School of the
University of Colorado in partial fulfillment
of the requirements for the degree of
Doctor of Philosophy
Department of Physics
2015

This thesis entitled:
Observation of a Persistent Non-Equilibrium State in an Extremely Isotropic Harmonic Potential
written by D. S. Lobser
has been approved for the Department of Physics

Eric A. Cornell

Heather J. Lewandowski

Date

The final copy of this thesis has been examined by the signatories, and we find that both the content and the form meet acceptable presentation standards of scholarly work in the above mentioned discipline.

Lobser, D. S. (Ph.D., Physics)

Observation of a Persistent Non-Equilibrium State in an Extremely Isotropic Harmonic Potential

Thesis directed by Prof. Eric A. Cornell

Ludwig Boltzmann made tremendously important contributions to the problem of connecting macroscopic, empirical phenomena with microscopic, atomistic dynamics. At the end of the nineteenth century, Boltzmann was confronted with various strong objections to his work. For example, Boltzmann's atomistic explanations presuppose the reality of atoms, a notion that was vigorously rejected in some circles [14, 38]. Then too, there was the critique by Loschmidt that Boltzmann's H-theorem, put forth as a microscopic explanation for the Second Law of Thermodynamics, could hardly account for irreversible physics when the individual two-atom collisions were each reversible [18, 42]. Still intriguing today is the existence of special cases of the Boltzmann equation in which time-varying distributions of atoms resist the imperative of equilibration, even in the presence of collisions. Boltzmann discussed such situations in a paper dedicated to responding to Loschmidt's critique [7, 4]. Perhaps Boltzmann's motivation was to enumerate special cases where his famous H value does not relax as it should, and by enumerating them, point out their nonnaturalness, their artificiality. Damping, or relaxation to equilibrium, of a time-invariant phase-space distribution, is an all-but universal result predicted by the Boltzmann equation.

Such improbable systems of atoms have only very recently been realized experimentally. Kinoshita et al. [36] experimentally confirmed that atoms constrained to move in a quasi one-dimensional potential, an atomistic Newtons cradle, exhibit vastly suppressed relaxation. Chevy et al. [15] observed long-lived breathe-mode oscillations in highly elongated but still 3D geometries. Perhaps one of the more interesting cases is the vanishing damping of the monopole breathe-mode oscillation in a spherically symmetric harmonic oscillator [29], where a cloud of atoms experiences undamped temperature oscillations, causing the cloud to expand and contract as if it were breathing. Until now, this phenomenon has been experimentally inaccessible due to the difficulty in generating isotropic harmonic confinement. This thesis discusses a new magnetic trap capable of producing spherical confinement and presents the first experimental realization of this historically significant oddity using a magnetically trapped gas of ^{87}Rb atoms.

Dedication

To my family.

Acknowledgements

First and foremost I want to thank my family for their constant support. Regardless of what I was interested in when I was growing up, my family always did whatever they could to support me. Mom's enthusiasm and positive outlook is infectious. She never takes no for an answer and always finds a way to accomplish something once she sets her mind to it. When I wanted to try fencing, she did a bunch of research and found the best place to go for fencing lessons and drove me across town a few times a week for years so that I could get the best training around. When I got into photography, she helped me enroll in the best photography class in the area so I could have access to one of the few color dark rooms in the state. If it wasn't for her, I wouldn't have experienced so many of the things that have defined who I am today, and I'd still probably be working at a restaurant! Dad's excitement about math and programming was invaluable when I was growing up. He would always challenge me with problems and surprise me with the simplicity of his solutions to them. Often, he told me that you only really understand how something works if you can program a computer to solve it. I remember getting my first graphing calculator in middle school, a TI-86, and asking him what the PRGM button was. Of course, I got a long winded answer that I didn't really care about. But then he had me write a program and helped me line by line. The goal was to calculate the prime factors of an arbitrary number. He'd let me struggle through it for a while, then he'd look at the program and tell me where I'd gone wrong and why and suggest a better alternative until later that night when I finally had a working program. You could put in a number and it would slowly churn out one prime

factor at a time until it finished. I remember thinking it was a great program because it took so long, which *must* have meant that it was solving a very difficult problem. After that I started moving on to other problems and soon forgot about that first program. But a few years later I discovered that the very same program was being used by a lot of students at the nearby high school to cheat on their tests (I knew this because I heard people referencing my program by it's unfortunate and arbitrary name "BBB"). Looking back on that first programming experience, I couldn't have chosen a better problem to solve. Ironically, the first algorithm to fully takes advantage of a quantum computer is Schor's algorithm for computing the prime factors of a number. A concept which is extremely relevant for my transition into quantum information research! I also have my brother—David even made some of the figures in this thesis—and sister to thank, as well as my aunts, uncles, cousins, and grandparents, who've all been so supportive over the years.

I've worked with a number of great students during my 10 years at JILA. Paul Parazzoli always set time aside to help me out with problems when I was an undergrad, and I'm looking forward to working with him again during my postdoc. Along with Noah Fitch and Carrie Weidner, I think we made an excellent team and I couldn't ask for a better first group of people to work with in the lab. Shih-Kuang Tung was a great student and gave me a lot of advice while he taught me about the TOP trap and many of the details of the experiment. It was a pleasure working in the lab next door to the EDM group over the years. I'll miss all the interesting things Matt Grau used to mention to me, and I have him to thank for my learning about the Julia language. I also want to thank Brandon Ruzic for putting up with me these last couple months. And the same goes for Cam and Victor, who've been very helpful and patient with my getting them data. It has been a pleasure hanging out with so many people in my class and I'm confident that they will all go on to be very successful.

Finally, I consider myself extremely lucky to have had such great advisors over the last 10 years. As an undergraduate, I worked for Prof. Heather Lewandowski. When I started, Heather didn't have any lab space and I was building electronics out of her office. This gave me the chance to see how a lab is put together from the ground up, especially since the lab was converted from an office! Heather has been instrumental, even during my graduate career, in my understanding and approach to experimental systems. Her knowledge and insight, as well as her ability to impart that knowledge, has given me a strong foundation that helped immensely in my graduate work. Heather treats her students with a great deal of respect. Even when I was an undergraduate, who wasn't yet well-versed in the technical aspects of the experiment, she encouraged me to participate in troubleshooting difficult problems with her and the other graduate students on the experiment. My input was treated seriously, and, even if I wasn't always able to contribute, it was during these times that I learned the most.

Eric never ceases to amaze me with his incredible approach to physics. His ideas and way of looking at problems extremely are inspiring, which never fails to give me a new perspective and a renewed excitement about science. Working on this experiment was a totally different experience from my undergraduate work. The experiment was well established and had been for well over decade, but working on a mature experiment also has its difficulties. Approaching problems on the TOP trap made me think about problems in a new way, and often involved repurposing some preexisting hardware for an entirely different task. Eric's creativity and his ability to turn a difficult problem on its side introduced me to an entirely new and invaluable skill set that I will continue to use in all aspects of my life. I greatly admire his tact and his wisdom and will look back on these years with fond memories.

Contents

Chapter

Appendix

Tables

Table

Figures

Figure

Chapter 1

Introduction

The notion of irreversibility in nature is a concept that is ingrained in us from a very early age. Nobody expects the cream in their coffee to suddenly separate and move to one side of the mug, or for their coffee to get hotter as it sits. If, however, the cream were to separate from the coffee or if its temperature were to spontaneously increase, no physical laws would be violated. We now know that it's really the *probability* of cream completely separating from coffee that is so small it is *effectively* an impossibility. But it wasn't until the late 19th century that Ludwig Boltzmann formulated a rigorous explanation of irreversible processes as time-reversible dynamics in a statistical framework. Boltzmann made various contributions to physics, but he was truly interested in understanding the macroscopic phenomena described by thermodynamics at the microscopic level, to which he made monumental advances. By 1872, he formulated his transport equation, which describes how the phase-space distribution of a gas evolves in time as a function of individual particle collisions. Using his transport equation, more commonly referred to as the Boltzmann equation, he derived the H-theorem, which he put forth as a description of the Second Law of thermodynamics. While nothing about this approach seems especially problematic today, his theory met with a great deal of skepticism and, in some cases, was even viciously opposed. For example, Boltzmann assumed the existence of atoms, which were not yet fully accepted by the scientific community. But the objections against Boltzmann's theory hinged primarily on two arguments. First, the notion of a mechanistic description of the way a gas approaches equilibrium was considered to be fundamentally flawed because the time reversal symmetry of mechanical systems conflicted with the irreversible nature of entropy. Second, mechanical systems undergoing elastic collisions will eventually return to their initial state. These two arguments are usually called the "reversibility" and "recurrence" objections respectively. The recurrence objection was spurred on by Henri Poincaré and his assistant, Ernst Zermelo, but included various other scientists, mathematicians, and philosophers even including Friedrich Nietzsche, who first pointed out the paradox [19]. Heated arguments about the recurrence objection spanned nearly two decades and were often punctuated with sharply worded, deep cutting comments from both sides. Unfortunately, the debate was never resolved[1] and ultimately died out with the people involved. The recurrence objection has a much more colorful history than the reversibility objection, but it was the reversibility objection that lead to the result of this thesis.

Joseph Loschmidt, a friend and colleague of Boltzmann, is attributed with development of the reversibility objection, however this argument had been made by William Thomson in 1874 [4] and was essentially what Maxwell was trying to motivate with his demon analogy [4, 38]. Loschmidt's criticism was not directed at Boltzmann, but simply pointed out the problem with using a statistical distribution of microstates in a gas as a means of describing thermodynamic phenomena. He argued that there are certain arrangements of atoms in a vessel that were inconsistent with the barometric law, which states that if the vessel is divided into vertically stacked layers then the mean energy of each layer must be the same. Suppose a single atom is placed at the top of the vessel and the rest of the atoms are at rest at the bottom of the vessel, as shown in Fig. 1.1. The atom at the top will eventually fall to the bottom and its kinetic energy will be distributed amongst the other atoms. For very large numbers of atoms, it is very likely that an atom will never be found in the top layer at a later time because all of the atoms must come to rest at the bottom again. However,

---

[1] Boltzmann's ideas are now widely accepted, but it the people involved in the original debate died before reaching an agreement.

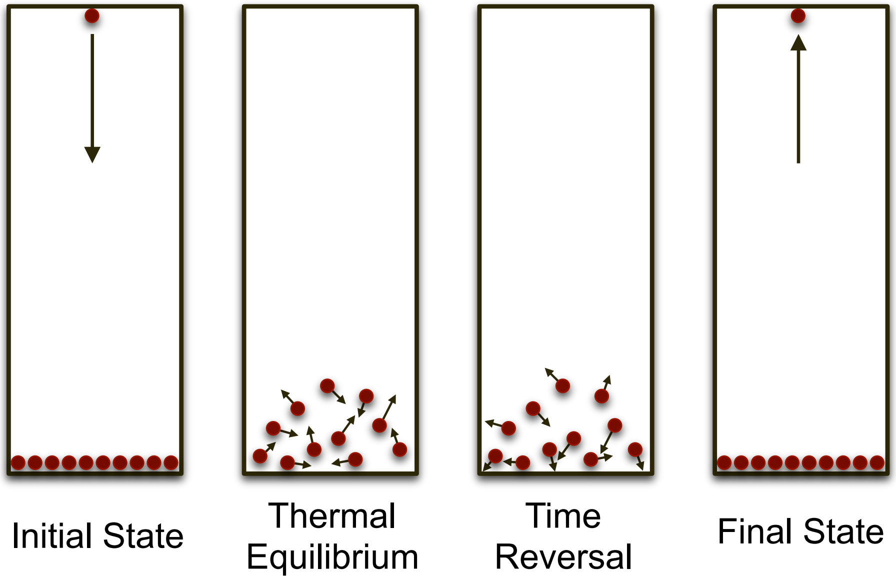

Figure 1.1: Diagram representing Loschmidt's argument about how time-reversal symmetry can lead to unlikely results. Initially, all of the atoms are at rest at the bottom of a vessel with the exception of a single atom placed at the very top of the vessel. The atom at the top of the vessel will fall to the bottom, colliding with other atoms. Eventually, the energy from the dropped atom will distribute to all of the other atoms and they will reach a state of equilibrium. By reversing time, the time-reversal symmetry inherent to mechanical systems implies that the atoms will approach their initial state with one atom at the very top of the vessel and all of the other atoms resting at the bottom. Loschmidt's argument was that an equilibrium distribution could thus be constructed in such a way that, as time advances, the distribution will approach the unlikely state used in his example. Because entropy was observed to have no time-reversal symmetry, Loschmidt claimed that the mechanical arguments used by Boltzmann to describe how a gas approaches equilibrium were flawed.

Loschmidt argued that [4]

> If, after a sufficient time τ is elapsed from the establishment of the stationary state, we suddenly turn the velocities of all atoms in the opposite directions, then we will find ourselves at the beginning of a state to which the character of stationarity can apparently be ascribed. This would last for a certain time, but then the stationary state would start gradually to deteriorate and after a time we would arrive unavoidably again at our initial state.

While Loschmidt's argument wasn't directed at Boltzmann, it did suggest that Maxwell's distribution could not sufficiently describe states in equilibrium because special arrangements of the microstates in the distribution could be constructed to drive the system out of equilibrium and hence the system wasn't necessarily stationary. At the time, the laws of thermodynamics were considered to be absolute and could not be violated. This posed serious problems for kinetic theory, which allowed for deviations from thermodynamics in special cases. Boltzmann had been aware of these anomalies as early as 1868, when he showed that a gas initially constrained to lie in one dimension would never reach a homogeneous isotropic distribution. He published an article in response to Loschmidt's reversibility argument, which cited the 1868 example, but also derived a number of other special cases that exhibited bizarre behavior [7]. Originally, Boltzmann had sidestepped the issue, claiming that the bizarre behavior that arose from extremely artificial initial conditions was characteristically unnatural. Deeming these cases impossible in the limit of extremely large atom number, he ignored them because they would never occur in a real system. This sentiment was shared by Thomson in his 1874 paper [58]:

> ...the greater the number of molecules, the shorter will be the time during which the disequalizing will continue; and it is only when we regard the number of molecules as practically infinite that we can regard spontaneous disequalization as practically impossible.

Despite Boltzmann's awareness of the unusual behavior potentially exhibited by these artifically cooked-up systems, he eventually conceded that his theories were invalid in these highly improbable cases and, thereafter, parenthetically stipulated that the Second Law "can be mechanically represented only by means of assumptions regarding initial conditions" [14]. Loschmidt's argument did eventually cause Boltzmann to approach the problem differently, and in 1877 he published a paper that used a purely combinatorial approach. There are still two schools of thought regarding Boltzmann's viewpoint during the development of kinetic theory. Many argue that his 1876 and 1877 papers marked a sudden realization that his original formulation of the H-theorem was not only incomplete, but incongruent with his combinatorial approach. However, his 1877 paper did not refute any ideas from his original formulation, but instead carefully laid out the probabilistic framework on which the transport equation was based. This is also evidenced by a reference to his 1876 paper in his *Lectures on Gas Theory*, which was published 20 years later:

> Other solutions of these equations, in which t can also occur explicitly, can also be found [7]. For example, there is one remarkable solution in which the gas flies outward from a center equally in all directions in such a manner that, first, there is no viscosity; and second, while the temperature of course drops as a result of the expansion, it drops equally everywhere in space so that no heat conduction occurs. We shall no longer concern ourselves with these matters, however; we shall only ask what value the quantity H has in all these cases.

He then goes on to show that entropy is constant in cases where the gas is in motion, but satisfies the conditions for equilibrium in his transport equation while resisting the imperative of equilibration. One such case is exhibited by the absence of damping of the monopole, or "breathe," mode of a gas in which the cloud continually expands and contracts as if it were breathing. The condition for this exceptional behavior of the breathe mode is that the gas be confined to an external potential that is both isotropic and harmonic.

Variations of this effect have been experimentally verified in other dimensionalities. Kinoshita et al. [36] experimentally confirmed that atoms constrained to move in a quasi one-dimensional potential, an atomistic Newtons cradle, exhibit vastly suppressed relaxation. Chevy et al. [15] observed long-lived breathe-mode oscillations in highly elongated, but still 3D, geometries. However, the difficulty in generating an isotropic harmonic potential has prevented the experimental verification of the spherical case until now.

1.0.1 Thesis Layout

The purpose of this thesis is to present experimental confirmation of Boltzmann's very old, yet remarkable, result. Because the foundation of the result led to over three decades of heated debates, the foundation of the theory will be laid out carefully in chapter 2. Chapter 3 will give a detailed description and analysis of the magnetic trap, which finally made the experimental realization of this effect possible. In chapter 4, various other details of the experiment will be covered. Chapter 5 presents the results of our experiment on Boltzmann's original prediction. Chapter 6 will briefly describe some of our extensions of these studies to Bose-Einstein Condensates. And Chapter 7 discusses another technique altogether, which is used to spatially separate a series of quasi-2D condensates confined to a 1D optical lattice.

Chapter 2

Theoretical Background

Perhaps Boltzmann's greatest achievement was connecting microscopic, atomistic dynamics to macroscopic empirical phenomena. His ideas helped establish the foundations of kinetic theory, despite the initial resistance of various skeptical opponents of his theories [4, 19, 42]. One of the more fundamental ideas that Boltzmann developed is known as the transport equation, or often simply as the Boltzmann equation, which describes how a gas evolves as a function of collisions between particles in the gas. Boltzmann was intrigued by Maxwell's distribution, which describes the distribution of velocities in a gas at thermal equilibrium. But he was particularly interested in understanding how the complex and chaotic behavior of atoms in a gas could lead to a stable solution, even when atoms are constantly colliding and changing velocities [38]. His idea was that if he could keep track of the motion of each atom and each collision, he could demonstrate how the bulk system would invariably approach the Maxwell distribution. By 1865, Loschmidt had determined the average size of molecules and effectively calculated Avogadro's constant [11]. So Boltzmann was well aware that even a small volume of gas contained an immense number of atoms and keeping track of their individual motions was impossible, and tackling such a problem would require statistical methods. From Boltzmann's perspective, the statistical framework was just a convenient mathematical tool that allowed the calculation of such a complicated and random system managable. Ironically, it wasn't until later that he realized the implications of the statistical framework to the underlying physics.

The statistics used in the Boltzmann equation show up in the form of a phase-space distribution, which is used to describe the arrangement of particles in a gas. The distribution function, $f(\mathbf{r}, \mathbf{v}, t)$, represents the probability density of finding a particle centered about a given region of phase space at time t. This discussion will assume that the distribution is for a single particle and is normalized so that

$$\int f(\mathbf{r}, \mathbf{v}, t) d^3r d^3v = 1, \tag{2.1}$$

where the integral is carried out over the entire phase space. Standard literature on kinetic theory will often use momentum instead of velocity as a phase-space coordinate. For a monatomic gas, the difference amounts to a different normalization constant and the two quantities can more or less be interchanged. In the absence of collisions, the phase space distribution of a gas will remain constant and

$$\frac{df}{dt} = 0. \tag{2.2}$$

Because f is a function of more than one variable, the total derivative can be expanded so that

$$\frac{df}{dt} = \frac{\partial f}{\partial t} + \mathbf{v} \cdot \nabla_{\mathbf{r}} f + \frac{\mathbf{F}}{m} \cdot \nabla_{\mathbf{v}} f = 0, \tag{2.3}$$

where $\mathbf{F}$ is an external force and m is the atomic mass. Eq. (2.3) is the single particle equivalent of the Liouville equation, which states that the phase-space density of a system of non-interacting particles is conserved.

Boltzmann's goal was to describe how a gas would approach equilibrium based on collisional processes. Thus Eq. (2.3) must incorporate another term to account for collisions, resulting in the Boltzmann equation:

$$\frac{df}{dt} = I_{coll}[f]. \tag{2.4}$$

The left side gives the time evolution of the distribution and the right side accounts for any changes to f due to collisions, as described by the "collision integral" $I_{coll}[f]$. Detailed treatments of the collision integral can be found in various textbooks [9, 13, 33, 47, 62], but because the equation is so fundamental to the topic of this thesis it will be briefly discussed here.

For now, it is convenient to represent Eq. (2.4) in the following form

$$I_{coll}[f] = \left(\frac{\partial f}{\partial t}\right)_{coll} = \left(\frac{\partial f}{\partial t}\right)^{+}_{coll} - \left(\frac{\partial f}{\partial t}\right)^{-}_{coll}. \tag{2.5}$$

The last terms are used to explicitly distinguish between entering and leaving[1] scattering events, which respectively increase or decrease f in a particular region of phase-space.

The following assumptions are made about collisions:

- Only binary collisions are considered, which falls under the assumption that the gas is sufficiently dilute.
- Collisions are local and instantaneous.
- The atoms lack any internal structure so that collisions are elastic.[2]
- Velocities of two atoms directly before and after a collision are uncorrelated, but do satisfy conservation of energy and momentum.

Boltzmann called this last assumption “Stosszahlansatz”, now known as the *molecular chaos hypothesis*, which is a necessary ingredient for deriving the irreversible kinetic equation [47].

Binary collisions are often treated as the scattering of particles from a fixed center of force. The parameters of the collision are characterized by two scattering angles, θ and ϕ, and an impact parameter, b, which is the shortest possible distance between the center of mass of both particles if no collision occurs [23, 59]. Exact knowledge of the parameters of

---

[1] The term “entering” refers to scattering events, which result in a final distribution that increases at a particular phase-space coordinate, while the “leaving” terms lead to a decrease in the distribution at the same phase-space coordinate.

[2] Boltzmann’s treatment of this problem preceded the development of quantum mechanics and this argument implied that atoms could be treated as hard spheres. A modern interpretation of this assumption is that collisions have low enough energy that the internal structure in the atoms is inaccessible in this energy regime.

the collision is impossible in a statistical framework, which necessitates that the collisions be described by a differential cross section $\sigma(\Omega)d\Omega$. For a beam of particles incident on the force center, the rate of at which particles are scattered into a solid angle element $d\Omega$ is given by

$$R_0\sigma(\Omega)d\Omega \tag{2.6}$$

where R_0 is the incident particle flux. Consider a particle with a given phase-space coordinate $\mathbf{r}$ and $\mathbf{v}$. Using the associated statistical representation, the existence of a single particle at this coordinate implies

$$\int f(\mathbf{r}', \mathbf{v}', t)\delta(\mathbf{r} - \mathbf{r}')\delta(\mathbf{v} - \mathbf{v}')d\mathbf{r}'d\mathbf{v}' = 1, \tag{2.7}$$

where the shorthand notation $d\mathbf{r}'d\mathbf{v}'$ is equivalent to the notation $d^3r'd^3v'$ used in Eq. (2.1). The incident flux depends on the phase-space density at $\mathbf{r}$ and $\mathbf{v}$ as well as the velocity of the incoming particles, $\mathbf{v}'$:

$$R_0 = f(\mathbf{r}, \mathbf{v}_1, t)\left|\mathbf{v} - \mathbf{v}_1\right| d\mathbf{v}_1. \tag{2.8}$$

So the number of particles scattered into $d\Omega$ between time t and $t + dt$ is

$$f(\mathbf{r}, \mathbf{v}_1, t)\left|\mathbf{v} - \mathbf{v}_1\right| d\mathbf{v}_1\sigma(\Omega)d\Omega dt. \tag{2.9}$$

So far we have assumed that a particle exists at the precise phase-space coordinate ($\mathbf{r}$,$\mathbf{v}$) at time t, which was imposed by Eq. (2.7). We cannot assume, however, that a particle exists at a precise phase-space coordinate and instead must consider the *probability* of finding a particle at ($\mathbf{r}$,$\mathbf{v}$) and thus we must include the single-particle distribution of our test particle. Incorporating the distribution of our test particle, which is multiplied by Eq. (2.9), the total number of scattering events can be determined by integrating over all scattering angles as well as all possible velocities of atoms in the incoming beam, $\mathbf{v}_1$. Because the velocity of both particles will change abruptly after a collision, the distribution will decrease abruptly at a given phase-space coordinate. The total decrease in $f(\mathbf{r}, \mathbf{v}, t)$ in some particular phase-space volume element is thus

$$\left(\frac{\partial f}{\partial t}\right)^{-}_{coll} d\mathbf{r}d\mathbf{v}dt = f(\mathbf{r},\mathbf{v},t)d\mathbf{r}d\mathbf{v}dt\int\sigma(\Omega)d\Omega\int d\mathbf{v}_1\left|\mathbf{v}-\mathbf{v}_1\right|f(\mathbf{r},\mathbf{v}_1,t). \tag{2.10}$$

Multiple collisions in this infinitesimal phase-space volume between t and $t+dt$ are neglected because of the assumption that the gas is sufficiently dilute. This assumes collision events where $\{\mathbf{v},\mathbf{v}_1\}\rightarrow\{\mathbf{v}',\mathbf{v}'_1\}$, however, particles can also scatter such that $\{\mathbf{v}',\mathbf{v}'_1\}\rightarrow\{\mathbf{v},\mathbf{v}_1\}$. These collisions will increase f, and contribute to the entering collision term in Eq. (2.5). The entering collision term can be derived with the same arguments and we find

$$\left(\frac{\partial f}{\partial t}\right)^{+}_{coll} d\mathbf{r}d\mathbf{v}dt = f(\mathbf{r},\mathbf{v}',t)d\mathbf{r}d\mathbf{v}'dt\int\sigma(\Omega)d\Omega\int d\mathbf{v}'_1\left|\mathbf{v}'-\mathbf{v}'_1\right|f(\mathbf{r},\mathbf{v}'_1,t). \tag{2.11}$$

Elastic collisions conserve both total and relative momentum so, since we are working with a monatomic gas, this implies

$$\left|\mathbf{v}-\mathbf{v}_1\right| = \left|\mathbf{v}'-\mathbf{v}'_1\right|. \tag{2.12}$$

At a given scattering angle $d\mathbf{v}d\mathbf{v}_1 = d\mathbf{v}'d\mathbf{v}'_1$ and the differential cross section is also identical for both entering and leaving collisions. Using these equalities we arrive at an entering collision term of the form

$$\left(\frac{\partial f}{\partial t}\right)^{+}_{coll} d\mathbf{r}d\mathbf{v}dt = f(\mathbf{r},\mathbf{v}',t)d\mathbf{r}d\mathbf{v}dt\int\sigma(\Omega)d\Omega\int d\mathbf{v}_1\left|\mathbf{v}-\mathbf{v}_1\right|f(\mathbf{r},\mathbf{v}'_1,t). \tag{2.13}$$

Although the distributions in the entering collision term depend on primed velocities, whereas the integral is carried out over a single unprimed velocity, it is implied that $\mathbf{v}$ is fixed while $\mathbf{v}'$ and $\mathbf{v}'_1$ are functions of $\mathbf{v}$, $\mathbf{v}_1$, and Ω.

Combining the entering and leaving collision terms brings us to the full form of the collision integral

$$I_{coll}[f] = \int d\mathbf{v_1}\int d\Omega\sigma\left(\Omega\right)\left|\mathbf{v}-\mathbf{v_1}\right|\left(f'f'_1 - ff_1\right), \tag{2.14}$$

using the shorthand notation for the distribution functions where $f\equiv f(\mathbf{r},\mathbf{v},t)$, $f'_1\equiv f(\mathbf{r},\mathbf{v}'_1,t)$, etc...

2.1 Collision Invariants

Once a gas reaches equilibrium, the distribution becomes static and

$$\frac{df}{dt} = 0. \tag{2.15}$$

Collisions are of course still occuring, but have no effect on the distribution as the collision integral must equal zero. There exists a class of solutions known as *collision invariants* for which the collision integral will always vanish. These solutions have the general form [13, 29, 27]

$$\log f = \alpha + \boldsymbol{\beta} \cdot \mathbf{p} + \gamma p^2, \tag{2.16}$$

where α, $\boldsymbol{\beta}$, and γ are arbitrary constants, but can also be functions of $\mathbf{r}$ and t. Solutions of this form will always force the collision integral to zero because of conservation of energy, momentum, and atom number. In other words, because

$$p^2 + p_1^2 = p'^2 + p_1'^2 \tag{2.17}$$

$$\mathbf{p} + \mathbf{p}_1 = \mathbf{p}' + \mathbf{p}_1', \tag{2.18}$$

then

$$f f_1 = f' f_1' \tag{2.19}$$

when the distributions are collision invariants. Thus, the kernel of the collision integral must always vanish for distributions of this form.

2.1.1 Equilibrium Distributions

While collision invariants force the collision integral to zero, they don't necessarily satisfy Eq. (2.3) and

$$\frac{df}{dt} \neq 0 \tag{2.20}$$

unless α, $\boldsymbol{\beta}$, and γ are properly constrained. Generically, distributions that cause the collision integral to vanish, but don't satisfy the Boltzmann equation, are referred to as "local equilibrium distributions." These local equilibrium distributions can be understood more intuitively by recasting Eq. (2.16) into a more familiar exponential form

$$f = \mathcal{A} e^{-\frac{\mathcal{B}m}{2}|\mathbf{v}-\mathbf{u}|^2}, \tag{2.21}$$

where $\mathcal{A}$, $\mathcal{B}$, and $\mathbf{u}$ can be functions of $\mathbf{r}$ and t. In order for the collision integral to vanish, energy conservation must now satisfy

$$|\mathbf{v}-\mathbf{u}|^2 + |\mathbf{v}_1 - \mathbf{u}|^2 = |\mathbf{v}' - \mathbf{u}|^2 + |\mathbf{v}_1' - \mathbf{u}|^2 . \tag{2.22}$$

Because $\mathbf{u}$ cannot depend on $\mathbf{v}$, this condition is met for local collisions and $\mathbf{u}$ is essentially a Galilean transformation.

The distribution (2.21) can be made to satisfy the Boltzmann equation for a general external potential $V(\mathbf{r})$ by setting

$$\mathcal{A} = \mathcal{A}_0 e^{-\mathcal{B}V(\mathbf{r})} \tag{2.23}$$

$$\mathcal{B} = \frac{1}{kT} \tag{2.24}$$

$$\mathbf{u} = 0, \tag{2.25}$$

where k is the Boltzmann constant, and T is the temperature. This is the well known Maxwell-Boltzmann distribution

$$f(\mathbf{r},\mathbf{v}) = \mathcal{A}_0 e^{-\frac{1}{kT}\left(\frac{1}{2}mv^2 + V(\mathbf{r})\right)}. \tag{2.26}$$

The contraints (2.23)-(2.25) provide the traditionally well-understood solution to the Boltzmann equation, however Boltzmann also explicitly derived various stationary non-equilibrium states that exist for certain special potentials [7, 28]. One example in particular is the undamped monopole mode in an isotropic harmonic potential.

2.2 Collective Excitations

2.2.1 Monopole Mode

2.2.1.1 Two Particle Derivation

The undamped nature of the monopole mode is found by calculating the evolution of the square radius of the cloud and can be derived in various ways [29]. It is instructive to see how the monopole nondamping result can be built up starting from small atom numbers $N = 1, 2,$ etc... Spherical symmetry simplifies the problem, which can be treated as analogously one dimensional. The radial motion of a single particle of mass m, energy E, and angular momentum L is governed by the effective potential [59]

$$V_e = \frac{L^2}{2mr^2} + \frac{1}{2}m\omega^2 r^2 \tag{2.27}$$

so that the radial force is

$$m\frac{d^2r}{dt^2} = -\frac{d}{dr}V_e \tag{2.28}$$

and the kinetic energy is

$$\frac{1}{2}m\left(\frac{dr}{dt}\right)^2 = E - V_e. \tag{2.29}$$

We note that $d^2r^2/dt^2 = 2(dr/dt)^2 + 2rd^2r/dt^2$, and substituting (2.28) and (2.29) yields the differential equation for r^2

$$\frac{d^2}{dt^2}r^2 = -\Omega^2\left(r^2 - r_0^2\right), \tag{2.30}$$

where $\Omega \equiv 2\omega$ and $r_0^2 = E/(m\omega^2)$. It can be seen by inspection of Eq. (2.30) that the square radius undergoes sinusoidal oscillations, or "monopole breathe", around its mean value r_0^2 at a frequency of 2ω. Now, if there are two particles, 1 and 2, each with individual values of E, L, and r^2, each particle will oscillate at 2ω and taking the sum of their respective differential equations (2.29) yields

$$\frac{d^2}{dt^2}r_t^2 = -\Omega^2\left(r_t^2 - r_{0t}^2\right) \tag{2.31}$$

where their combined square radius, $r_t^2 \equiv r_1^2 + r_2^2$, oscillates around its mean value, $r_{0t}^2 \equiv (E_1+E_2)/(m\omega^2)$. The magnitude of the collective breathe motion depends on the magnitude and relative phase of the individual particle trajectories. These individual quantities will abruptly change in the event of a collision. Assuming the collisions are local, r_1, r_2, and thus r_t^2 will not change from the instant before to the instant after the collision. Similarly, momentum and energy conservation imply that $\frac{d}{dt}r_t^2$ and r_{0t}^2 are unchanged by the collision.

These three continuities imply that the parameters and boundary conditions of Eq. (2.31) are matched directly before and after a collision. This ensures that neither the magnitude nor phase of the oscillation will change as the result of a pairwise collision. If we instead consider N atoms where

$$r_t^2 = \sum_{i=1}^{N} r_i^2 \tag{2.32}$$

$$r_{0t}^2 = \frac{1}{m\omega^2}\sum_{i=1}^{N} E_i, \tag{2.33}$$

one can see that the monopole mode is left unperturbed—and in particular *undamped*—by local, pairwise, momentum- and energy-conserving collisions.

The above approach is consistent with a system in the hydrodynamic limit, with total number of atoms so large that the function $f(\mathbf{r}, \mathbf{v}, t)$ is essentially continuous. However, in the hydrodynamic limit, mean-field effects can come into play in which case the monopole frequency is shifted and perhaps damped. In our experiment, the total number of atoms, N, is only a few hundred thousand, and the mean-free path is large compared to the spatial extent of the sample—we are not in the hydrodynamic limit in any sense of the word—and mean-field effects can be neglected.

2.2.1.2 Moments Method

Another way to calculate the behavior of the monopole mode is by calculating moments using the Boltzmann equation. In general, the expectation value of a quantity $\chi(\mathbf{r}, \mathbf{v})$ is

$$\langle \chi \rangle = \int \chi f d\mathbf{r} d\mathbf{v}. \tag{2.34}$$

The time evolution of χ can be determined using the Boltzmann equation

$$\int \chi \left(\frac{\partial}{\partial t} + \mathbf{v} \cdot \nabla_{\mathbf{r}} + \frac{\mathbf{F}}{m} \cdot \nabla_{\mathbf{v}} \right) f d\mathbf{r} d\mathbf{v} = \int \chi I_{coll}[f] d\mathbf{r} d\mathbf{v}. \tag{2.35}$$

By using the identity

$$\chi \frac{df}{dt} = \frac{d}{dt}(\chi f) - f \frac{d\chi}{dt} \tag{2.36}$$

we can rewrite Eq. (2.35) as

$$\begin{aligned} \int \Bigg[&\frac{\partial}{\partial t}(\chi f) + \mathbf{v} \cdot \nabla_{\mathbf{r}}(\chi f) + \frac{\mathbf{F}}{m} \cdot \nabla_{\mathbf{v}}(\chi f) \\ &-f \frac{\partial \chi}{\partial t} - f \mathbf{v} \cdot \nabla_{\mathbf{r}} \chi - f \frac{\mathbf{F}}{m} \cdot \nabla_{\mathbf{v}} \chi \Bigg] d\mathbf{r} d\mathbf{v} = \int \chi I_{coll}[f] d\mathbf{r} d\mathbf{v}. \end{aligned} \tag{2.37}$$

Because χ is not an explicit function of time, the fourth term in Eq. (2.37) drops out and we are left with

$$\frac{d\langle \chi \rangle}{dt} - \langle \mathbf{v} \cdot \nabla_{\mathbf{r}} \chi \rangle - \langle \frac{\mathbf{F}}{m} \cdot \nabla_{\mathbf{v}} \chi \rangle = \langle \chi I_{coll} \rangle. \tag{2.38}$$

A convenient property of the collision integral is that when χ is a collision invariant of the form $\chi(\mathbf{r}, \mathbf{v}) = a(\mathbf{r}) + \mathbf{b}(\mathbf{r}) \cdot \mathbf{v} + c(\mathbf{r}) v^2$, the expectation $\langle \chi I_{coll} \rangle$ is zero. This is a result of certain symmetries that let $\langle \chi I_{coll} \rangle = \langle \frac{1}{4}(\chi + \chi_1 - \chi' - \chi_1') I_{coll} \rangle$, which vanishes when conservation laws are imposed [33, 47].

The behavior of the monopole mode is found by calculating the time evolution of $\langle r^2 \rangle$. This quantity is a collision invariant, and using Eq. (2.38) we quickly arrive at the following closed set of equations:

$$\frac{d}{dt}\langle r^2\rangle = 2\langle \mathbf{r}\cdot\mathbf{v}\rangle \tag{2.39}$$

$$\frac{d}{dt}\langle \mathbf{r}\cdot\mathbf{v}\rangle = \langle v^2\rangle - \omega^2\langle r^2\rangle \tag{2.40}$$

$$\frac{d}{dt}\langle v^2\rangle = -2\omega^2\langle \mathbf{r}\cdot\mathbf{v}\rangle. \tag{2.41}$$

Differentiating Eq. (2.39) with respect to time then gives the wave equation

$$\frac{d^2}{dt^2}\langle r^2\rangle = -4\omega^2\langle r^2\rangle, \tag{2.42}$$

which describes undamped oscillations at frequency 2ω.

2.2.2 Dipole Mode

It turns out that there is one other undamped mode, the dipole mode, which is just a center-of-mass oscillation in the trap. The moment method can be used to also model dipole oscillations with the following set of equations

$$\frac{d}{dt}\langle \mathbf{r}\rangle = \langle \mathbf{v}\rangle \tag{2.43}$$

$$\frac{d}{dt}\langle \mathbf{v}\rangle = -\omega^2\langle \mathbf{r}\rangle. \tag{2.44}$$

These give the following wave equation

$$\frac{d^2}{dt^2}\langle \mathbf{r}\rangle = -\omega^2\langle \mathbf{r}\rangle, \tag{2.45}$$

which describes undamped oscillations of the center-of-mass position of the cloud at frequency ω. This result is perhaps less surprising than the undamped monopole mode and is equivalent to the solution for a single particle undergoing simple harmonic oscillations in a harmonic potential. The undamped behavior of the dipole mode is a result of the generalized Kohn theorem [17], which doesn't depend on the trap symmetry, and the result for an anisotropic trap returns a set of uncoupled wave equations along each principal axis of the potential. We use this mode to characterize our trapping potential as it provides a simple way of measuring trap frequencies.

2.2.3 Quadrupole Mode

Behavior of the axially symmetric quadrupole mode can be determined by calculating $\langle 2v_z^2 - v_r^2 \rangle$ using the moments method. The full treatment is discussed in [29], which arrives at the following result for monopole and quadrupole mode frequencies in an anisotropic harmonic trap with frequencies ω_r and ω_z:

$$\left(\omega^2 - 4\omega_z^2\right)\left(\omega^2 - 4\omega_r^2\right) - \frac{i}{\omega\tau}\left(\omega^4 - \frac{2}{3}\omega^2(5\omega_r^2 + 4\omega_z^2) + 8\omega_r^2\omega_z^2\right) = 0. \tag{2.46}$$

This equation is obtained using the "relaxation time approximation," where the relaxation time, τ, is defined as

$$\tau = \frac{5}{4\gamma_{coll}}. \tag{2.47}$$

The collision rate γ_{coll} is given by

$$\gamma_{coll} = \frac{n(0)v_{th}\sigma_0}{2} \tag{2.48}$$

for a peak density $n(0)$, average thermal velocity $v_{th} = \sqrt{8kT/\pi m}$, and scattering cross-section σ_0.

Solving for the roots of Eq. (2.46) gives complex monopole and quadrupole frequencies, where we define

$$\omega = \omega_0 + i\Gamma. \tag{2.49}$$

The real and imaginary parts correspond to the mode's natural oscillation frequency and damping rate respectively. For $\omega_r = \omega_z$, this method can be used to determine the complex monopole frequency, which is undamped with frequency $2\omega_{trap}$ as expected. However, the damping rate of the quadrupole mode in the collisionless limit depends linearly on collision rate and is approximately

$$\Gamma_Q \simeq \frac{1}{5}\gamma_{coll}. \tag{2.50}$$

In this limit, the quadrupole frequency is identical to the monopole frequency. When collisions are neglected entirely, the imaginary part of Eq. (2.46) is zero and the first term describes undamped monopole-like oscillations along each principal axis of the potential. As the hydrodynamic limit is approached, the monopole and quadrupole frequencies are split as shown in Fig. 2.1. While the monopole frequency is unchanged, the quadrupole frequency asymptotically approaches $\sqrt{2}\omega_{trap}$. In this limit, the quadrupole damping tends toward zero and it behaves like a true normal mode. Fig. 2.2 shows the damping in the crossover regime between the collisionless and hydrodynamic limits.

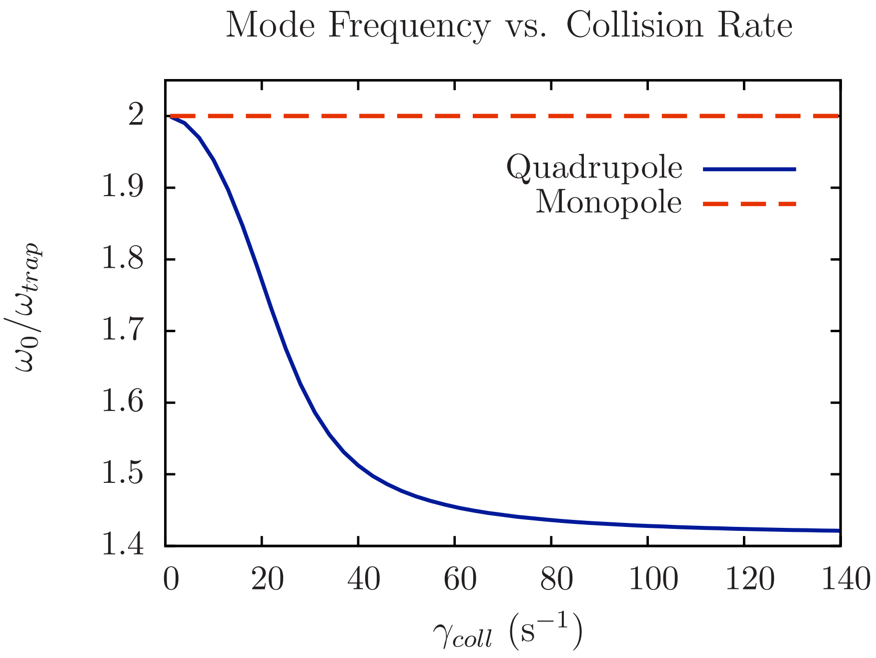

Figure 2.1: Frequency dependence on collision rate for monopole and quadrupole modes. As the $\gamma_{coll} \to \infty$ the frequency of the quadrupole mode approaches $\sqrt{2}\omega_{trap}$ while the monopole mode frequency is unchanged. These values are calculated from the real part of the roots of Eq. (**??**), where the roots correspond to the angular momentum projections $l_z = 2$ (quadrupole) and $l_z = 1$ (monopole) [29]. The trap frequency used in this calculation is $\omega_{trap} = 2\pi(9 \text{ Hz})$.

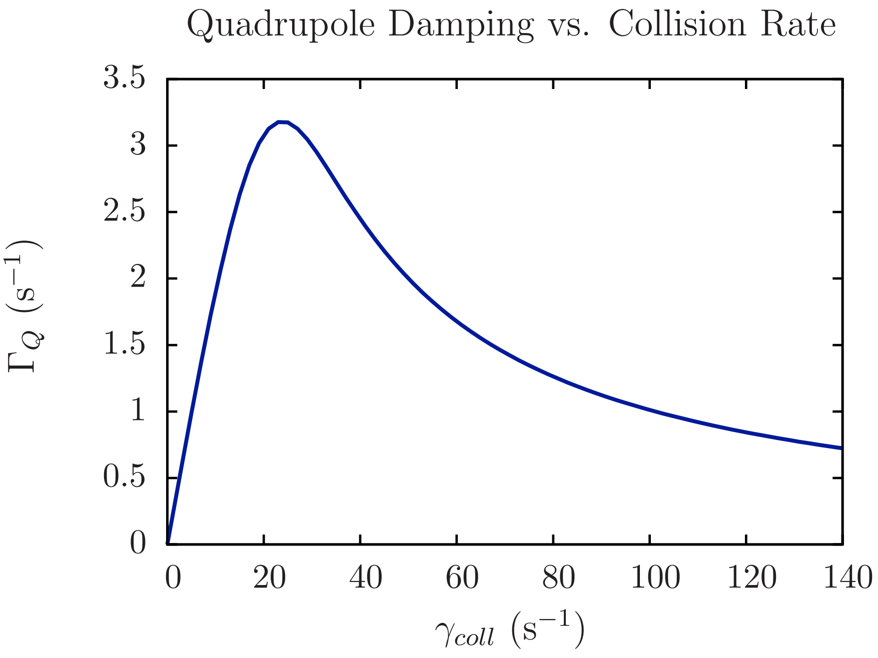

Figure 2.2: Damping of the quadrupole mode as a function of collision rate. In the collisionless limit, the quadrupole damping has a linear dependence on collision rate given by $\Gamma_Q \simeq \gamma_{coll}/5$. The actual slope is closer to 1/5.06328 for $\gamma_{coll} \leq 1$, which is calculated from Eq. (2.46). The trap frequency used in this calculation is $\omega_{trap} = 2\pi(9\text{ Hz})$.

2.2.4 Mode Coupling

Earlier it was mentioned that when neglecting collisions, the oscillations are essentially 1D monopole-like oscillations along each principal axis of the potential. It is important to note that when $\omega_r \neq \omega_z$, these oscillations dephase. When they are in phase, the overall behavior is that of a monopole breathe. When perfectly out of phase, it appears like a quadrupole oscillation. In the collisionless limit, this type of shape oscillation will still occur, but the modes are coupled by collisions [12]. This coupling causes the monopole mode to damp due to the non-zero energy populating the quadrupole mode. From Eq. (2.46), the dependence of damping rate on trap anisotropy can be calculated for both modes, and is shown in Fig. 2.3 for a collision rate of $\gamma_{coll} = 5.06$ (s^{-1}).

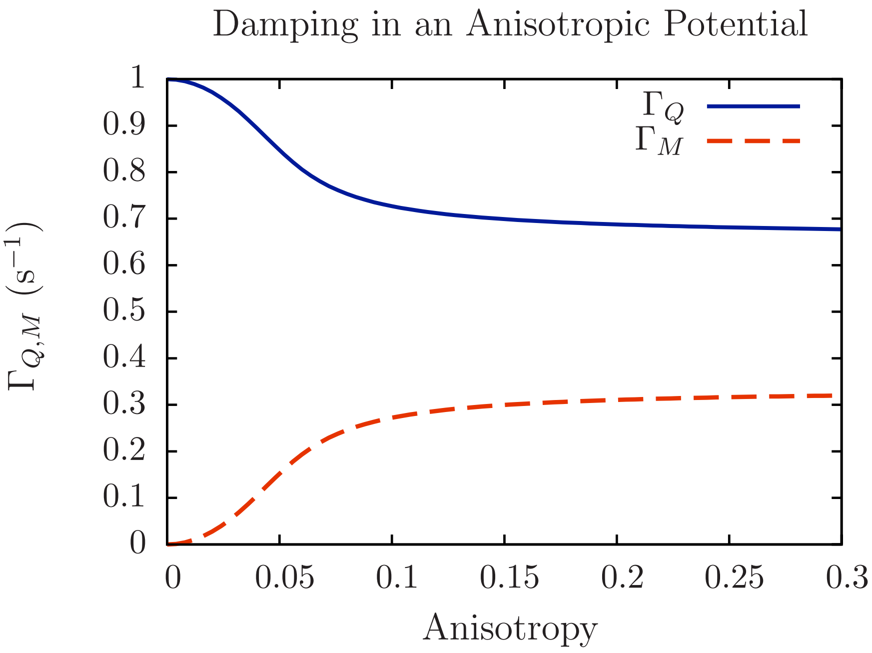

Figure 2.3: Shifts in the damping rates for the monopole and quadrupole modes due to mode coupling in an anisotropic trap as calculated from the real part of the $l_z = 2$ and $l_z = 1$ roots of Eq. (2.46). Anisotropy is defined by 2δ where $\omega_z = \omega_{trap}(1+\delta)$, $\omega_r = \omega_{trap}(1-\delta)$, and $\omega_{trap} = 2\pi(9\text{ Hz})$ is used as an approximate mean frequency. The collision rate is set to $\gamma_{coll} = 5.06\ (\text{s}^{-1})$, but the relative shift in damping rate for large anisotropies approaches the same values. The final values for the quadrupole and monopole mode damping rates sum to the quadrupole damping rate in an isotropic trap. For very anisotropic traps the monopole (quadrupole) modes approach a rate of approximately 1/3 (2/3) of the isotropic quadrupole damping result. Reducing γ_{coll} reduces the level of anisotropy at which the damping rates flatten out. This model appears to break down in the limit of large anisotropy, where both modes are populated for roughly equal times and one would expect that the damping rates should both converge to 1/2 the value of the quadrupole damping rate in a spherical trap.

2.3 Degenerate Clouds

When the cloud is Bose condensed, the behavior of the monopole mode is slightly modified. BECs are described by the Gross-Pitaevskii equation (GPE):

$$\left(-\frac{\hbar^2}{2m}\nabla^2 + V_{ext}(\mathbf{r},t) + g\left|\Psi_0(\mathbf{r},t)\right|^2\right)\Psi_0(\mathbf{r},t) = i\hbar\frac{\partial}{\partial t}\Psi_0(\mathbf{r},t). \tag{2.51}$$

Closely resembling the Schrödinger equation, the GPE contains an extra mean-field interaction term, $g\left|\Psi_0(\mathbf{r},t)\right|^2$, where $g = 4\pi\hbar^2 a_{scatt}/m$, a_{scatt} is the interatomic scattering length, and m is the atomic mass. Another difference is that $\Psi_0(\mathbf{r}, t)$ represents the collective wave function of the condensate, known as the *order parameter*, so the mean-field term can be instead represented by $gn(\mathbf{r}, t)$ where $n(\mathbf{r}, t)$ is the condensate density. Presence of the mean field modifies the potential, causing a shift in the frequency of the monopole mode equal to [26]

$$\omega_M = \omega_{trap}\sqrt{4 + \xi}, \tag{2.52}$$

for a 3D system with an average density, $\langle n \rangle$, and temperature, T, where

$$\xi = \frac{g\langle n \rangle}{g\langle n \rangle + kT}. \tag{2.53}$$

In the Thomas-Fermi limit, $\xi \simeq 1$ and $\omega_M = \sqrt{5}\omega_{trap}$.

For a pure condensate, the monopole mode is still undamped [46]. Damping, however, does occur for a finite temperature condensate. In this case, the normal and condensed components of the cloud oscillate at different frequencies because the normal component isn't as strongly affected by the mean field. Both components interact and, once their oscillations dephase, the collective monopole motion will relax. Various finite-temperature theories have been proposed [49] but, due to the lack of experimental tests of these models, their accuracy remains an open question.

Chapter 3

Generating a Spherical Harmonic Potential

3.1 Introduction

From a theoretical standpoint, the realization of an isotropic harmonic potential has enormous benefits as a testbed for numerous physical models. Not only can difficult calculations be greatly simplified by imposing spherical symmetry, which in many respects can be thought of as analogously one dimensional, but interesting physical phenomena also emerge in spherically symmetric systems [7, 13, 29, 53]. Experimental study of these systems has so far been prevented by the difficulty in generating spherical potentials.

Stable magnetic traps have long been paramount to ultracold atom experiments. Gases are typically cooled evaporatively and must be confined by a local minimum of an inhomogeneous magnetic field. Various magnetic traps have been developed for evaporative cooling experiments, such as the Ioffe-Pritchard trap [48], QUIC trap [21], and baseball trap [5] to name a few. However, almost none of the available traps is able to generate spherically symmetric confinement when gravitational forces are present. One exception is the time-averaged orbiting potential (TOP) trap [45], which uses a fast rotating bias field to create a local minimum in a quadrupole magnetic field. The TOP trap is capable of generating a suitably isotropic potential under ideal conditions. In practice, the water-cooled coils used to produce the magnetic fields are bulky and difficult to align. Any construction asymmetries give rise to a residual anisotropy in the potential, which is effectively impossible to prevent. The nature of the TOP trap allows for careful control of trap ellipticities confined to the plane of the rotating bias field. Previous experiments performed with a TOP trap were able to shim out asymmetries in the xy plane, allowing for cylindrical trap geometries that were round to within 0.1%. This chapter discusses a modification to the standard TOP trap, capable of shimming out elliptic cross terms in all three dimensions. A method of optimizing trap sphericity is demonstrated such that the three principal trap frequencies differ by less than 0.1%.

3.2 Basic TOP Theory

We begin our discussion with a brief overview of the TOP potential neglecting any gravitational effects. Tight confinement, a necessary feature of any magnetic trap used in evaporative cooling experiments, is produced by a quadrupole field defined by

$$\mathbf{B_Q} = \frac{B'_z}{2} x\hat{x} + \frac{B'_z}{2} y\hat{y} - B'_z z\hat{z}. \tag{3.1}$$

The quadrupole field alone is insufficent for ultracold atom experiments because the vanishing field at the center of the trap allows for Majorana transitions causing atoms to fall out of the trap faster than they can be evaporatively cooled [41]. Other magnetic traps take advantage of the quadrupole field because of its simplicity, but add extra fields to create a non-zero local minimum [48, 5, 21]. The TOP trap does this with the addition of a rotating bias field of the form

$$\mathbf{B_{TOP}}(t) = B_0 \cos(\omega t)\hat{x} + B_0 \sin(\omega t)\hat{y}. \tag{3.2}$$

The instantaneous field simply adds a linear offset to the quadrupole field, displacing the magnetic zero-point of the quadrupole field from the atoms. By setting the rotation frequency, ω, much faster than the characteristic trap frequency, the atoms are not only prevented from reaching the quadrupole zero, but micromotion induced by the oscillating field is negligible, thus creating a stable potential. The potential is calculated by taking the time average of the magnitude of the total magnetic field, so

$$\begin{aligned} U_0 = \mu\frac{\omega}{2\pi}\int_0^{\frac{2\pi}{\omega}} & dt[(B_0\cos(\omega t) + \frac{B'_z}{2}x)^2 \\ & +(B_0\sin(\omega t) + \frac{B'_z}{2}y)^2 + 4B'^2_z z^2]^{\frac{1}{2}} \end{aligned} \tag{3.3}$$

Expanding around the center of the trap, one finds

$$U_0 \simeq \mu B_0 + \frac{\mu B'^2_z}{16B_0}\left(x^2 + y^2 + 8z^2\right). \tag{3.4}$$

It can immediately be seen that the potential is harmonic with a minimum that is greater than zero. From Eq. (3.4), it is evident that the potential is anisotropic and the ratio of trap frequencies in the axial and radial dimensions is $\omega_z/\omega_r = \sqrt{8}$. This anisotropy is problematic when attempting to generate a spherical geometry. However, we take advantage of the fact that the potential is not perfectly harmonic to add a controlled distortion to the potential. Anharmonic effects can be seen directly by calculating U_0 at extremely large axial displacements. In the limit where $B'_z|z| >> B_0 >> B'_z\sqrt{x^2 + y^2}$, the integrand in Eq. (3.3) is dominated by the quadrupole field and the potential reduces to

$$U_0 \simeq 2\mu B'_z|z|, \tag{3.5}$$

which is not harmonic. For smaller displacements, the crossover between the harmonic and linear form of the potential amounts to a relaxation of the confinement that is most significant along $\hat{z}$.

By using gravity to our advantage, we are able to control the displacement along $\hat{z}$, and thus control the aspect ratio of the trap. To calculate this effect, an extra term is added to the Eq. (3.3) and the new potential is given by

$$U = U_0 + mgz. \tag{3.6}$$

The additional gravitational term adds a linear slope to the potenial, causing the minimum to move downward as shown in Fig. 3.1. Clearly, gravity always contributes to the full

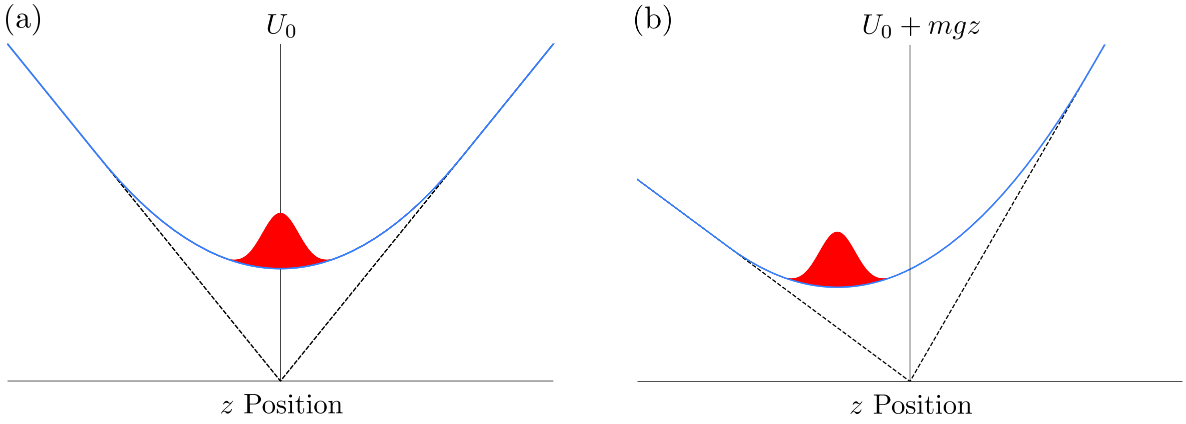

Figure 3.1: (a) Diagram of the TOP potential along the $\hat{z}$ axis, the atomic sample is shown in red and the anharmonic shifts are exaggerated to show how the potentially becomes asymptotically linear at large displacements from the center of the potential. (b) Representation of the effective tilting of the potential caused by gravity. The location of the trap minimum is shifted, and the cloud moves closer to the linear region of the potential leading to a relaxation in the confinement.

potential, but the displacement due to gravity, or gravitational sag, depends on the ratio of the gravitational force to the magnetic force on the atoms. We define the ratio of these two forces as

$$\eta \equiv \frac{mg}{\mu B'_z} \tag{3.7}$$

In the high-field limit $\mu B'_z >> mg$, the gravitational term can be dropped from Eq. (3.6) and U_0 is an adequate approximation of the potential. By decreasing B'_z, we can control how much the atoms sag in the trap and preferentially relax the confinement in the z dimension. However, the calculation of the potential must be expanded around the new minimum, which is given by

$$\mathbf{z_0} = -\frac{B_0}{B'_z}\frac{\eta}{\sqrt{1-\eta^2}}\hat{z}. \tag{3.8}$$

Carrying out the expansion around $\mathbf{z_0}$, we find

$$\begin{aligned} U \simeq \mu B_0\sqrt{1-\eta^2} &+ \frac{\mu B_z'^2}{16B_0}\left(1+\eta^2\right)\sqrt{1-\eta^2}\left(x^2+y^2\right) \\ &+ \frac{\mu B_z'^2}{2B_0}\left(1-\eta^2\right)^{3/2} z^2. \end{aligned} \tag{3.9}$$

The ratio of trap frequencies is now determined by η, where

$$\frac{\omega_z}{\omega_r} = \sqrt{8\frac{1-\eta^2}{1+\eta^2}}. \tag{3.10}$$

Because the only adjustable parameter in η is B_z', the quadrupole field strength must be tuned to set the aspect ratio of the trap, which is isotropic when $\eta = \sqrt{7/9}$.

Using gravity as a way of controlling the symmetry of the potential requires a weak trap with trapping frequencies on the order of 10 Hz. Another approach has been developed by Hodby et. al. known as the "zTOP" trap, which adjusts the symmetry of a TOP trap with an additional pair of Helmholtz coils oriented along the $\hat{z}$ axis [32]. Their method adds a linear offset to the trap so that the atoms lie in the symmetric region of the potential. The atoms will of course feel an additional force that pushes them back toward the minimum of the potential but, using the same time-averaging principle employed by the TOP trap, the vertical offset can be reversed before the atoms can start to approach the minimum. Theoretically, the ideal modulation of the vertical bias field has the functional form of the square wave, with twice the frequency of the rotating bias field, in order to maximize the time in which the atoms are at the symmetric region of the potential. In their experiment, Hodby et. al. modulated the vertical field with certain harmonic components of the square wave to reduce the aspect ratio of the trap down to a level of $\omega_z/\omega_r = 1.6$.

3.3 Controlling Ellipticity

An ideal TOP trap construction would produce an isotropic potential without any modifications. However, measurements of the trap frequencies in our system reveal residual ellipticities in all dimensions. These ellipticities are most likely due to construction asymmetries that come with the difficulty in aligning bulky, water-cooled coils. Previous experiments were able to shim out the ellipticity in the xy plane by adding a small counter rotating field to the normal TOP field. The eccentricity and elliptic cross terms could be controlled by adjusting the amplitude and relative phase of the counter rotating field. This idea is illustrated

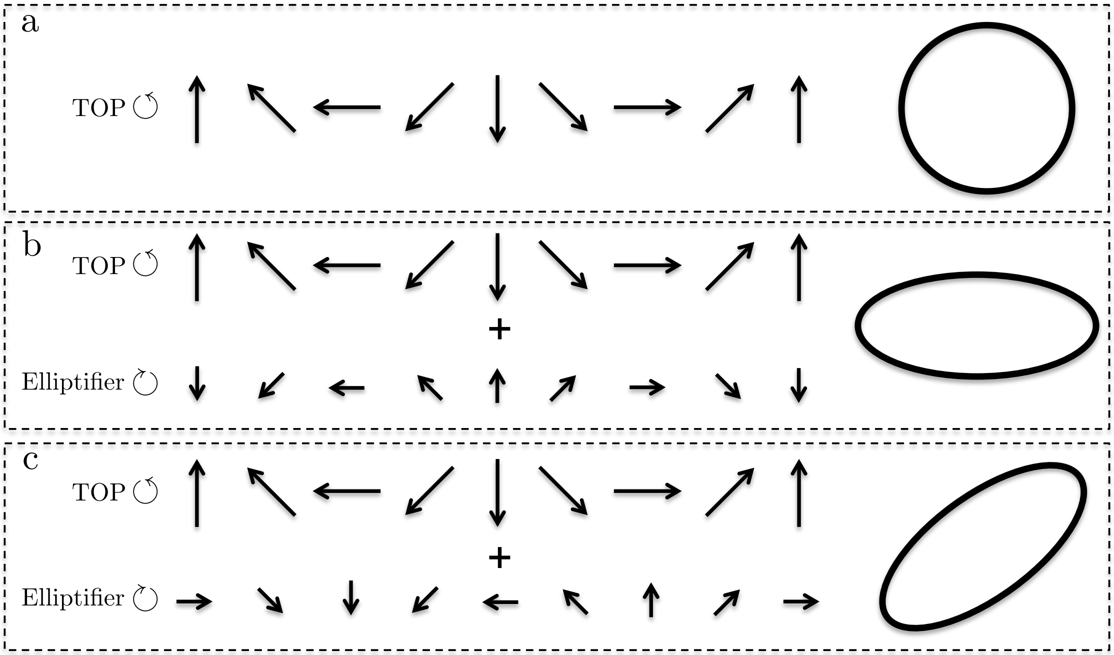

Figure 3.2: Each panel shows a representation of the rotating TOP field as well as an additional counter rotating field in the latter 2 panels. The path traced out by the quadrupole zero is represented on the right, and is characteristic of the ellipticity induced in the trapping potential in the xy plane.

in Fig. 3.2, where a small counter-rotating "elliptifier" field is added to a uniform TOP field to produce changes in the ellipticity of the contour produced by the path of the quadrupole field minimum. Fig. 3.2a shows the ideal TOP field, which in theory should be perfectly circular. Figs. 3.2b and 3.2c show how the elliptifier field can induce ellipticity where the principal axes of the ellipse rotate based on the phase of the elliptifier field. The Lissajous figure traced out by the quadrupole zero is directly proportional to the elliptical profile of the potential because $U = \mu\langle B(t)\rangle$. Of course, the goal is to produce a perfectly round profile, such as the one in Fig. 3.2a, however precise control of the ellipticity is required in order to shim out the residual ellipticities we observe in our trapping potential. The elliptifier field was previously used to create extremely cylindrical trap geometries—necessary for BEC vortex experiments—where the principal trap frequencies in the xy plane differed by 0.1% [30].

Unfortunately, this control was limited to only the plane of the TOP coils and elliptic cross terms in the xz and yz planes posed a significant problem for generating a spherical potential. Because one can control the ellipticities in the xy plane with the coils that lie in that plane, it stands to reason that one would gain control of the xz and yz planes if coils were aligned along those planes, which is possible with an additional set of TOP coils aligned with the $\hat{z}$ axis. One way to think of the oscillating $\hat{z}$ field is a field that causes the TOP field to tilt relative to the quadrupole field. Suppose the $\hat{z}$ field is oscillating with the same phase as the $\hat{x}$ field. When the field is maximized, the bias field will be tilted upwards towards the positive $\hat{z}$ direction. When the field is minimized, the bias field will be tilted downwards, and there will be no tilt when the field is zero. This is equivalent to mechanically tilting the TOP coils, which moves the Lissajous figure traced out by the quadrupole zero out of the xy plane. It should be noted that the purpose of this vertical field is entirely different than that of the zTOP trap, though the two ideas could presumably be combined.

It is important to work with parameters that are as orthogonal as possible to minimize the number of adjustments necessary for removing any ellipticities. An ellipsoidal potential contains 6 quadratic terms and has the form

$$U \propto Ax^2 + By^2 + Cz^2 + Dxy + Exz + Fyz, \tag{3.11}$$

where independent control of each coefficient lets us generate a spherical harmonic potential by setting $A = B = C$ and $D = E = F = 0$. These coefficients are directly controlled by the quadrupole and TOP fields. Because the quadrupole field must be set to control the symmetry between the radial and axial dimensions, it can only adjust the ratio $2C/(A+B)$ and the rotating bias fields must be used to control the remaining coefficients. The diagram in Fig. 3.2 demonstrates how the phase of the elliptifier field can be changed to rotate the ellipse, however this does not give independent control over the A, B, and D coefficents in the xy plane. We can instead define two separate fields corresponding to the counter-rotating fields in Figs. 3.2b and 3.2c. The first field, which we will continue to call the elliptifier field, will have a phase corresponding to the one shown in Fig. 3.2b. This field controls the A and B coefficients relative to some overall value set by the TOP field—in other words the elliptifier field could be described by δ, where $A \to A + \delta$ and $B \to A - \delta$—while not affecting the D coefficient. The D coefficient can be controlled by a counter-rotating field with a phase corresponding to Fig. 3.2c, and will not affect the A or B coefficients, giving independent control of the xy cross term. Cross terms in the xz and yz planes can be adjusted by including an oscillating field along the $\hat{z}$ axis, which has the same frequency and phase as the field in the $\hat{x}$ and $\hat{y}$ dimensions respectively. We now have 6 fields to control the 6 coefficients of the quadratic potential. The A, B, and C terms are controlled by the Quadrupole, TOP, and Elliptifier fields, while the D, E, and F terms are controlled by three additional "cross-term fields", all of which are summarized in Tab. 3.1.

	$\hat{x}$	$\hat{y}$	$\hat{z}$
Quadrupole	$\frac{B'_z}{2}x$	$\frac{B'_z}{2}y$	$-B'_z z$
TOP Field	$B_0 \cos(\omega t)$	$B_0 \sin(\omega t)$	0
$\hat{x}\hat{y}$ Elliptifier	$B_{ell} \cos(\omega t)$	-$B_{ell} \sin(\omega t)$	0
$\hat{x}\hat{y}$ Cross Term	$B_{xy} \sin(\omega t)$	$B_{xy} \cos(\omega t)$	0
$\hat{x}\hat{z}$ Cross Term	0	0	$B_{xz} \cos(\omega t)$
$\hat{y}\hat{z}$ Cross Term	0	0	$B_{yz} \sin(\omega t)$

Table 3.1: The six fields used to control the potential, separated into cartesian components.

The orthogonality of these fields can be shown explicitly by computing the new potential. With the additional fields, it difficult to solve for the potential analytically when gravity is taken into account. However, the analytic solution can be motivated by calculating the time-averaged magnetic field, which can be then tuned to cancel out the construction asymmetries to realize the ideal TOP model. The new instantaneous field now takes the form

$$\begin{aligned}B_{mod}(t) = [((B_0 + B_{ell})\cos(\omega t) + B_{xy}\sin(\omega t) + \frac{B'_z}{2}x)^2 \\ +((B_0 - B_{ell})\sin(\omega t) + B_{xy}\cos(\omega t) + \frac{B'_z}{2}y)^2 \\ +(B_{xz}\cos(\omega t) + B_{yz}\sin(\omega t) - B'_z z)^2]^{\frac{1}{2}}\end{aligned} \tag{3.12}$$

Expanding Eq. 3.12 around the trap center one finds

$$\begin{aligned}B_{mod}(t) \simeq B_0 + \frac{B'^2_z}{8B_0}(x^2 + y^2 + 4z^2) \\ -\frac{B'^2_z}{8B_0^3}[((B_0 + B_{ell})\cos\omega t + B_{xy}\sin\omega t)\,x \\ + ((B_0 - B_{ell})\sin\omega t + B_{xy}\cos\omega t)\,y \\ -2\,(B_{xz}\cos\omega t + B_{yz}\sin\omega t)\,z]^2\end{aligned} \tag{3.13}$$

Here we have assumed that the extra shimming fields are small compared to B_0 so, at the field origin,

$$\langle B_{mod}(t)\rangle|_{\mathbf{r}=0} = \frac{\omega}{2\pi}\int_0^{\frac{2\pi}{\omega}} |B_{mod}(t)|_{\mathbf{r}=0} = B_0. \tag{3.14}$$

This simplification is made so that any sinusoidal terms in the denominator of Eq. 3.14 fall out, as in the solution for the ideal TOP field. Evaluating the square in the final term in Eq. 3.14 and computing the time average, one finds

$$\begin{aligned}\langle B_{mod}(t)\rangle \simeq B_0 + \frac{B'^2_z}{8B_0}(x^2 + y^2 + 4z^2) \\ -\frac{B'^2_z}{16B_0^3}[\left((B_0 + B_{ell})^2 + B_{xy}^2\right)x^2 \\ + \left((B_0 - B_{ell})^2 + B_{xy}^2\right)y^2 \\ +4\left(B_{xz}^2 + B_{yz}^2\right)z^2 \\ +4B_{xy}B_0xy \\ -4\,(B_0B_{xz} + B_{ell}B_{xz} + B_{xy}B_{yz})\,xz \\ -4\,(B_{xy}B_{xz} + B_0B_{yz} - B_{ell}B_{yz})\,yz\;]\end{aligned} \tag{3.15}$$

Because the shimming fields are considered to be small, coefficients that are second order in any of the shimming fields can be dropped, leaving

$$\begin{aligned}\langle B_{mod}(t)\rangle \simeq B_0 \quad &+ \quad \frac{B_z'^2}{16B_0}(x^2+y^2+8z^2) \\ &+ \quad \frac{B_z'^2}{4B_0^2}\left[-\frac{1}{2}B_{ell}x^2+\frac{1}{2}B_{ell}y^2-B_{xy}xy+B_{xz}xz+B_{yz}yz\right].\end{aligned} \tag{3.16}$$

One can see that Eq. 3.16 is the same as Eq. 3.4 with extra terms that give full control over the ellipticity in the xy plane plus control over the elliptic cross terms in the xz and yz planes. Once the elliptic cross terms are shimmed out, the resulting potential matches that of the ideal TOP, and the frequency ratio ω_z/ω_r can be set by tuning the strength of the quadrupole field.

Gravitational effects slightly modify the terms in Eq. (3.16). To account for these differences, the full potential was computed numerically around $\mathbf{z_0}$ in a spherical trap and the strength of the elliptic shimming fields was found to differ by the following numerical factors,

$$\xi = \frac{1}{10}, \qquad \zeta = \frac{1}{6} \tag{3.17}$$

where Eq. 3.16 is instead written as

$$\begin{aligned}\langle B_{mod}(t)\rangle \simeq B_0 &+ \frac{\sqrt{2}B_z'^2}{27B_0}(x^2+y^2+z^2) \\ &+ \frac{4\sqrt{2}B_z'^2}{27B_0^2}\left[-\frac{\xi}{2}B_{ell}x^2+\frac{\xi}{2}B_{ell}y^2-\xi B_{xy}xy+\zeta B_{xz}xz+\zeta B_{yz}yz\right].\end{aligned} \tag{3.18}$$

This result agrees very well with the measured elliptical cross terms as shown in Fig. 3.3, which shows the dependence of the yz coefficient on the B_{yz} field.

3.4 Anharmonic Effects

Using a TOP trap to generate a near-spherical potential comes at the cost of introducing anharmonic perturbations. It is essentially the anharmonic effects that support the spherical solution. Anharmonic terms can be computed by expanding the TOP potential to

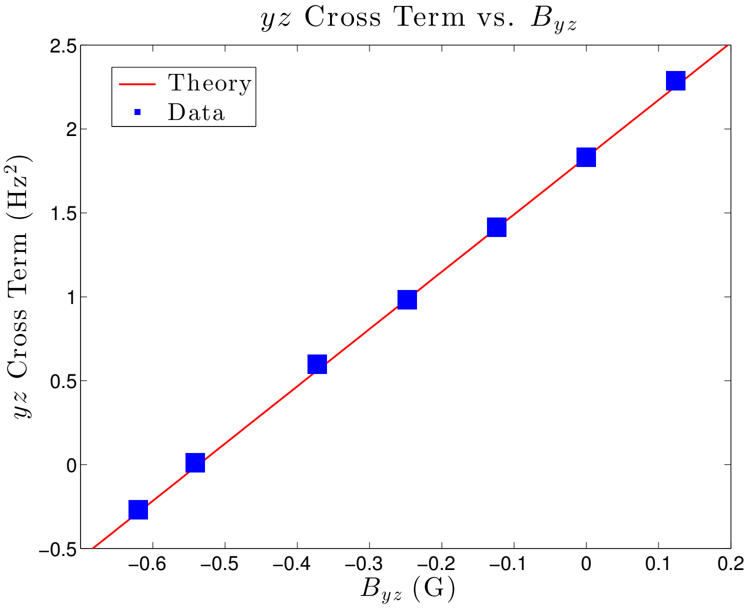

Figure 3.3: Measurement of the yz cross term for different strengths of the B_{yz} field. The slope of the theory line is determined from Eq. 3.18 but is offset by the measured yz cross term at $B_{yz} = 0$ to account for the residual ellipticity in the trap.

higher order, where we assume that any asymmetries have been shimmed out. The coefficients for the potential up to 4th order in r and z is are given in table 3.2.

	r^0	r^2	r^4
z^0	$B_0\sqrt{1-\eta^2}\mu$	$\frac{B_z'^2\sqrt{1-\eta^2}(\eta^2+1)\mu}{16B_0}$	$\frac{B_z'^4\sqrt{1-\eta^2}(15\eta^6-21\eta^4+5\eta^2+1)\mu}{1024B_0^3}$
z^1	0	$-\frac{B_z'^3\eta(3\eta^4-4\eta^2+1)\mu}{16B_0^2}$	$-\frac{3B_z'^5\eta(\eta^2-1)^2(35\eta^4-30\eta^2+3)\mu}{1024B_0^4}$
z^2	$\frac{B_z'^2(1-\eta^2)^{3/2}\mu}{2B_0}$	$\frac{B_z'^4(1-\eta^2)^{3/2}(15\eta^4-12\eta^2+1)\mu}{32B_0^3}$	$-\frac{3B_z'^6(1-\eta^2)^{5/2}(35\eta^2(9\eta^4-11\eta^2+3)-3)\mu}{2048B_0^5}$
z^3	$\frac{B_z'^3\eta(\eta^2-1)^2\mu}{2B_0^2}$	$\frac{B_z'^5\eta(\eta^2-1)^2(35\eta^4-40\eta^2+9)\mu}{32B_0^4}$	$\frac{5B_z'^7\eta(\eta^2-1)^3(7\eta^2(99\eta^4-153\eta^2+65)-45)\mu}{2048B_0^6}$
z^4	$\frac{B_z'^4(1-\eta^2)^{5/2}(5\eta^2-1)\mu}{8B_0^3}$	$\frac{B_z'^6(1-\eta^2)^{5/2}(5\eta^2(63\eta^4-91\eta^2+33)-9)\mu}{128B_0^5}$	$-\frac{15B_z'^8(1-\eta^2)^{7/2}(7(429\eta^6-792\eta^4+450\eta^2-80)\eta^2+15)\mu}{8192B_0^7}$

Table 3.2: Full list of coefficients for the TOP potential, arranged by the orders of r and z which they multiply.

	r^0	r^2	r^4
z^0	$8.157 \times 10^{-2} R_0$	$3.625 \times 10^{-2} R_0^{-1}$	$-9.651 \times 10^{-4} R_0^{-3}$
z^1	0	$2.261 \times 10^{-2} R_0^{-2}$	$-5.931 \times 10^{-4} R_0^{-4}$
z^2	$3.625 \times 10^{-2} R_0^{-1}$	$6.714 \times 10^{-3} R_0^{-3}$	$2.275 \times 10^{-3} R_0^{-5}$
z^3	$3.014 \times 10^{-2} R_0^{-2}$	$-7.071 \times 10^{-3} R_0^{-4}$	$6.771 \times 10^{-3} R_0^{-6}$
z^4	$2.327 \times 10^{-2} R_0^{-3}$	$-1.552 \times 10^{-2} R_0^{-5}$	$1.03 \times 10^{-2} R_0^{-7}$

Table 3.3: List of full TOP expansion coefficients for a spherical trap. R_0 is the radius of the trajectory of the quadrupole zero, known as the "circle of death."

Symmetry in the radial plane causes all of the odd powers of r to vanish, but this symmetry does not exist in the z dimension, giving rise to odd powers of z. Imposing spherical symmetry constrains the value of B'_z and η, and we get a simplified set of coefficients shown in table 3.3. The magnetic moment, μ, has been removed and we have introduced $R_0 \equiv 2B_0/B'_z$, which is the radius of the quadrupole field zero from the center of the trap, often called the "circle of death." Each coefficient is of roughly the same order, with the exception of R_0. So the anharmonic terms could be reduced by either decreasing the cloud size, or by increasing the radius of the circular trajectory, R_0. However, increasing R_0 reduces the trap frequency and requires longer evolution times for studies of collective oscillations and presents greater difficulty when trying to drive individual modes.

Chapter 4

Experimental Details

The experiment itself has a long and colorful history, and many of its current components were used for the realization of the first Bose-Einstein condensate (BEC) in 1995 [2]. Shortly after the 1995 experiment, the group made several modifications to the apparatus, dubbed “JILA Mark III”, including an entirely new chamber that has been continuously under vacuum since late 1996 [20]. A perfect way to describe the current state of the experiment is from a former graduate student on this experiment, Paul Haljan, who wrote in his 2003 thesis [31]:

> Although practically every part of the setup has undergone modification, the same basic apparatus underlies it all (if you can still see it under the optics and coils!) Only now is the experiment beginning to suffer from some limitations, particularly in optical access, leaving room for plenty of ingenuity.

When this was written, JILA Mark III had only been in use for 7 years, however the vacuum system is now older than the incoming freshman class and other components (including the control computer) are older than the incoming first year graduate students! It is safe to say that ingenuity has played a key role in the development of experiments conducted with JILA Mark III over the last decade. It is also safe to say that each time the experiment changed hands, it became slightly more complicated and modifications from one generation of students were often incorporated into modifications from later generations. Despite the various layers of obfuscation involved in the experimental process, it can still consistently produce big, beautiful condensates. While the experiment has endured a spectacular evolution over the years, Paul Haljan's statement still holds true: the same basic apparatus underlies it all.

4.1 Apparatus

The experiment's longevity is primarily attributable to the simplicity of the vacuum system, which lies at the core of the experiment. With the exception of the Rb getters, the vacuum chamber does not contain any feedthroughs or components that pertain directly to the experimental sequence. Nearly any modification to the experiment can be made externally, removing the need to break vacuum. Traditionally, the apparatus has been used for BEC experiments and low background pressures are imperative to ensure long BEC lifetimes. When the system was first constructed, the group was able to reach background pressures as low as 10^{-12} Torr. Since then, the system has been under continuous vacuum and determining the actual pressure is difficult; BEC lifetimes are several minutes long.

The dominant source of background pressure comes from our Rb dispensers, which are evaporative getters. Atoms are first collected in a magneto-optical trap (MOT) [43], where the filling rate of the MOT depends largely on the background Rb pressure. During the first experiments with BECs in this lab, low enough background pressures required extremely long MOT load times and one experimental cycle took nearly 20 minutes. The JILA mark III uses a double-MOT system [43] to allow for fast filling times and maintain a low background pressure in the evaporation region. The apparatus, shown in Fig. 4.1, is fitted with two MOT cells connected by a 37 cm long, stainless steel "transfer" tube.

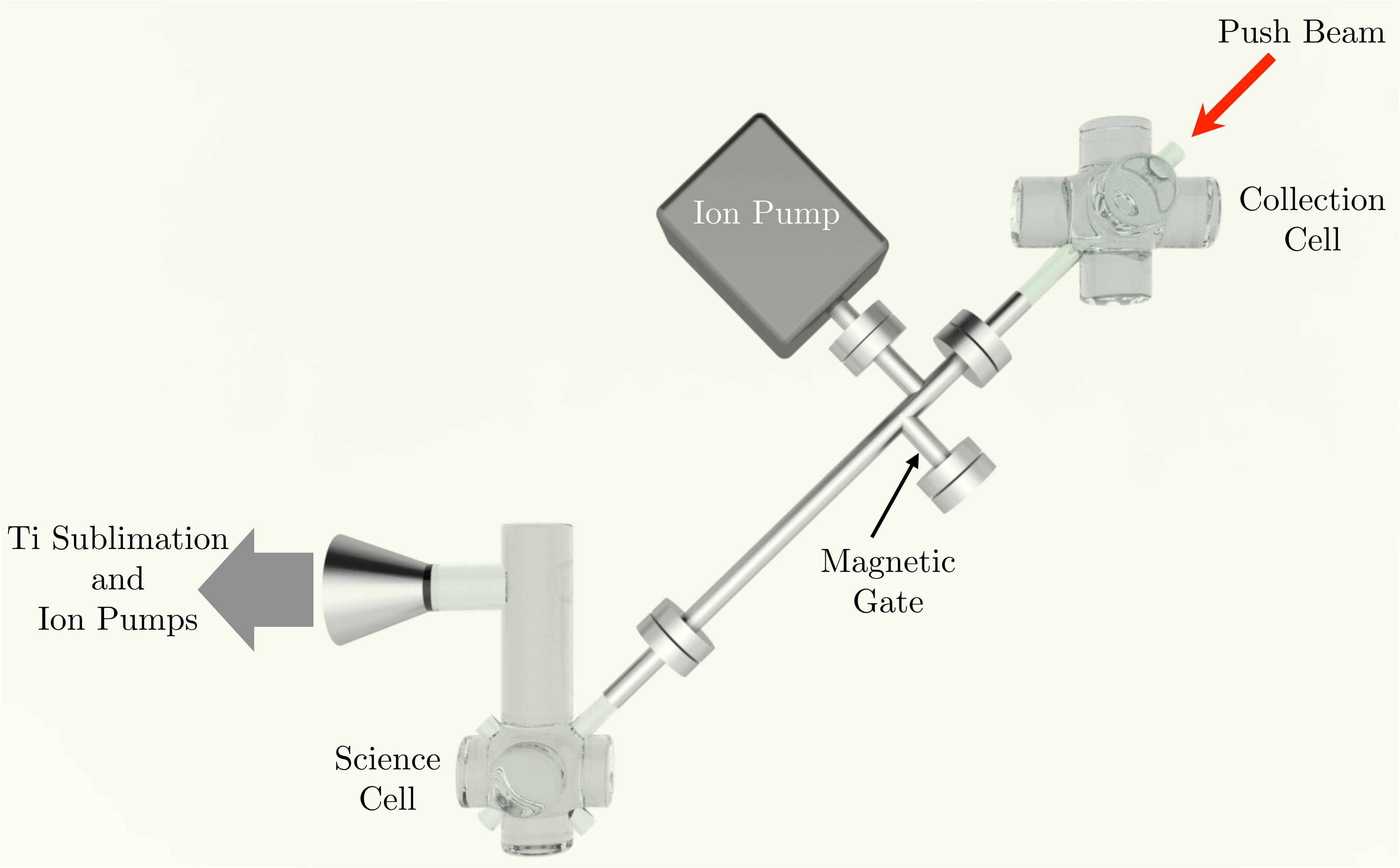

Figure 4.1: Layout of the vacuum chamber. The transfer tube is 37 cm long with a diameter of 1.3 cm and has a spiral-wound wire resting against its interior to prevent scattered light from the collection MOT beams from reaching the science MOT. Two additional connections are made to the transfer tube, one is attached to a 20 L/s ion pump, while the other houses a magnet encased in glass used to block the tube so as to limit vacuum conductance when the experiment is not in use. A portion of the vacuum system is not shown, which connects to a 30 L/s ion pump, a titanium sublimation pump, and a roughing valve that was used for initially pumping out the chamber. Artistic rendering courtesy of David Lobser.

Initially atoms are loaded in the “collection” MOT cell, which contains the Rb getters and runs a higher background pressure of around 10^{-9} Torr to speed up loading, then they are transferred to the “science” MOT using a push beam. The collection MOT has two sets of getters, each set up in a parallel as shown in Fig. 4.2

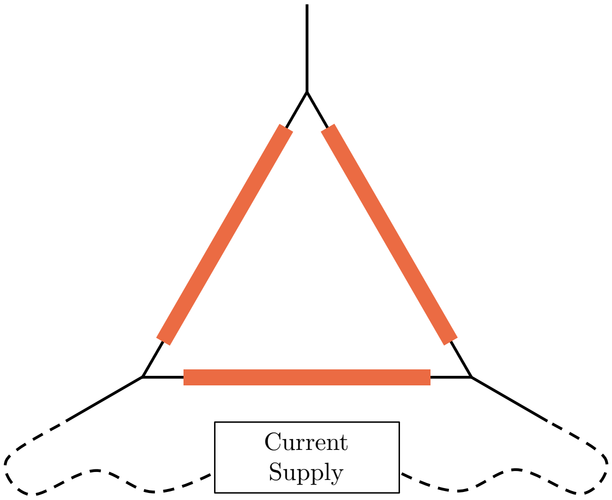

Figure 4.2: Configuration of the Rb getters. The collection MOT cell contains two arms each with 3 getters arranged in this configuration. The current supply is attached to two of the three available terminals so that the current through the getter directly between the two active terminals is twice the current through the other two. This keeps the getters warm and prevents any contaminants or extra Rb from sticking to them.

At the end of each day, we turn off the getter current to maximize their lifetime, which was originally predicted to be two years per getter [20]. However, we only switched to the second getter arm two years ago, and the actual lifetime is closer to 6 years per getter. We also minimize residual background Rb from collecting in the science cell by blocking the transfer tube with a magnetic gate. In Fig. 4.1, a small arm attached to the transfer tube contains a bar magnet encased in glass. The gate is opened or closed using another bar magnet, which is dragged along the outside of the tube.

Under normal operating conditions, the collection MOT load time is roughly one second. The push beam is pulsed every 400 ms until the number of atoms in the science MOT (proportional to the MOT fluorescence monitored on a photodiode) is 80% of the desired value, at which point the pulse separation reduces to 200 ms. To increase the stability of the initial number, and to reduce any initial slosh, we load 5% more atoms than specified and wait for the science MOT to decay to the correct value before loading the atoms into the magnetic trap. Several stages are involved when loading atoms into the magnetic trap. After enough atoms are collected in the MOT, the quadrupole field is ramped down from 17.4 G/cm to 5.2 G/cm for a compressed MOT (CMOT) stage. Then the quadrupole field is removed entirely, at which point the atoms are cooled to sub-doppler temperatures in an optical molasses and then optically pumped on the $|F = 2, m = 2\rangle \rightarrow |F = 1, m = -1\rangle$ transition. At this point, the quadrupole and TOP fields are quickly ramped on and the evaporative cooling procedure is initiated.

Forced evaporation of the atomic sample in a TOP trap is slightly different from most BEC experiments. Radiofrequency (RF) radiation is coupled to the atoms, pumping the outermost (and thus most energetic) atoms into an untrapped state. During the first stages of evaporation, the RF frequency is ramped down from 100 MHz to 13 MHz, but a key difference of evaporating in a TOP trap is that the TOP bias field is simultaneously reduced from 50 G to 5.2 G. Initially, the TOP field must be large so that the radius of the circle of death is larger than the size of the cloud. However, the trap frequency scales inversely with the TOP field. Evaporating in a weakly confining potential can be problematic because elastic collision rate, which is directly proportional to rethermalization rate, scales as the square of the trap frequency. Efficiency of the evaporative sequence is thus maximized by maintaining the largest allowable trap frequency at all times.[1] The maximal trap frequency is limited by the cloud size and, during the first stages of evaporation, the TOP field is ramped down with the RF frequency so that the radius of the circle of death is slightly larger than the distance of the RF knife from the center of the trap. For the last stage of evaporation, the TOP trap settings are changed to another set of parameters that specify the

---

[1] During the early stages of evaporation this is not an issue, but when the density approaches 10^{14} cm^{-3} inelastic losses start to become problematic.

desired final trap geometry. It is during this stage that all of the shimming fields, including the vertical TOP fields are turned on. The remainder of the evaporation ramps only the frequency, and the TOP field is fixed.

4.1.1 TOP Fields

The primary TOP coils are set up in a Helmholtz configuration and aligned with the four horizontal windows of the science cell used for MOT beam access. In order to provide the 50 G field, the coils must be able to dissipate 180 W and are made from 22 AWG wire housed in a polyflo tubing for water cooling. The quadrupole coils are placed directly above and below the cell in an anti-Helmholtz configuration, and are made of water-cooled hollow copper tubing in order to dissipate a maximum of 2700 W. Because the vertical TOP coils only need to produce fields on the order of a few hundred mG, they don't require any water cooling. The TOP and quadrupole coils were both set up as close to the cell as possible, and the vertical TOP coils are placed directly above and below the quadrupole coils as shown in Fig. 4.3.

The TOP coils are driven by a 4.5 kHz sine wave that is split into two channels for the x and y coil pairs. Each channel is passed through a circuit where both the phase and amplitude of the signals are independently adjusted. A separate function generator is used to provide the elliptifier field signal, and passed through an identical circuit used for the TOP signal. The elliptifier signal is 45° out of phase with the TOP signal, which is used as a trigger, and the amplitude is adjusted by the control computer via GPIB. The elliptifier and TOP signals added together, then the outputs for the x and y coil pairs are sent to a dual-channel high-powered amplifier and impedance matched to the TOP coils using a pair of home-made transformers.

The 4.5 kHz sine wave used for the TOP fields is also passed to a separate circuit that drives the vertical TOP coils. This circuit has the same basic functionality as the one used for the TOP fields: the channels are split into sine and cosine components that are

Figure 4.3: Artistic representation of the science cell and field coils. The larger coils above and beneath the cell generate the quadrupole field, and the remaining coils are used for the TOP fields. The original TOP coils are mounted in on the horizontal windows and are actually slightly oblong. Artistic rendering courtesy of David Lobser.

independently adjusted. Because the current required for the vertical field is less than 1 A, the output is amplified by an LM675 power op-amp contained within the same circuit.

4.2 Imaging

The experiment is equipped with two independent imaging systems, which are set up to probe along two orthogonal axes. The older of the two imaging setups has a dedicated imaging port that is perpendicular to the axis of the transfer tube, while the other imaging system is aligned vertically. To speed up the data taking process, and to reduce errors associated with initial conditions such as atom number, we image the cloud non-destructively using the phase-contrast technique [3]. Phase-contrast imaging probes with light far-detuned from resonance. In this case, the light passing through the cloud experiences a small phase shift that depends on both the detuning of the probe beam and the density of the cloud. The resulting phase-shifted light is then interfered with the light that doesn't pass through the atoms, to resolve a signal. Phase shifts are typically only a few degrees, and the contrast of the interference is very small, and thus difficult to resolve. The contrast can be improved by selectively shifting the portion of the probe beam that is not incident on the cloud. Fig. 4.4 shows the layout of a phase-contrast imaging system. Light that passes through the sample is diffracted while the rest of the probe beam remains collimated. In Fourier space, the ratio of the widths of the collimated probe beam and the scattered light is inverted. Placing a "phase dot," which adds a $\pi/2$ phase shift to the light, at the focus of a lens allows the unscattered probe light to be phase shifted while leaving the scattered light nearly unaffected.

We use a confocal imaging setup, shown in Fig. 4.4, with the phase dot placed at the focus of the probe beam. The phase dot is made by depositing MgFl_2 onto a glass substrate. Its thickness is determined by the wavelength of the probe light and given by $\lambda/4(n-1) =$ 513 nm, where $n \approx 1.38$ is the refractive index of MgFl_2 [31]. For the side-view imaging system, the phase dot has a 100 μm diameter and is large enough to capture the probe beam, which has a 100 μm waist, but smaller than the scattered light, which has a typical

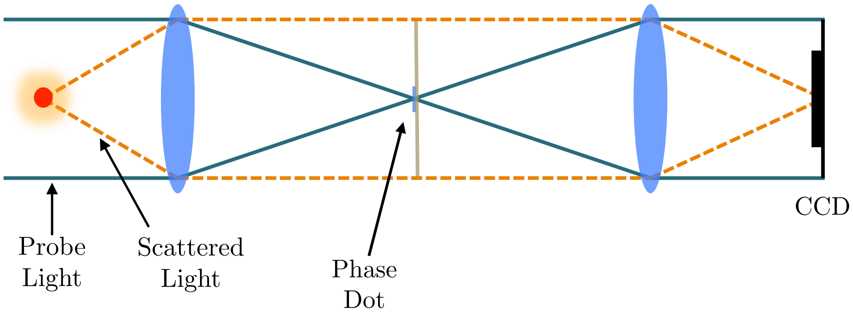

Figure 4.4: Layout of the phase-contrast imaging setup. The example shown has a magnification of unity, but can be enlarged by increasing the focal length of the second lens. It is necessary that the phase dot is larger than the waist of the probe beam, while remaining smaller than the scattered light. In the limit where the diameter of the phase dot is large enough that all the scattered light passes through it, the signal is reduced and equivalent to having no phase dot at all.

diameter of roughly 850 μm. The top-view imaging system uses a 200 μm phase dot to account for slight instabilities in the probe alignment. Because the top-view probe shares an axis with the MOT beams, two mechanical flipper mirrors are used in the beam path and small variations in their position cause the beam to shift slightly from shot to shot.

4.2.1 Expected Phase Shift

The phase shift imparted by the cloud as a function of detuning is

$$\phi = \frac{\omega d}{c} Re\left[n(\Delta)\right] \tag{4.1}$$

where d is the length of the condensate along the imaging axis and

$$Re\left[n(\Delta)\right] = 1 + \frac{Ne^2}{8\pi\epsilon_0 m\omega} \sum_i \frac{\Delta_i}{\Delta_i^2 + \left(\frac{\Gamma}{2}\right)^2} K_i \tag{4.2}$$

is the real part of the refractive index. N is the number of atoms, so that Nd is a column density, ω is the frequency of the light, and Δ_i is the detuning of the probe light from a particular quantum state (indexed with i). The sum is taken over all hyperfine states and the K_i terms are normalized Clebsch-Gordon coefficients so that $\sum_i K_i = 1$. Because the atoms only populate the $|F=1, m_F=-1\rangle$ hyperfine state, the detuning is taken to be constant and the sum is taken only over the relevant K_i's. We are interested in the phase difference between the refracted and non-refracted component of the probe beam which is

$$\Delta\phi \simeq \frac{\omega d}{c}\frac{Ne^2}{8\pi\epsilon_0 m\omega}\frac{\Delta}{\Delta^2+\left(\frac{\Gamma}{2}\right)^2}\frac{1}{2} \tag{4.3}$$

$$\simeq \frac{Nde^2}{8\pi\epsilon_0 mc}\frac{1}{2\Delta} \qquad \text{for } \Delta \gg \Gamma \tag{4.4}$$

Since the atoms are in the $|1,-1\rangle$ state, we typically do phase contrast imaging on the $F{=}1{\rightarrow}2'$ transition. In this case the absorption cross section is

$$\sigma_0 = \frac{\hbar\omega\Gamma}{2I_{sat}}. \tag{4.5}$$

In this case, the phase shift becomes

$$\Delta\phi = 2.85\frac{I_{sat}c^2}{\hbar\omega^3}\frac{N\sigma_0 d}{4\Delta} \tag{4.6}$$

Limitations in phase-contrast imaging are typically due to scattering when the probe is not sufficiently detuned from resonance. However, phase-contrast imaging is feasible because the signal goes as $S \propto \Delta^{-1}$ whereas the photon scattering rate goes as $R \propto \Delta^{-2}$. The scattering rate is well known and given by

$$R_{sc} = \frac{\Gamma}{2}\frac{I/I_{sat}}{1+4\left(\frac{\Delta}{\Gamma}\right)^2+\frac{I}{I_{sat}}} \tag{4.7}$$

$$\simeq \frac{\Gamma^3}{8\Delta^2}\frac{I}{I_{sat}} \qquad \text{for } \Delta \gg \Gamma \tag{4.8}$$

4.2.2 Expected Signal

The actual signal depends on the parameters of the phase dot, the thickness of which sets the sensitivity for the measured phase shift. The exact parameters of the phase dot are discussed in Paul Haljan's thesis [31] where the following relations for the signal and phase shift are presented

$$S_0(\Delta\phi) = 4\sin\frac{\delta_0}{2}\left[\sin\frac{\delta_0}{2} + \sin\left(\Delta\phi - \frac{\delta_0}{2}\right)\right] \tag{4.9}$$

$$\Delta\phi = \arcsin\left[\frac{S_0}{4\sin\frac{\delta_0}{2}} - \sin\frac{\delta_0}{2}\right] + \frac{\delta_0}{2}. \tag{4.10}$$

Here, S_0 is the measured signal, ϕ is the phase shift due to the atoms and $\delta_0 = \pi/2$ is the phase shift due to the phase dot.

The side-view probe frequency is servoed using a dichroic atomic vapor laser lock (DAVLL) [16]. Because the DAVLL lock is able to resolve only fine-structure spectra, the frequency is calibrated by interfering the probe with another laser locked to the resonant hyperfine transition used for absorption imaging. The interference is detected by a fast photodiode, and the set point on the DAVLL lock is adjusted so that the beat frequency between the two lasers is minimized. A small fraction of the probe light is diverted into a Fabry-Perot interferometer, which is used to measure the relative shift in frequency at different set points for the frequency lock and set the desired detuning from resonance. We normally run at a detuning of about 800 MHz to 1 GHz. Figs. 4.5 and 4.6 show plots of the expected phase shift for a typical cloud and scattering rate for detunings between 100 MHz and 1.1 GHz.

When the phase shift is large enough, the signal is no longer linear and will oscillate as the detuning approaches zero. The signal as a function of detuning is shown in Fig. 4.7. and a comparison with experiment is shown in Fig. 4.8 For this data, the cloud size is slightly smaller than the one used in earlier calculations and the on resonance OD was used as a fitting parameter.

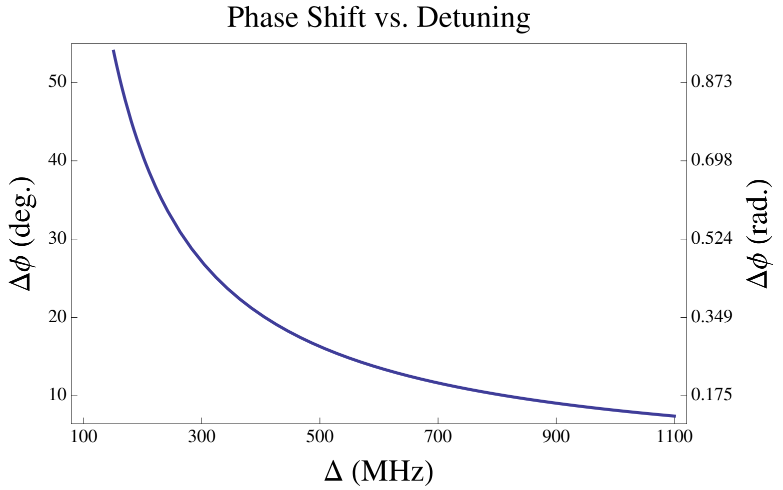

Figure 4.5: Expected phase shift of the probe as a function of detuning.

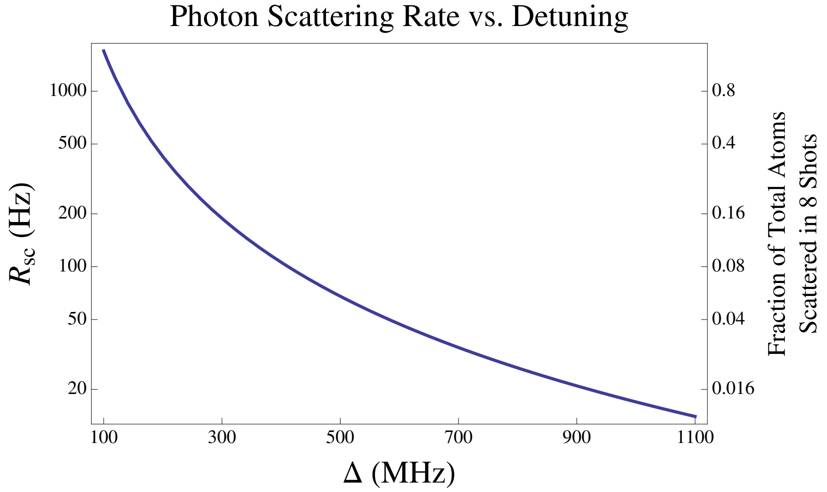

Figure 4.6: Expected scattering rate as a function of detuning.

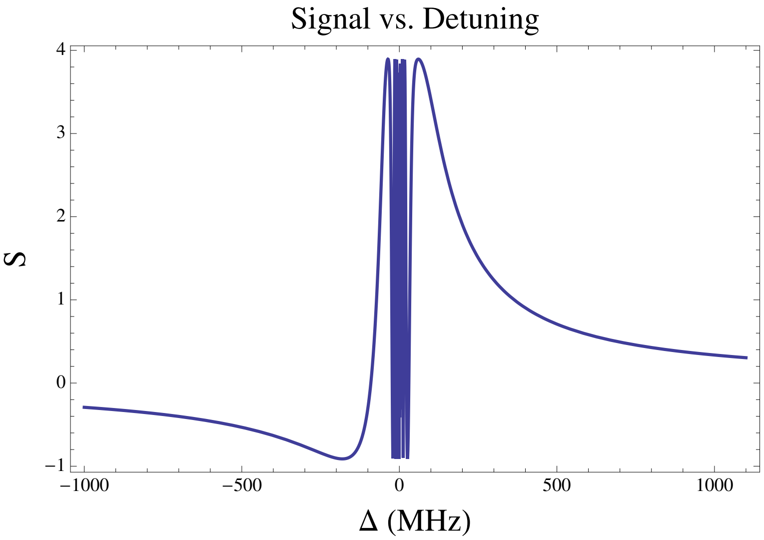

Figure 4.7: Signal vs. probe detuning, as calculated from Eq. 4.9

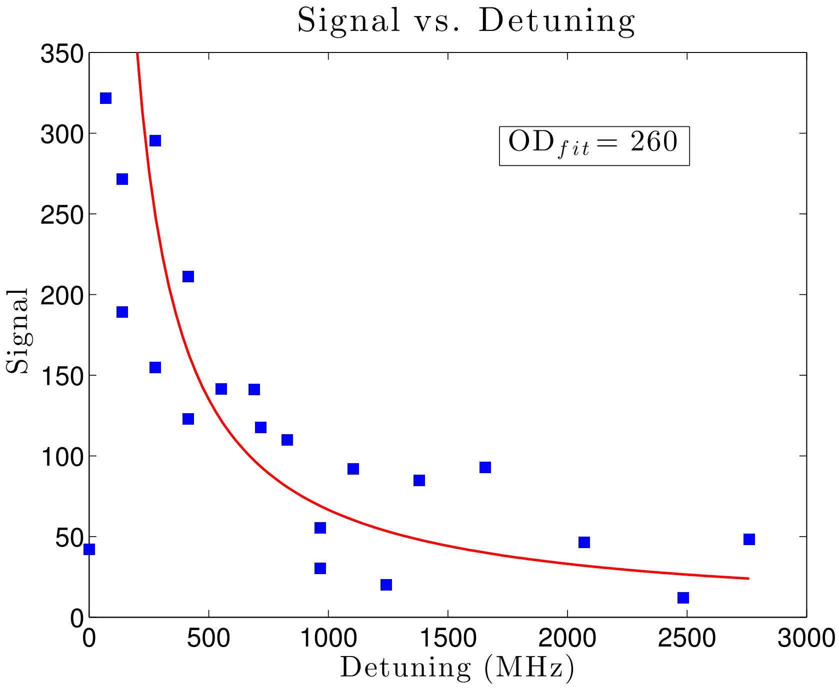

Figure 4.8: Comparison of expected signal to data where the signal has been scaled by a factor of 1000.

4.3 Trap Characterization

Trap frequencies are determined by driving center-of-mass (COM) "slosh" oscillations. The slosh mode is driven by temporarily displacing the center of the trap and measuring the COM position of our cloud at various times after the initial displacement. We use two imaging beams aligned along orthogonal axes so that the position of the cloud can be measured in all three dimensions simultaneously. Our machine is traditionally used for studies with Bose-Einstein condensates, which have a couple advantages. The small condensate size makes for simple and accurate fitting of the COM position of the cloud, and also allows for non-destructive imaging with a high SNR. Using phase-contrast microscopy, we can run our camera in "kinetics mode," where multiple images can be taken on a small region of the CCD in quick succession. We are able to take eight images in two directions before running into issues caused by the small frame size used on our CCD cameras. Acquiring multiple images per experimental cycle significantly speeds up data taking and provides a useful calibration between imaging axes. Sample images are shown in Fig. 4.9.

It is important to understand the artifacts that can occur when measuring the trap frequencies. Generally, any slosh motion aligned with a principal axis will have a constant amplitude and frequency. These oscillations are the eigenfunctions of the system, where the basis is defined by the principal axes. Measuring the slosh along an axis that is not consistent with the principal axes causes these eigenfunctions to couple as they are projected onto the new basis vectors. In a 2D system, for slosh that is driven linearly along a direction 45° away from two principal axes, any difference in the trap frequencies will lead to a dephasing of the slosh between those two axes at a rate proportional to the difference between the trap frequencies. This causes the motion to eventually become circular as it traces out a Lissajous figure, which appears as a beating between the two frequencies if the motion is observed in one dimension. In an extremely round trap, this dephasing is very slow and the motion remains approximately linear. However, the motion will also remain linear if it is aligned with one of the principal axes of the trap. To avoid any confusion, we drive an initially circular slosh motion by displacing the trap center along one axis and waiting a quarter trap period before displacing along the second axis. Sample data for a trap that is slightly out of round is shown in Fig. 4.10.

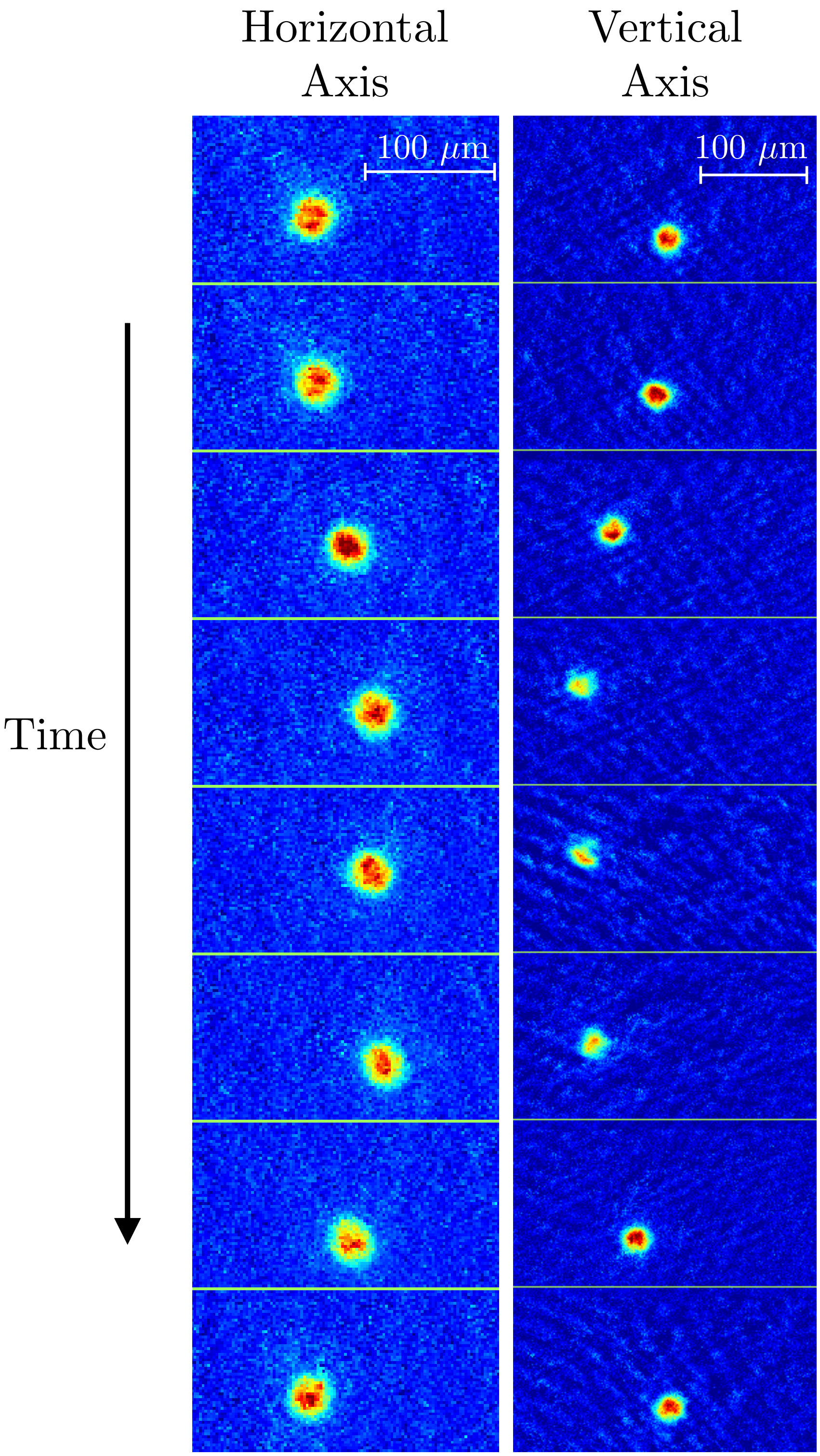

Figure 4.9: These are the raw data that are taken during each experimental cycle. Each set of eight images is taken simultaneously using phase-contrast microscopy from two orthogonal directions. The difference in cloud size between the two sets of images arises from differences in pixel size and magnification of the separate imaging systems. The images are taken in 15 ms intervals.

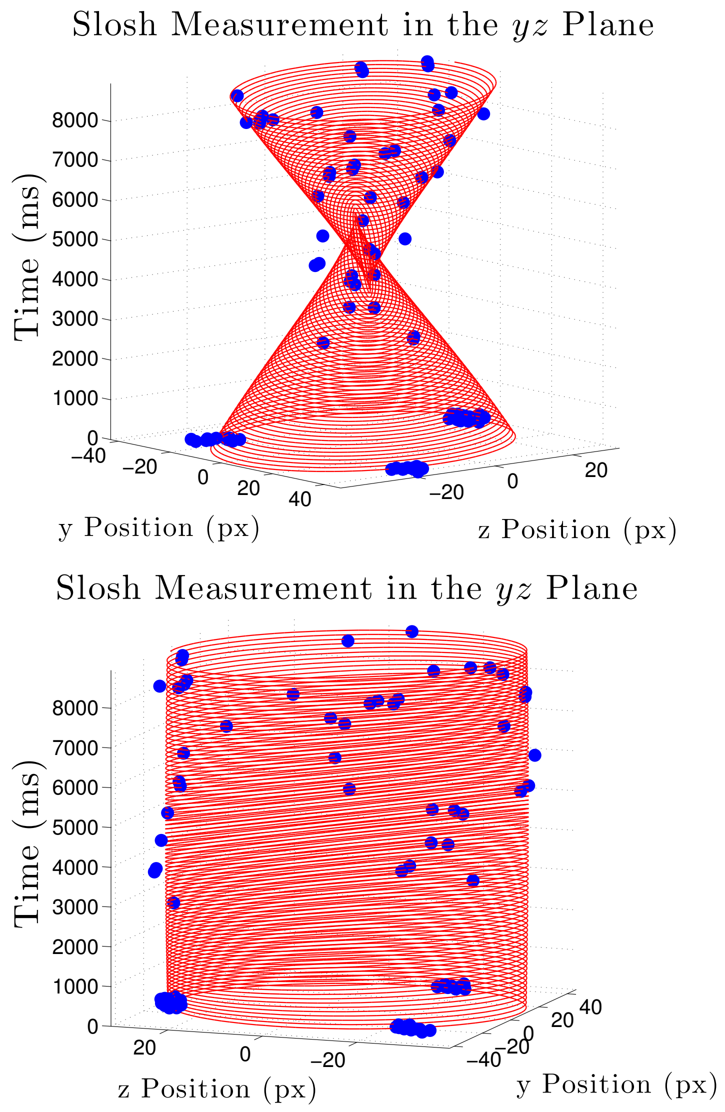

Figure 4.10: Sample data and fits of the slosh mode in the yz plane. Both sets of data are identical but viewed from a different angle. A beat frequency is visible in the first figure, while the amplitude appears constant in the figure on the bottom, indicating that the viewing angle is colinear with a principal axis. The red lines are the fits, and viewed from the top, trace out a Lissajous figure.

Our imaging beams are set up so that three of the axes of our images are approximately aligned with the three bias coils used for the rotating field and we simply define our lab frame from these imaging axes. We find that the most robust method for making the trap spherical is to detune the frequency along one of the principal axes and then round out the trap in

2D. Detuning one of the principal trap frequencies by 10% is sufficient to reduce coupling of the slosh mode driven along the other two axes. From the fits with a rotation matrix, we are able to back out the orientation and characteristic frequency of the principal axes. In other words, our data along the two imaging axes, say d_x and d_y, is fit by minimizing the following

$$\chi^2 = \sum_{i=1}^{N} \left| \begin{pmatrix} d_x^i \\ d_y^i \end{pmatrix} - \begin{pmatrix} \cos(\theta) & -\sin(\theta) \\ \sin(\theta) & \cos(\theta) \end{pmatrix} \begin{pmatrix} \mathcal{A}_x \sin(\omega_x t^i + \phi_x) \\ \mathcal{B}_y \sin(\omega_y t^i + \phi_y) \end{pmatrix} \right|^2 . \tag{4.11}$$

The superscript i indicates an element in an array of data points, for which the x and y data are determined from the same image taken at a time t^i. Taking the frequencies ω_1 and ω_2, and the rotation angle, θ, the elliptical trap profile can be solved using

$$A = \omega_1 \cos^2(\theta) + \omega_2 \sin^2(\theta) \tag{4.12}$$

$$B = (\omega_2 - \omega_1) \cos(\theta) \sin(\theta) \tag{4.13}$$

$$C = \omega_1 \sin^2(\theta) + \omega_2 \cos^2(\theta) \tag{4.14}$$

where we define our ellipse as

$$Ax^2 + Bxy + Cy^2. \tag{4.15}$$

The amplitude and phase parameters $\mathcal{A}_x$, $\mathcal{B}_y$, ϕ_x, and ϕ_y are only used to match the conditions of the drive and are not imperative in the final determination of the principal axes. We calibrate our system by varying the fields corresponding to terms in table 3.1 and fitting the elliptical coefficients measured from slosh data. The fit was used as a way of calibrating the induced ellipticity as a function of convenient experimental parameters, but the measured variation in the elliptical coefficients agrees well with theory as seen in Fig. 3.3. After the ellipticity in one plane was sufficiently shimmed out, we detuned the trap frequency along another dimension and round out another plane. This process was iterated—rounding out each plane in xy, xz, and yz individually—until the trap was spherical, which took roughly 2-3 cycles before the principal trap frequencies differed by less then 0.1%.

4.3.1 Direct Determination of Trap Frequencies and Orientation of Principal Axes

The previous method can be extended to 3D for directly determining all principal axes and their orientation without the need for detuning. When measuring slosh along a dimension that is not aligned along any principal axes, more complicated beating between the three trap frequencies is visible as shown in the simulated data in Fig. 4.11.

As with the 2D case, a least squares fit is performed using sums of sinusoidal functions. Here we define

$$\begin{aligned}
\mathcal{F}_x(t) &= \mathcal{A}_x \sin(\omega_i t + \theta_{x1}) + \mathcal{B}_x \sin(\omega_j t + \theta_{x2}) + \mathcal{C}_x \sin(\omega_k t + \theta_{x3}) \\
\mathcal{F}_y(t) &= \mathcal{A}_y \sin(\omega_i t + \theta_{y1}) + \mathcal{B}_y \sin(\omega_j t + \theta_{y2}) + \mathcal{C}_y \sin(\omega_k t + \theta_{y3}) \\
\mathcal{F}_z(t) &= \mathcal{A}_z \sin(\omega_i t + \theta_{z1}) + \mathcal{B}_z \sin(\omega_j t + \theta_{z2}) + \mathcal{C}_z \sin(\omega_k t + \theta_{z3})
\end{aligned} \tag{4.16}$$

The amplitudes $\mathcal{A}$, $\mathcal{B}$, and $\mathcal{C}$ correspond to oscillations along the principal axes with frequencies ω_i, ω_j, ω_k. The subscript indicates the projection of the oscillation onto the imaging axes $\hat{x}$, $\hat{y}$, and $\hat{z}$, in other words $\mathcal{A}_x = \mathcal{A} \cdot \hat{x}$. Each function has a variable phase, θ, but the frequencies ω_1, ω_2, and ω_3 are constrained to be the same for all three functions. Data along each imaging axis, d_x, d_y, and d_z is fit simultaneously using the method of least squares by minimizing the following function

$$\chi^2 = \sum_{i=1}^{N} \left[\left| d_x^i - \mathcal{F}_x(t^i) \right|^2 + \left| d_y - \mathcal{F}_y(t^i) \right|^2 + \left| d_z - \mathcal{F}_z(t^i) \right|^2 \right]. \tag{4.17}$$

Minimizing χ^2 is enough to determine the three principal trap frequencies, but in order to figure out the orientation of the principal axes relative to the imaging axes another step must be taken. The projection of the principal axes onto the imaging axes can be encoded by the following matrix

$$\begin{pmatrix} \hat{i} \cdot \hat{x} & \hat{j} \cdot \hat{x} & \hat{k} \cdot \hat{x} \\ \hat{i} \cdot \hat{y} & \hat{j} \cdot \hat{y} & \hat{k} \cdot \hat{y} \\ \hat{i} \cdot \hat{z} & \hat{j} \cdot \hat{z} & \hat{k} \cdot \hat{z} \end{pmatrix},$$

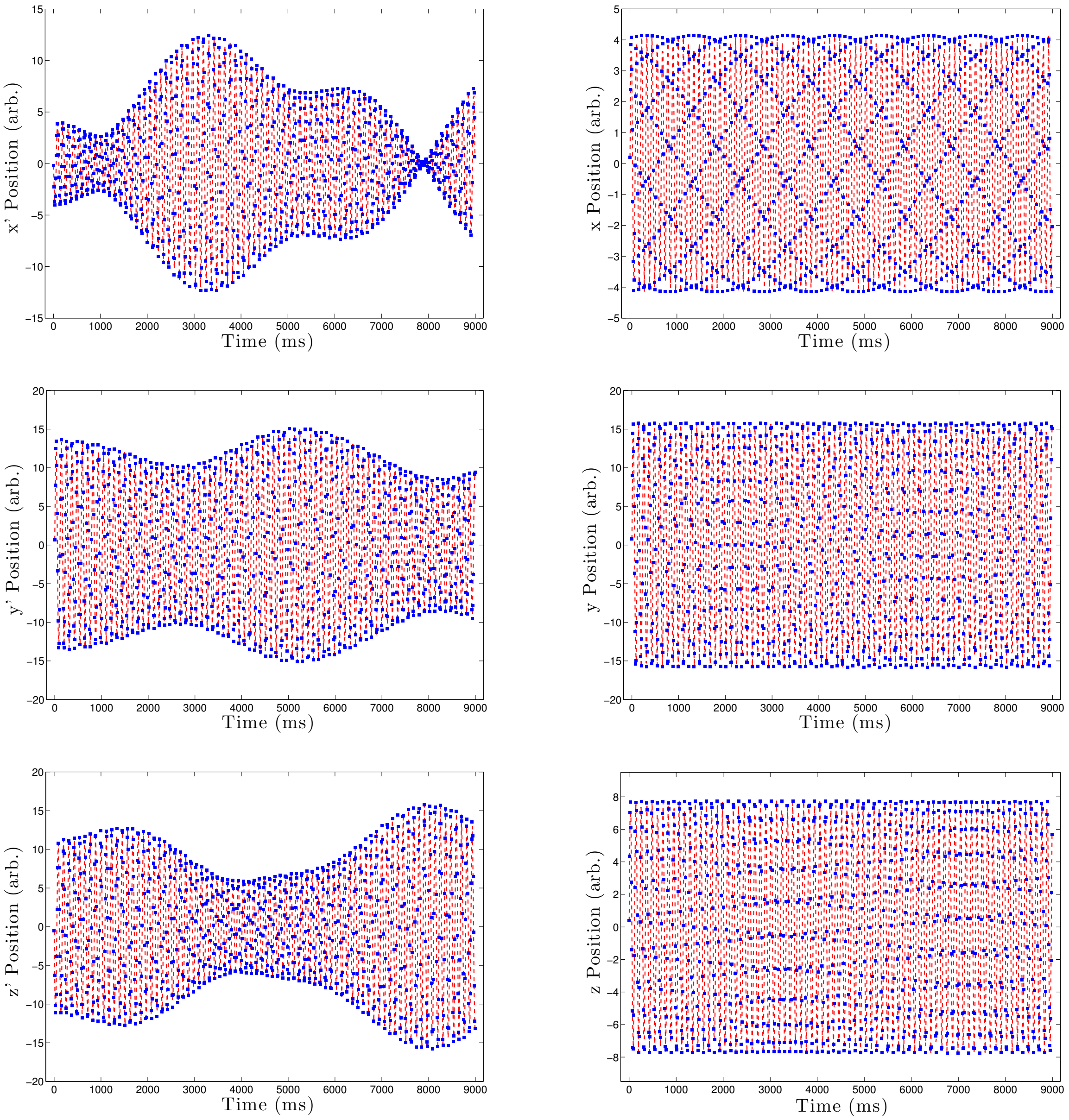

Figure 4.11: Simulated data measured along an axis other than the principal axes, where beating between the three principal frequencies can be seen. The left column shows data along 3 axes that are arbitrarily rotated from the principal axes. The right column shows the same data viewed along each principal axis. Data in the second column results from applying a rotation matrix that is determined from the methods discussed in this section.

which reduces to the identity matrix when the trap and imaging axes are aligned. Incorporating the results from the fit, the amplitudes can be written in the form

$$\mathcal{M}_{imaging} = \begin{pmatrix} \mathcal{A}_x & \mathcal{B}_x & \mathcal{C}_x \\ \mathcal{A}_y & \mathcal{B}_y & \mathcal{C}_y \\ \mathcal{A}_z & \mathcal{B}_z & \mathcal{C}_z \end{pmatrix}. \tag{4.18}$$

Here our basis is set by the imaging axes, if instead the basis is set by the trap axes the matrix becomes

$$\mathcal{M}_{trap} = \begin{pmatrix} \mathcal{A} & 0 & 0 \\ 0 & \mathcal{B} & 0 \\ 0 & 0 & \mathcal{C} \end{pmatrix}. \tag{4.19}$$

The transform between bases is simply given by

$$\mathcal{T} = \mathcal{M}_{trap}\mathcal{M}_{imaging}^{-1}. \tag{4.20}$$

Because we are not equipped with the actual values that comprise $\mathcal{M}_{trap}$, we need to diagonalize $\mathcal{M}_{imaging}$. Numerically, the most stable solution of $\mathcal{T}$ is computed using a singular value decomposition (SVD). The SVD returns three matrices such that

$$UWV^\dagger = \mathcal{M} \tag{4.21}$$

where U and $V^\dagger$ are unitary matrices and W is a diagonal matrix that is positive and real-valued. The diagonal elements in W are known as the "singular values," and can be interpreted as eigenvalues. This is one of the main benefits of using an SVD instead of just finding the eigenvectors of the system; the SVD diagonalizes a matrix and also returns the transformation that rotates into the original basis. The SVD has various uses, but is often described geometrically as a set of matrix transformations that produce an ellipsoid. In this interpretation, $V^\dagger$ is used to rotate a unit sphere into a new basis, W scales the sphere along the axes of the new basis to form an ellipsoid, and U rotates into the final basis. So, if we were to find the singular value decomposition of $\mathcal{M}_{imaging}$, then we would find that

$W = \mathcal{M}_{trap}$ with the exception that the values in W are sorted in decreasing order along the diagonal. But the singular values in W just correspond to the amplitude of the slosh oscillations, which are set by the drive amplitude and are irrelevant to the problem at hand. By replacing W with an identity matrix, we can back out the rotation between the imaging and trap frames with

$$R = UV^{\dagger}. \tag{4.22}$$

R is also unitary, meaning that the matrix that rotates $\mathcal{M}_{imaging}$ into $\mathcal{M}_{trap}$ is simply $R^{\dagger}$ in which case

$$R^{\dagger}\mathcal{M}_{imaging} = \mathcal{M}_{trap}. \tag{4.23}$$

Although the values in the $\mathcal{M}$ matrices are defined by the amplitude of oscillations, they are only a way of determining the projection of the principal axes onto our imaging axes. Once the rotation matrix has been determined, the principal axes should be instead defined in terms of the trap frequencies determined by minimizing Eq. (4.17).

The benefit of this approach lies in the experimental simplicity because individual trap axes don't need to be changed and the process can ideally be used to reduce trap anisotropy with a single set of data. In a near-spherical trap, the method is less stable when there is any noise in the data. However, when the trap frequencies differ by more than 1%, the method can be used to quickly and reliably map out the principal ellipsoid.

4.4 Driving Collective Excitations

To study the monopole and quadrupole modes, it is imperative that we can selectively excite them with minimal coupling into other modes. A particular mode is often parametrically driven by modulating the strength of the trap at the resonant frequency of the mode. However, in the collisionless limit, the monopole and quadrupole mode frequencies are degenerate and careful consideration must be taken in order to drive only one mode. Anharmonicities in the trap pose other issues, especially if the cloud has any vertical slosh.

The condition for a spherical trap depends strongly on the sag position of the atoms, and the ratio of radial to axial trap frequencies changes based on the position of the atoms along the $\hat{z}$ axis. This means that vertical slosh will couple to the quadrupole mode because of the anisotropic modulation of the trap strength. The TOP bias field, quadrupole field, and shim fields are the three tools we have for driving excitations, and adjustment of each field will couple to all three modes.

4.4.1 Dipole Mode

Driving the dipole slosh mode for characterizing trap frequencies is very straightforward. Because we care about only the COM position of the cloud, we work with small condensates for maximum signal-to-noise, so that any inadvertant excitation of the monopole or quadrupole modes doesn't affect the measurement. Instead of parametrically squeezing the trap, we excite the dipole mode by abruptly displacing the center of the trap using fields generated by large shim coils. Our iterative process of optimizing trap sphericity requires an initially circular slosh motion in either the xy, xz, or yz planes. Circular motion is excited by first shifting the trap along one axis. After a quarter period of the trap frequency the first shim field is returned to its initial value and a second shim field is applied along an orthogonal axis. The shim coils are roughly aligned along the same axes as the TOP coils so the shim fields can be adjusted more or less independently, but the fact that they are large and bulky makes them difficult to align and not perfectly orthogonal. Final values for the shim fields are roughly optimized by using the resulting slosh measurements immediately after the drive.

4.4.2 Monopole Mode

Excitation of the monopole and quadrupole modes require a less abrupt drive. The monopole mode is driven by sinusoidally modulating the strength of the trap symmetrically at twice the trap frequency. Changing the strength of the trap symmetrically can be done using only the TOP bias field. Symmetry is preserved only around the minimum of the trap, which unfortunately depends on both the TOP bias and quadrupole fields as found in Eq. (3.8). Modulation of the TOP bias field strength alone will not only drive a quadrupole mode due to the asymmetry of the trap at the position of the atoms, the atoms will also undergo vertical slosh. Sloshing can be minimized by using a very long drive, but this doesn't prevent the coupling of the drive to the quadrupole mode. The best solution is to shift the trap minimum using a vertical bias field so that it remains stationary and aligned with the cloud. This will remove any residual slosh and preserve the symmetry of the drive.

The modulation of the TOP field can be described with a small time-dependent perturbation $\xi(t)$:

$$B_0(t) = (1 + \xi(t))B_0. \tag{4.24}$$

For a spherical trap, the sag position of the atoms is

$$\mathbf{z_0} = -\frac{B_0}{B_z^{sph}}\sqrt{\frac{7}{2}}\hat{z}, \tag{4.25}$$

where B_z^{sph} is the quadrupole field gradient required for a spherical trap, and is defined by

$$B_z^{sph} \equiv \sqrt{\frac{9}{7}}\frac{mg}{\mu} \approx 34.61\frac{G}{cm}. \tag{4.26}$$

where mg is the gravitational force and μ is the magnetic dipole moment of the atoms. $\mathbf{z_0}$ is directly proportional to B_0, so the time-dependent shift in the trap minimum is $\xi(t)\mathbf{z_0}$. The vertical bias field needed to shim out the vertical slosh is given by the shift in the trap minimum multiplied by the quadrupole field gradient:

$$\begin{aligned} B_v(t) &= \xi(t)B_z^{sph}\mathbf{z_0} \\ &= \sqrt{\frac{7}{2}}\xi(t)B_0\hat{z} \end{aligned} \tag{4.27}$$

In the experiment, $\xi(t)$ is a sine wave driven for 4 periods at a frequency of 18 Hz with an amplitude of 12%. The extrema of the drive roughly correspond to trap frequencies of 8.55 Hz and 9.64 Hz for a stable trap frequency of 9.05 Hz. Ideally, shimming out the slosh with the vertical bias field should be sufficient to drive a pure monopole mode. In practice, however, a small amount of energy is put into the quadrupole mode. We reduce this coupling by modulating the quadrupole field in phase with the TOP field by roughly 5%. This value is optimized by alternately tweaking the strength of the quadrupole and vertical bias fields and minimizing the quadrupole mode and slosh amplitudes respectively. Assuming the modulation is small, the extra TOP fields used for shimming out ellipticity don't need to be changed and the resulting monopole amplitude is about 25% of the mean cloud size.

4.4.3 Quadrupole Mode

When exciting the quadrupole mode, it is important that the geometric mean of the trap frequencies is constant. Calculating the mean frequency change analytically requires another Taylor expansion of the potential. The expansion about the trap minimum summarized in table 3.2 won't give the correct results, because these terms automatically account for the new sag position of the atoms. Because the excitation frequency is faster than the trap frequency, the atoms aren't able to follow the trap minimum, and the correct form of the potential needs to be expanded around a stationary position. The instantaneous change in the average trap frequency can be calculated numerically. For a typical quadrupole drive, we dither the quadrupole field with a maximal relative shift of $\alpha = 4\%$. To maintain a constant average frequency, the TOP field must be modulated with a relative shift that is 4.424 times larger than that of the quadrupole field. Fig. 4.12 shows the change in the radial, axial, and mean trap frequencies as a function of the change in field strengths where the quadrupole and TOP bias fields shift by

$$\delta B_q = \Delta\alpha B_q \tag{4.28}$$

and

$$\delta B_0 = -4.424\Delta\alpha B_0 \tag{4.29}$$

respectively. The parameter Δ varies from -1 to 1 during the drive, where the fields are modulated sinusoidally at a frequency of 18 Hz for 4 periods such that $\Delta = \sin(2\omega_{trap}t)$. Simultaneous modulation of the quadrupole and TOP bias fields is necessary for both the monopole and quadrupole fields in practice. While the relative drive strength of each field is different in each case, the main difference is the overall sign of the modulation of the TOP bias field as shown in Fig. 4.13.

4.5 Detection

4.5.1 Fitting

To extract the quadrupole and monopole oscillation amplitudes, we measure the widths of the clouds using gaussian surface fits. Our fitting functions are defined by

$$A \exp\left(-\frac{(x-x_c)^2}{2\sigma_x^2} - \frac{(y-y_c)^2}{2\sigma_y^2}\right) + C \tag{4.30}$$

where x_c and y_c are the center coordinates and σ_x and σ_y are the cloud widths along each imaging axis. There is a small angle between our side-view image axes and our trap axes. This angle is most obvious when the quadrupole distortion is maximized, but when the cloud is nearly spherical the angle is not well defined. Using the rotation angle as a fit parameter, we were able to determine the actual rotation from quadrupole data with maximal distortion, and we fix the rotation to the resulting 5° tilt for our normal fitting routine. The fringes in our images don't cause any differences in the fits, and can be seen in the residual images in Fig. 4.14.

Phase-contrast imaging not only has the benefit of increasing our data acquisition rate, but also allows us to measure the relative monopole and quadrupole distortion in a single experimental cycle. Small variations in the initial conditions, such as temperature or atom number, would normally add noise to our measurement of the monopole mode. We use a time step of 17 ms between images to capture roughly 1.5 oscillations for both the monopole and quadrupole modes. Using a fixed frequency sine wave to fit the distortion using the six

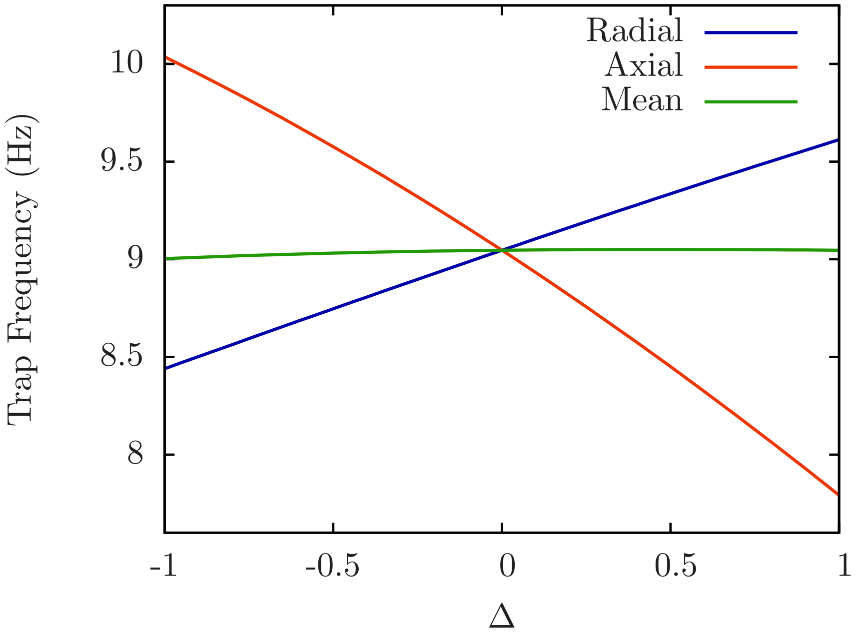

Figure 4.12: Radial, axial, and mean trap frequencies over the full range of field modulations used to drive the quadrupole mode. The maximal change in the field strength is 4% for the quadrupole field and 17.7% for the TOP bias field, which correspond to $\Delta = 1$. In the experiment, we also use the vertical bias field to minimize vertical slosh and end up changing the TOP bias field by only 13%.

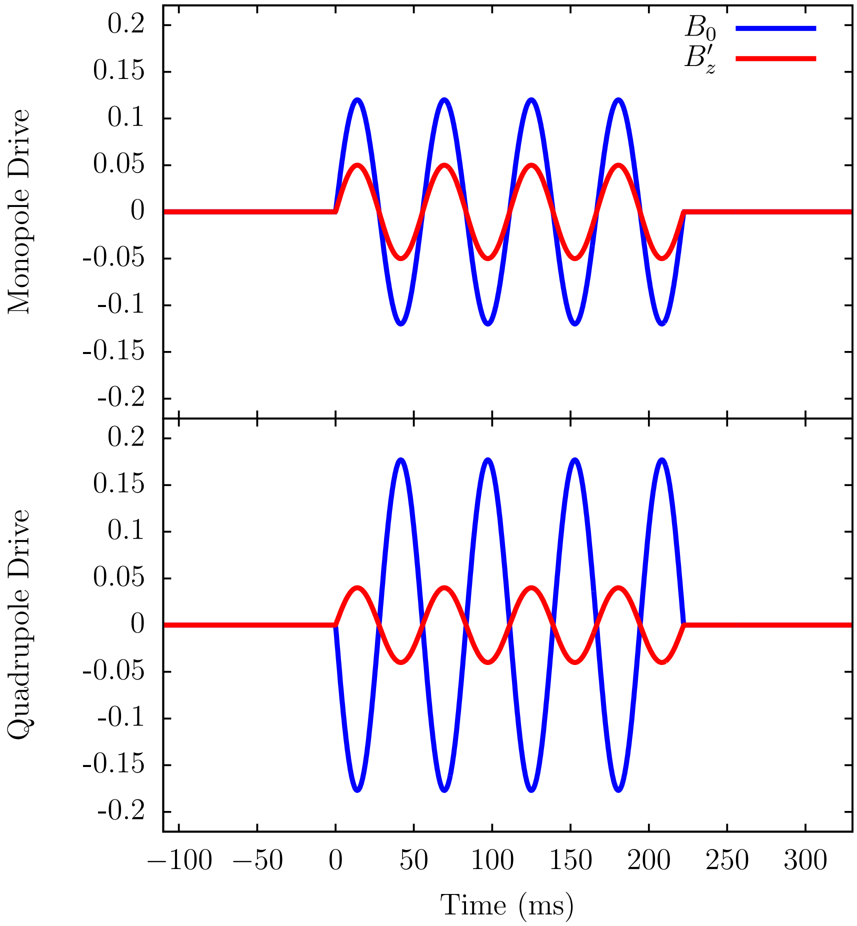

Figure 4.13: Quadrupole and TOP field modulation for driving monopole and quadrupole modes. Amplitudes are relative shifts in the overall quadrupole and TOP fields.

frames from a phase-constrast image, we can calculate the relative instantaneous amplitude of an oscillation by looking at the ratio of the amplitude to the mean. Amplitudes of the monopole and quadrupole distortion are scaled by the average width of the cloud during one cycle, given by the following relations

$$A_M = \frac{\sigma_i^2 + \sigma_j^2 + \sigma_k^2}{\langle \sigma_i^2 + \sigma_j^2 + \sigma_k^2 \rangle} - 1 \tag{4.31}$$

$$A_Q = \frac{2\sigma_k^2 - \sigma_i^2 - \sigma_j^2}{\langle \sigma_i^2 + \sigma_j^2 + \sigma_k^2 \rangle}. \tag{4.32}$$

Oscillation amplitudes are determined by fitting a cycle of oscillation in cloud width, obtained from each experimental run, with a fixed frequency sine wave as indicated by the solid lines in figure 5.1.

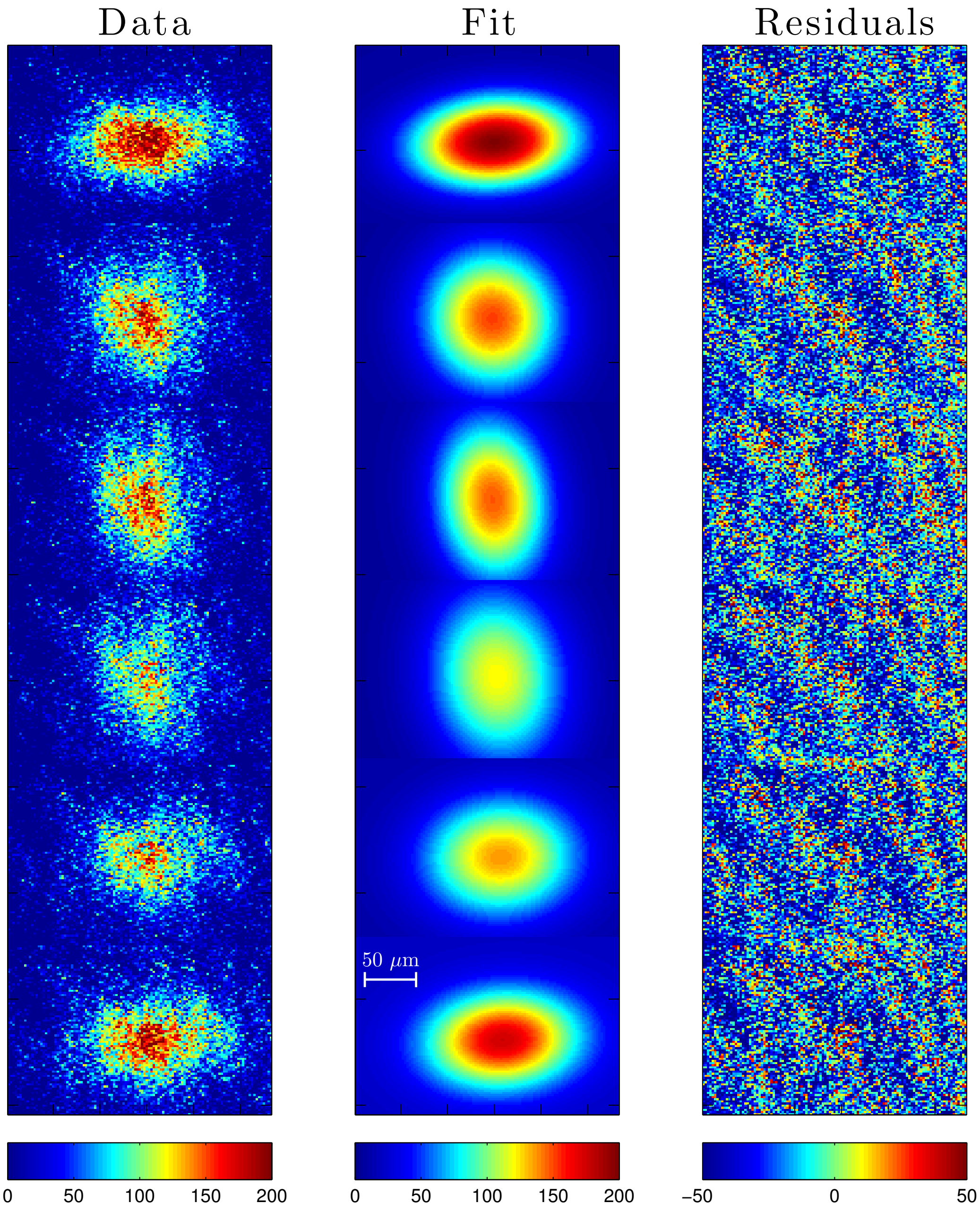

Figure 4.14: An example of raw quadrupole mode data and the associated surface fits taken during one cycle of the experiment.

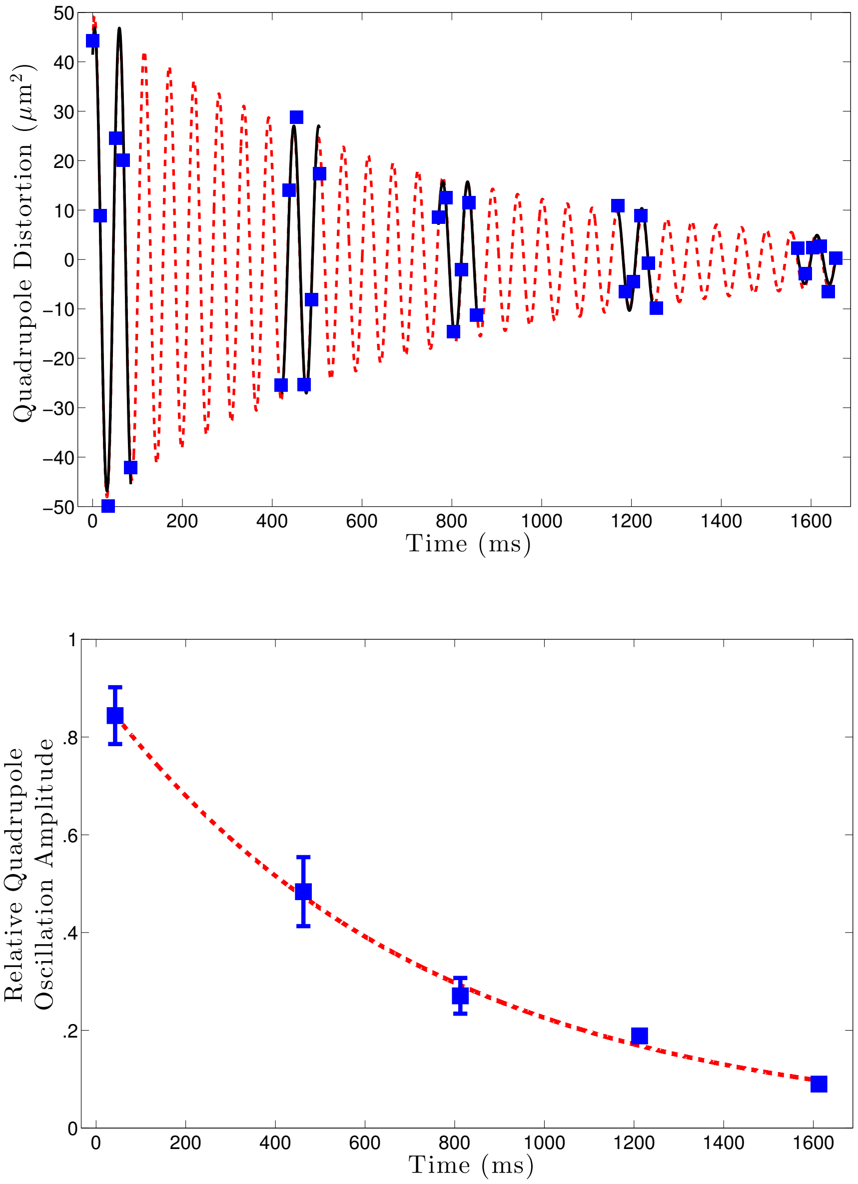

Figure 4.15: Sample data for a driven quadrupole mode in a spherical trap with residual asphericity less than 0.002 and a collision rate of 7.4(3) s^{-1}. Solid lines on the quadrupole data indicate a typical fitting procedure where individual periods taken in a single run are fit with an undamped sine wave to extract an instantaneous amplitude. The oscillation amplitudes at various cycles are in turn fit to an exponential decay to extract the damping rates. Random observable scatter in these points is predominantly due to small, irreproducible fluctuations in initial conditions.

Chapter 5

Observation of Suppressed Damping of Breathe Mode Oscillations in a Thermal Cloud

Boltzmann's prediction of the absence of damping of the monopole mode in an isotropic harmonic potential was made nearly 140 years ago. His result depended on the laws of mechanics and motivated his rigorous development of the statistical aspects of his theories. For over a century, experimental studies of gases had essentially no control over the confining potential, but were restricted to hard wall vessels. Even if experimentalists could create harmonic confinement, the depth of the potential would have to be enormous to account for temperatures of hundreds of Kelvin. Experimental study of the monopole mode in a harmonic potential has only been feasible with the advent of ultracold quantum gas techniques in the 1980s, but generating isotropic harmonic confinement hasn't been possible until now.

Although Boltzmann's prediction is a fully classical result, treating the atoms as hard spheres, an ultracold monatomic gas provides an ideal system to test his theory. As we approach the Bose-Einstein condensate transition temperature, T_c, mean-field effects can add an undesirable shift to the potential. We work at temperatures between $2T_c < T < 3T_c$ to avoid mean-field effects and also to ensure that the gas is sufficiently dilute in order that we are consistent with Boltzmann's original formulation of the transport equation. Our interatomic collision rate ranges from $2\ s^{-1}$ to $9\ s^{-1}$, which means that an atom in our $2\pi(9\text{ Hz})$ trap will typically undergo several oscillations before colliding with another atom. These short-range s-wave collisions also approximate the hard-sphere collisions used in the development of the Boltzmann equation.

Of course, we expect *some* damping as a result of our system not being totally ideal. Quadrupole damping rates serve as a baseline for comparison with any damping observed in the monopole mode. Damping of the quadrupole mode is well understood and, in the collisionless limit, the quadrupole damping rate scales linearly with interatomic collision rate as

$$\Gamma_Q \simeq \frac{1}{5}\gamma_{coll}. \tag{5.1}$$

We vary the initial atom number and final evaporation frequency to adjust the collision rate in our gas, then selectively drive monopole or quadrupole motion. The cloud is then allowed to evolve freely in the spherical trap before imaging the cloud. Six images are taken of the cloud along two orthogonal axes with an interval of 17 ms in order to sample roughly 1.5 oscillation periods.

The residual asphericity of the trap drifts with time, and we periodically retune the trap to keep the asphericity small, typically less than 0.002. Each day, we characterize the trap by taking dipole slosh measurements at the beginning, middle, and end of taking damping data. We also alternate between the monopole and quadrupole driven data after every few shots to reduce any systematic errors. Monopole and quadrupole data are taken over a range of evolution times, and three sets of data are taken at each evolution time throughout the day. Instantaneous oscillation amplitudes are measured from a single image, and the resulting amplitudes are averaged over the three different sets of data.

Suppressed damping of the monopole mode can be seen in the sample data in Fig. 5.1, and although the damping rate is small, it is nonzero. Fig. 5.1 shows only a small subset of our typical monopole data to show the contrast between the amount of damping between the two modes, and actual damping rates are acquired for up to 30 seconds of free evolution in the potential. A direct comparison of quadrupole and monopole damping rates in a near-spherical trap is shown in Fig. 5.2. The measured dependence of quadrupole on collision

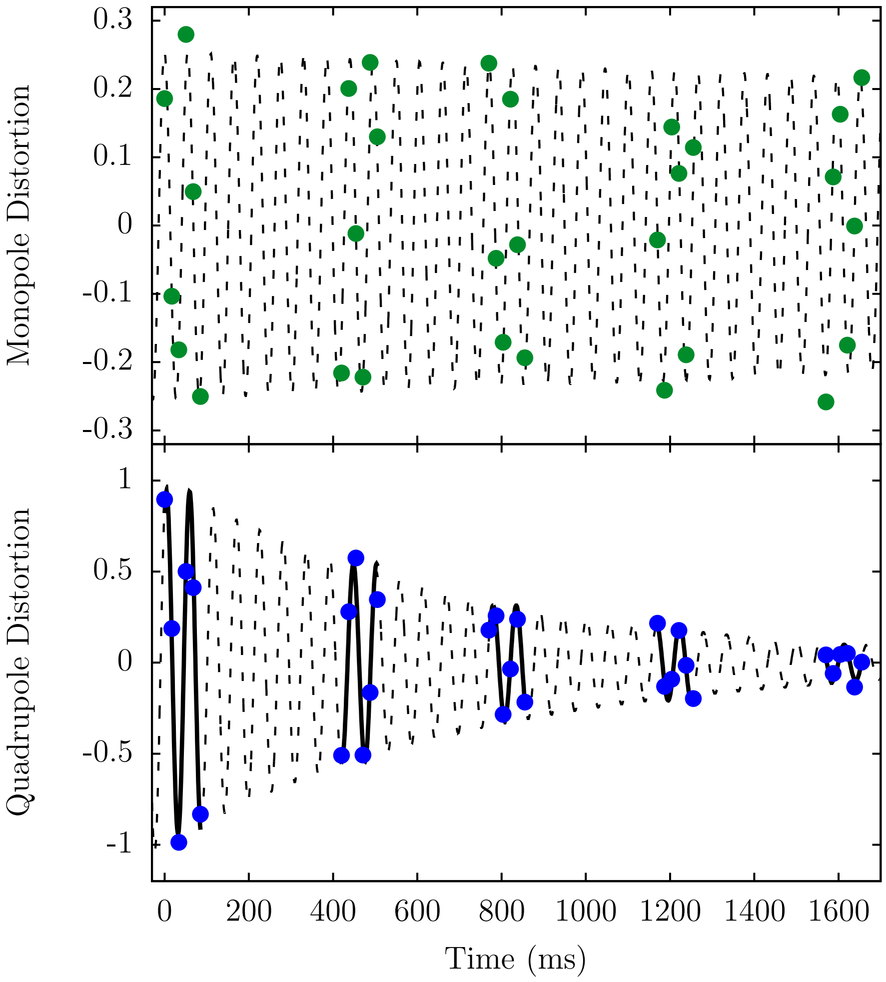

Figure 5.1: Sample data for a driven quadrupole mode and monopole mode in a spherical trap with residual asphericity less than 0.002. The normalized distortions plotted are calculated using Eqs. (4.31) and (4.32). Dashed lines indicate an exponentially damped sine-wave fit. Solid lines on the quadrupole data indicate a typical fitting procedure where individual periods taken in a single run are fit with an undamped sine wave to extract an instantaneous amplitude. The amplitudes at various times are in turn fit to an exponential decay to extract the damping rates shown in Fig. 5.2

rate is $\Gamma_Q = (4.9(1))^{-1}\gamma_{coll}$, which is in good agreement with Eq. (5.1). There is a small amount of damping in the monopole mode with an average rate of $\Gamma_M = 0.14(3)$ s^{-1}, but the damping rate is *independent* of collision rate as expected.

In order to understand the source of monopole damping, we note that Boltzmann's

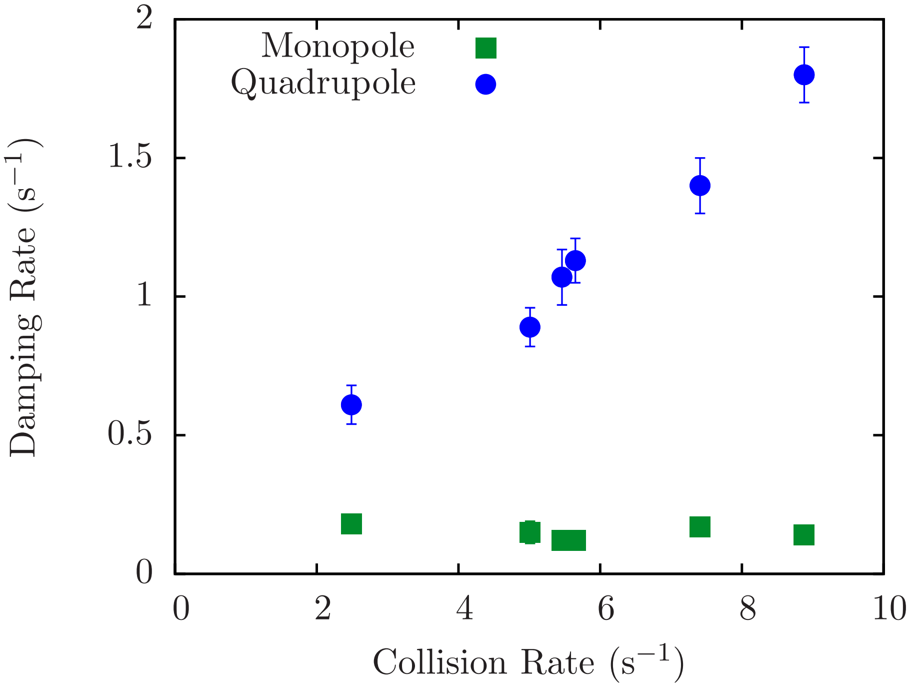

Figure 5.2: Monopole and quadrupole damping rates as a function of interatomic collision rate in a near-spherical trap. Residual asphericity was typically around 0.001, but always less than 0.0026. Cloud full width at half maximum was approximately 115 μm.

result hinges on the assumption that the potential is both isotropic and harmonic. Naturally, a real system will never satisfy both of these conditions perfectly, and the remainder of this chapter is a devoted to a discussion of the effects that small anisotropies and anharmonicities have on the monopole damping rate.

5.1 Effects of Anisotropy

Certain subtleties arise for gases in the collisionless limit when anisotropies in the potential are small enough that trap frequencies differ by less than a few percent. In a *totally* collisionless system, oscillations along the principal axes of the trap are fully decoupled and monopole- or quadrupole-like oscillations are undamped. If the principal trap frequencies differ such that $\omega_i = \omega_j \neq \omega_k$, dephasing occurs between oscillations along different principal axes and oscillations between pure monopole motion and pure quadrupole motion occurs with a period given by

$$T_{MQ} = \frac{\pi}{|\omega_k - \omega_i|}. \tag{5.2}$$

When collisions are included, the two modes become coupled and, as the population in the quadrupole mode increases, so does the damping. This effect can be seen when $T_{MQ} < 1/\Gamma_Q$, where multiple oscillations between monopole and quadrupole modes occur. Data in Fig. 5.3

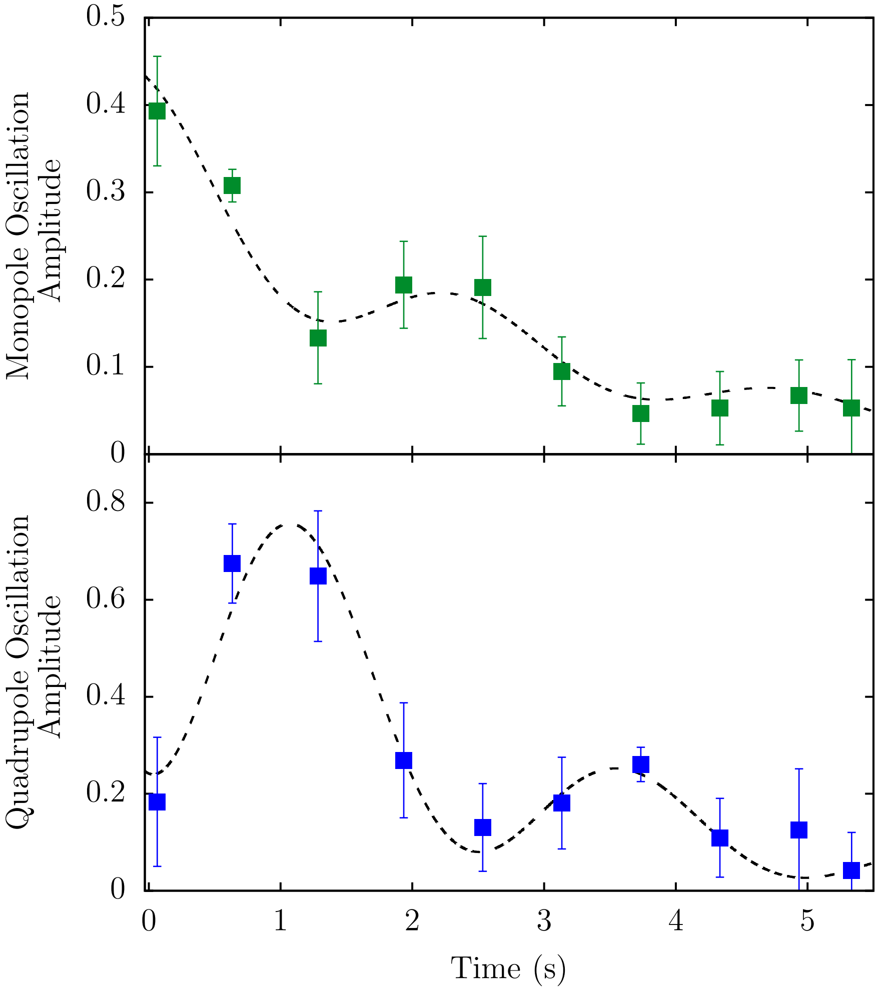

Figure 5.3: Monopole and quadrupole motion in an anisotropic trap where the residual asphericity is approximately 0.02. A monopole mode is initially driven and oscillations between the monopole and quadrupole modes can be seen. The fitting functions are given by $e^{-\gamma t}\left(\cos^2(\Delta\omega + \pi\delta_Q) + C\right)$, but should be used just as a visual guide.

show oscillations between monopole and quadrupole modes resulting from an initial monopole drive in a trap with residual asphericity of approximately 0.02. Oscillations of the individual modes are π out of phase and the damping rates for both modes are nearly equal, with a mean value of $\Gamma = 0.36(4)$ s^{-1}. The collision rate is roughly 3.7 s^{-1} leading to an expected quadrupole damping rate of 0.74 s^{-1} in a spherical trap, which is twice the value of the measured damping rate in the anisotropic trap. This is no surprise because the quadrupole mode is effectively populated only half of the time, leading to the factor of 2 decrease in the damping rate. If we decrease the amount of anisotropy such that $T_{MQ} >> 1/\Gamma_Q$, the quadrupole mode damps before it can fully couple back into the monopole mode. One can see this effect in Fig. 5.1, where the quadrupole mode damps before it can couple with the monopole mode. Fig. 5.4 shows a summary of driven quadrupole and monopole modes in traps with varying degrees of anisotropy. As we approach the spherical limit, mode coupling is no longer visible and both modes damp exponentially.

The data in Fig. 5.2 were taken in traps with residual asphericities ranging from 0.0005–0.0026, corresponding to 10.7 s$< T_{MQ}/2 <$ 55.6 s. The typical relaxation time for the monopole mode in these traps is $\tau_M = 7(2)$ s. While one could argue that this relaxation time agrees with the most anisotropic case, where the monopole mode had enough time to couple with the quadrupole mode, it cannot account for the data taken in more isotropic potentials, for which the damping is nearly the same. Thus, there must be another source of damping. It should also be noted that the results shown in Fig. 2.3 predict a damping that is two orders of magnitude smaller than what we observe. There also appears to be no correlation between the damping rate and residual anisotropy for our monopole data in a near-spherical trap. Fig. 5.5 shows the same monopole data in Fig. 5.2, but plotted against anisotropy. Thus, some other physical effect must provide the dominant source of residual monopole damping.

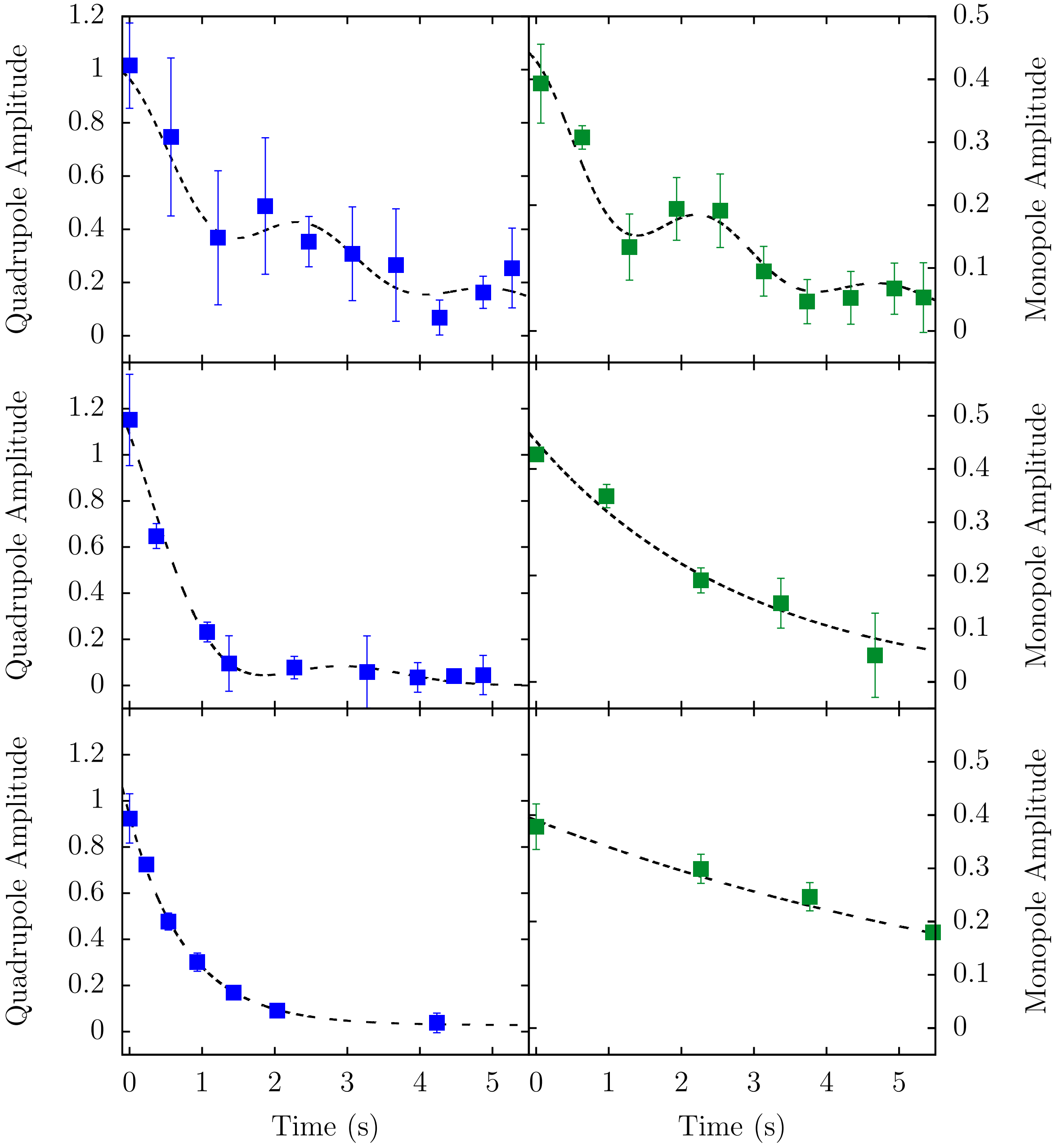

Figure 5.4: Monopole and quadrupole motion in traps with anisotropies of 0.0222 (top), 0.0133 (middle), and 0.0028 (bottom). Data on the left show driven quadrupole motion, while data on the right show driven monopole motion. As the level on anisotropy decreases, the mode coupling turns off and the decay of each mode becomes exponential.

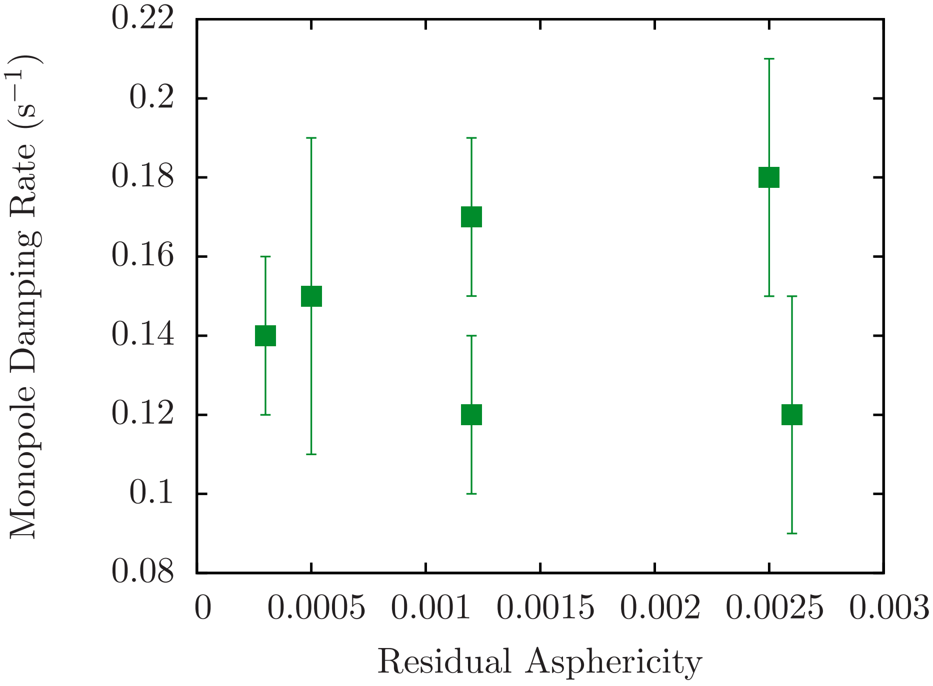

Figure 5.5: Monopole damping rates in very isotropic traps as a function of residual asphericity. The data shown are the monopole damping data from Fig. 5.2.

5.2 Effects of Anharmonicity

We now come to the second condition of Boltzmann's result, which requires that the potential be harmonic, and discuss the effect of anharmonic perturbations to our trapping potential as a source of damping. Amplitude-dependent frequency shifts caused by anharmonic perturbations lead to dephasing of individual particle trajectories, effectively damping of the collective monopole amplitude. Moreover, the anharmonic corrections to our potential are asymmetric, giving rise to an amplitude-dependent anisotropy. A calculation of the expected damping rate that takes into account all of the relevant anharmonic corrections is difficult. But the effect can be explored experimentally by measuring the monopole damping as a function of cloud size. Fig. 5.6 again shows the same monopole damping data from Fig. 5.2, but plotted against the average cloud FWHM. In this case, there does appear to be a slight increase in the damping rate as a function of cloud size. However, it is difficult to draw any conclusions from these data alone.

Just as we deliberately broke the symmetry of the trap to investigate the effects of anisotropy, we can look at monopole damping rates for extremely large clouds. Fig. 5.7 shows data for cloud widths that are up to twice the FWHM of our typical samples. The first point in Fig. 5.7 is calculated from the average cloud size and damping of the monopole data in Fig. 5.2. The trend of the data in Fig. 5.7 suggests that the damping seen at a cloud size of 115μm may be due to the onset of anharmonic effects. Unfortunately, we are unable to work with smaller clouds due to limitations in the signal-to-noise ratio of our imaging system.

While the damping is highly suppressed, the small but finite relaxation of the monopole mode is an artifact of small anharmonic perturbations to our trap, which decrease with cloud size. We find that, in the limit of zero anharmonic shifts, the damping of the monopole mode vanishes, as predicted by Boltzmann in 1876 [7].

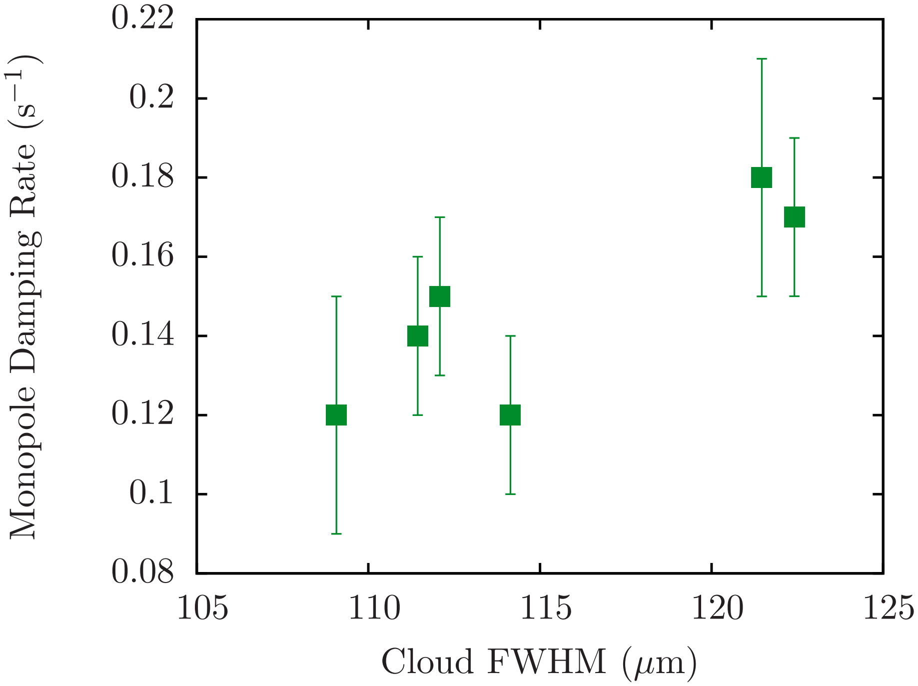

Figure 5.6: Our same monopole data from Fig. 5.2 are revisited, but this time plotted against the average FWHM of the clouds. The FWHM is calculated from the average of all of the breathe data after the clouds have been driven in order to account for the small amount of heating induced by the drive.

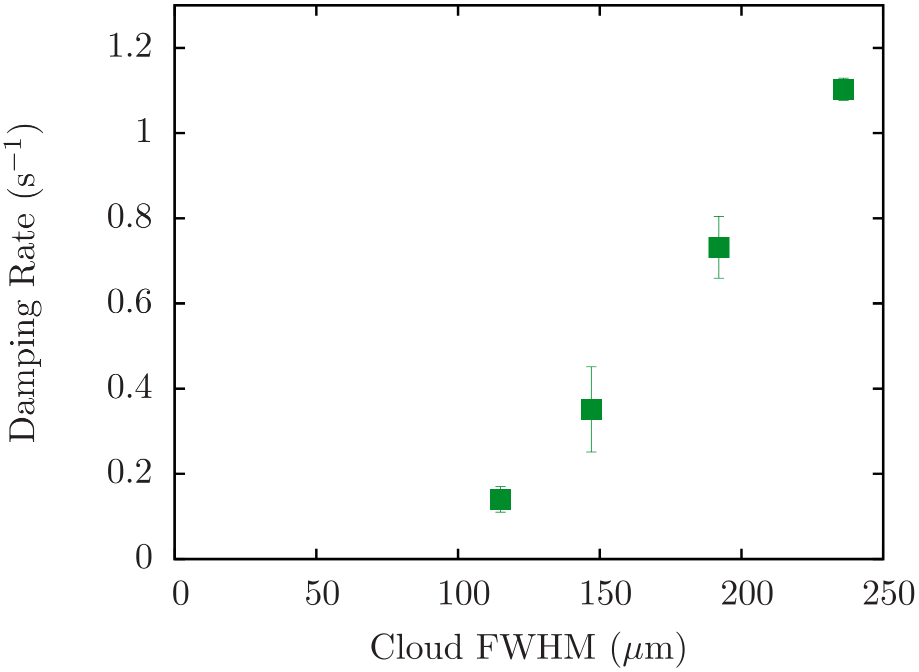

Figure 5.7: Damping of the monopole mode in a near-spherical trap as a function of the spatial extent of the atom cloud. The fractional amplitude of the excitation is the same for all points. Consistent with anharmonicity-induced damping, we see the observed damping rate decreases rapidly for smaller clouds, but the trend of the data suggests that even for the smallest clouds (such as those used in Fig. 5.2) the residual damping observed may be due to the onset of anharmonic effects.

Chapter 6

Monopole Mode Measurements in a Finite-Temperature BEC

One great feature of an isotropic harmonic potential is that complex and computationally demanding theories can be greatly simplified through symmetry considerations. An unresolved problem in the world of BEC physics is an accurate, yet accessible, theory of the interactions between the normal and condensed components of a finite-temperature condensate. There currently exist numerous, competing finite-temperature models [49], which in many cases are difficult to adapt to the irregularities that can often arise in experimental systems. Collective modes in a finite-temperature condensate are complicated not only by the fact that mean-field interactions modify the potential, but the effective potential is different for the condensate and the thermal atoms. A profile of a finite-temperature condensate is shown in Fig. 6.1 where the thermal atoms (red) no longer have a gaussian profile, but are pushed away from the center because of the presence of the condensate. Monopole oscillations for a condensate have a modified frequency that approaches $\sqrt{5}\omega$ in the Thomas-Fermi limit due to mean-field effects. In a finite-temperature cloud, however, the thermal atoms will still breathe at a frequency of about 2ω with a slight variation caused by the mean-field. As the two components dephase, they start beating together leading to damping and revivals of the mode [34].

Experimentally, distinguishing a thermal atom and a condensate atom is impossible, and correctly fitting surface data is a very difficult task. However, before decommissioning the experiment, we decided to take some finite-temperature condensate monopole data and

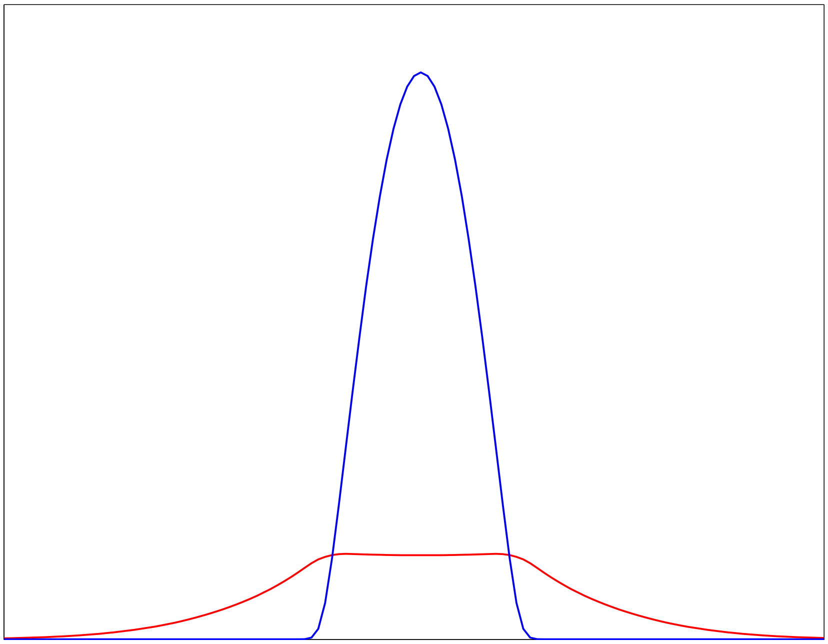

Figure 6.1: Profile of a simulated finite-temperature condensate in a harmonic trap. The condensate atoms are shown in blue and the thermal atoms in red. Mean-field interactions modify the potential, pushing the thermal atoms away from the condensate. This particular simulation uses the ZNG model for a condensate at a temperature $T = 0.75T_c$ [1].

provide our results here for anyone who wants to use them. Each set of data is taken using the same imaging and drive parameters specified in chapter 4. We use a simplified surface fit defined by the sum of a gaussian and an integrated Thomas-Fermi profile, defined by

$$f = max\left[A_{BEC}\left(1 - \frac{(r-r_c)^2}{S_r^2} - \frac{(z-z_c)^2}{S_z^2}\right)^{\frac{3}{2}}, 0\right] \tag{6.1}$$

$$+ A_{th}\exp\left(-\frac{(r-r_c)^2}{2\sigma_r^2} - \frac{(z-z_c)^2}{2\sigma_z^2}\right) + C. \tag{6.2}$$

Despite having the wrong functional form, this function fits to our data surprisingly well. Sample surface fits are shown in Fig. 6.2 and the residuals are small and the background is relatively flat, both for undriven data and monopole data. For comparison, Fig. 6.3 shows the first frame after both the data and fit have been azimuthally averaged about the center

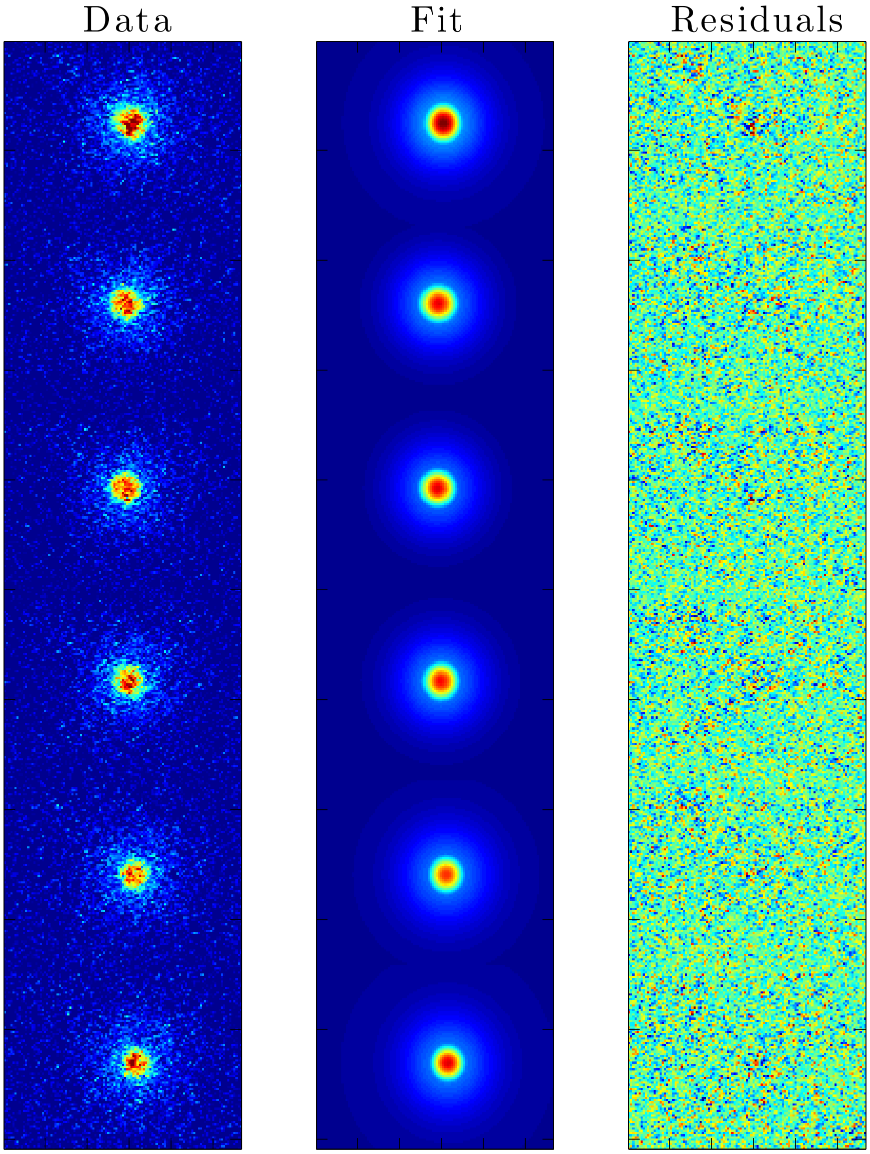

Figure 6.2: Surface fits to raw data using Eq. (6.2). No drive was used for this particular set, but the fits work equally well for driven data. The surface fits are shown in the center column and the residuals are shown in the righthand column.

position of the cloud. The variables A_{BEC} and A_{th} are the fit amplitudes for the Thomas-

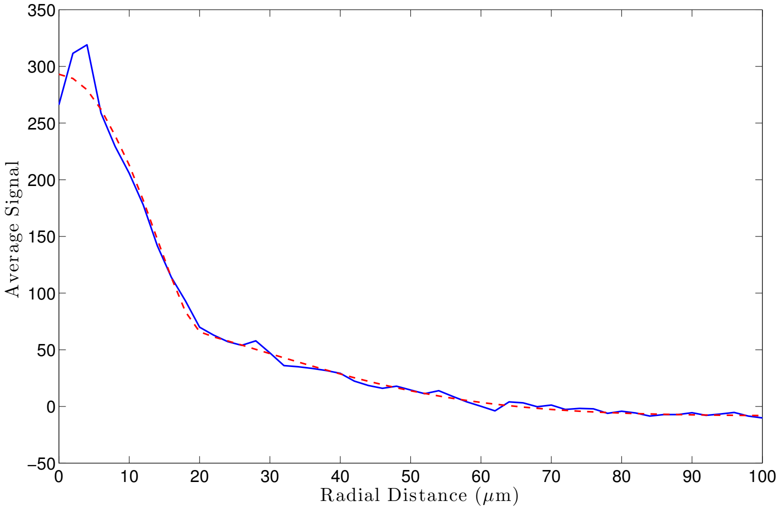

Figure 6.3: Azimuthally averaged data (blue solid line) and surface fit (red dashed line) around the center position of the condensate.

Fermi and gaussian surfaces respectively. Widths of the condensate, S_r and S_z, and thermal cloud, σ_r and σ_z, are given in microns. The radial widths with the r subscript are measured along an axis that is 45° relative to our x and y TOP coils. Images were taken along two axes for our thermal breathe experiments, but due to an issue with our top-view laser that became more problematic when these sets were taken, it was not used for most of these data. However, images that *were* taken from the top showed that the oscillation was extremely symmetric in the radial plane. The final variable in Eq. (6.2) is C, and is simply added to correct for any offsets in the background signal on the images.

It is clear that we see damping and revivals of the monopole mode. The effect is less marked for the thermal component, and damping is most clearly seen in the condensate oscillations. Deviations from a simple beat are in part caused by our simplified surface fitting function. At different phases of the oscillation, our Thomas-Fermi function is presumably fitting to some thermal atoms as well. This is obscured by the fact that our images are integrated along one dimension. Attempts at extracting reasonably quiet data from an inverse Abel transform of our images proved difficult, and to reduce the noise in our data the idea was abandoned. The monopole oscillation data (for the BEC component only, given by the average TF radius $\langle S \rangle$) are shown on the next several pages, and compared with the following fitting function

$$e^{-\gamma t}\left(\cos^2(2\pi f t + \delta) + c\right) \tag{6.3}$$

which was also used for our anisotropic thermal data. Individual periods are fit to sine wave oscillations with the frequency fixed at 20 Hz, compared to a mean trap frequency of 9.05(3) Hz with a residual anisotropy less than 0.003. For each set, we list the BEC fraction N_0/N, where total atom numbers are on the order of 10^5. Actual values for the data plotted are given in appendix A.

These data is provided "as is" and we make no claim about what sort of behavior we expect to see or whether or not the data is in agreement with any particular theory. However, we hope that these data will be of some use to theorists who are looking for a simplified system that can be used to test different finite-temperature theories.

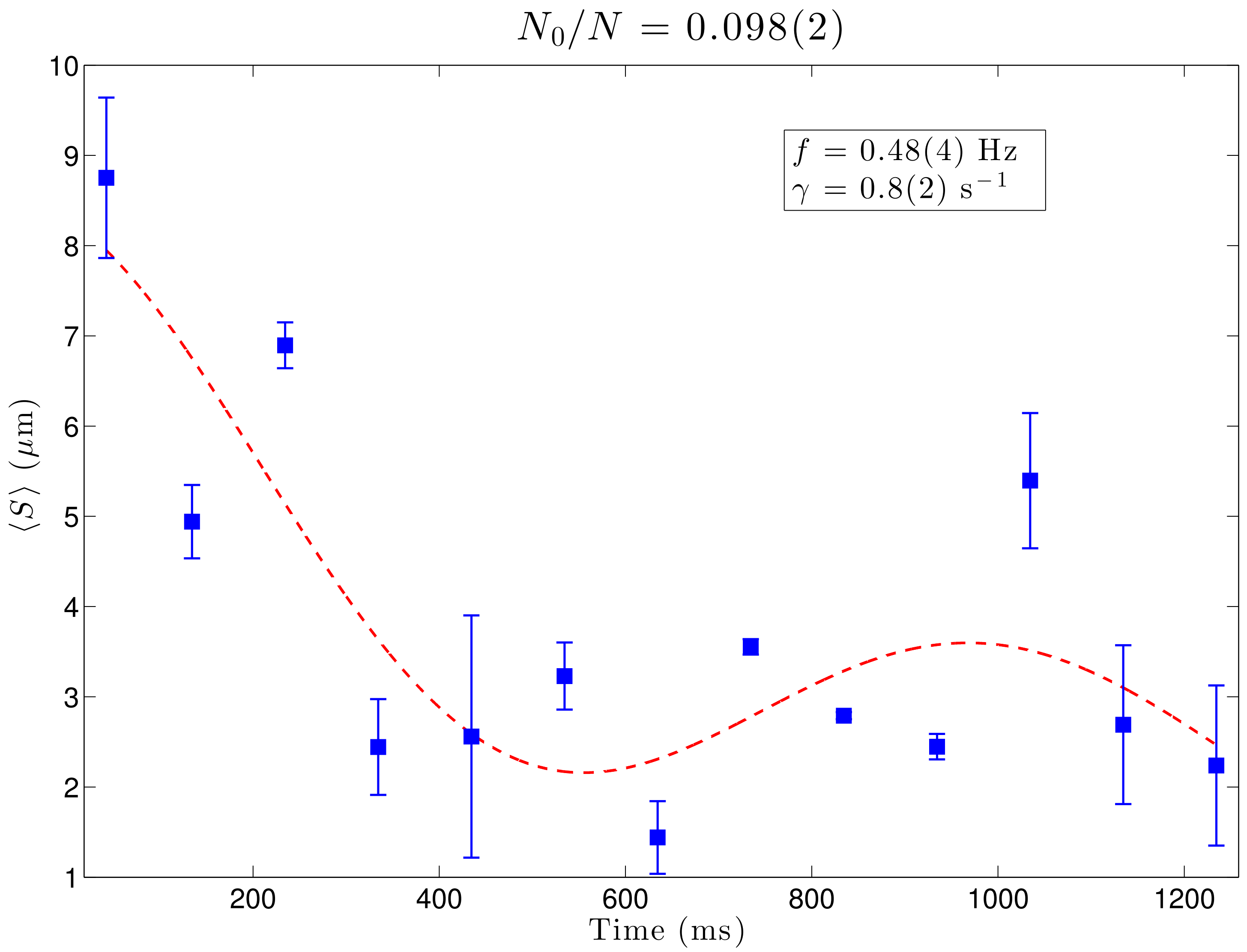

Figure 6.4: Condensate damping for a BEC fraction of $N_0/N = 0.098(2)$, $N = 9.1(1)\times10^5$

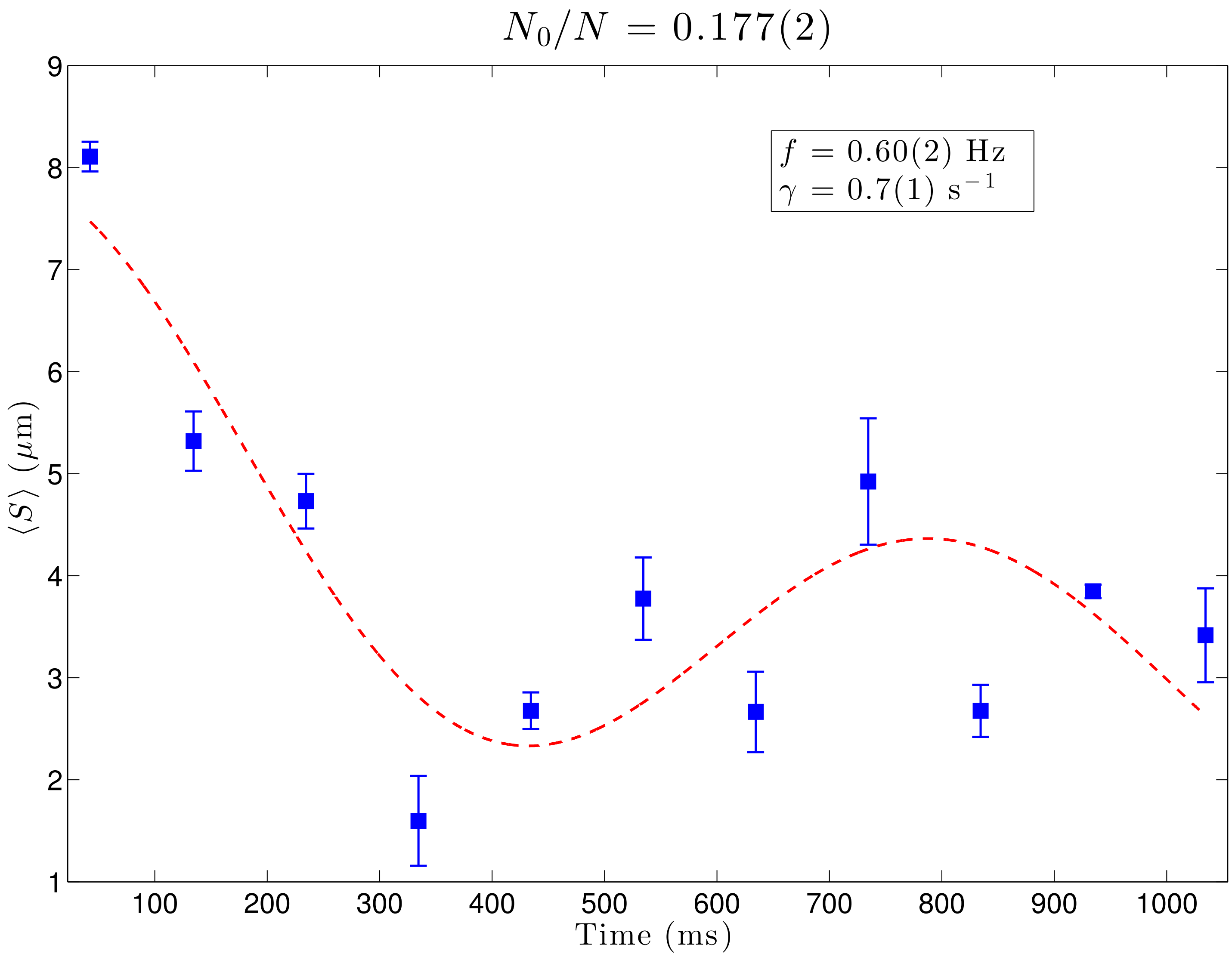

Figure 6.5: Condensate damping for a BEC fraction of $N_0/N = 0.177(2)$, $N = 7.9(1) \times 10^5$

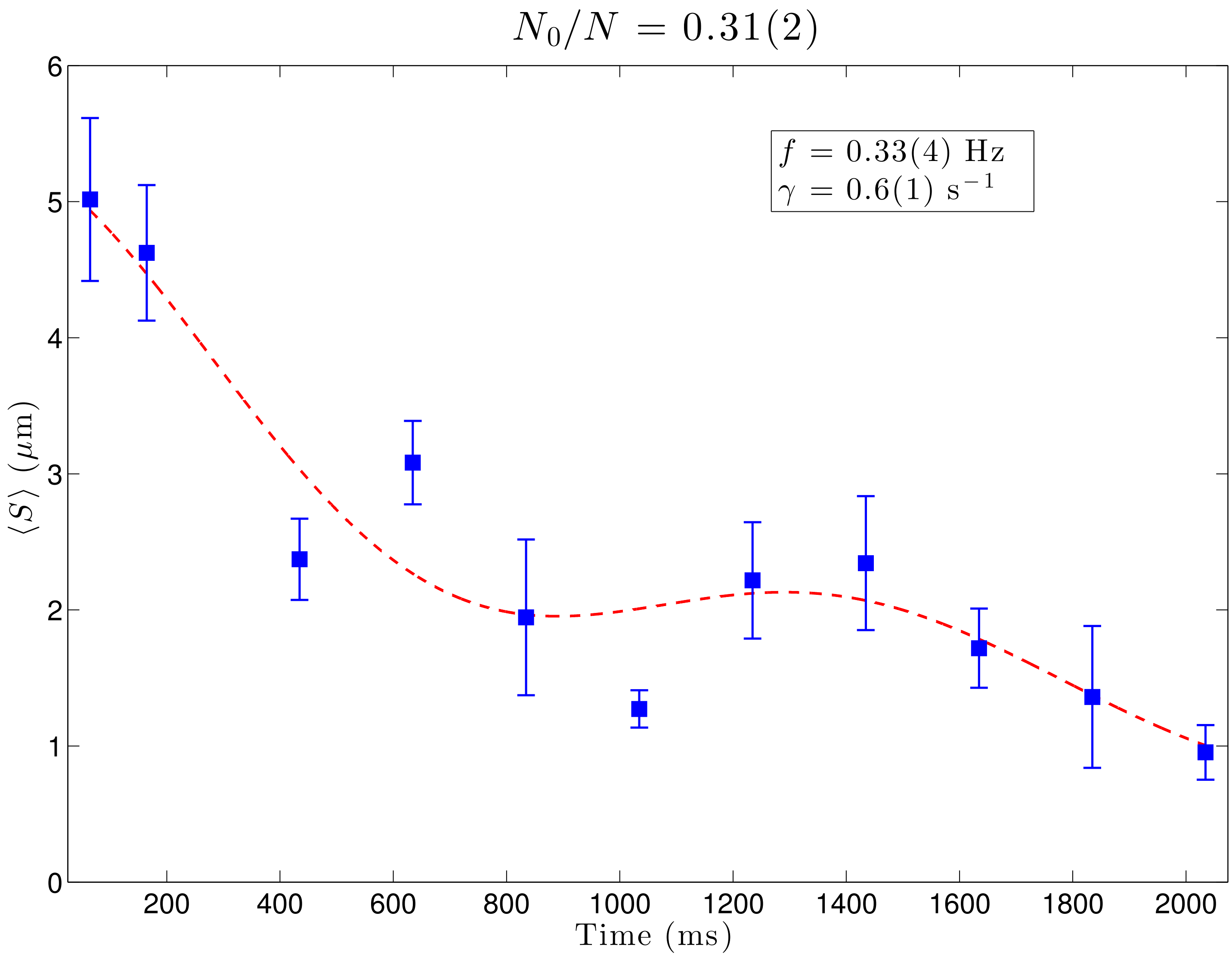

Figure 6.6: Condensate damping for a BEC fraction of $N_0/N = 0.31(2)$, $N = 5.4(2)\times10^5$

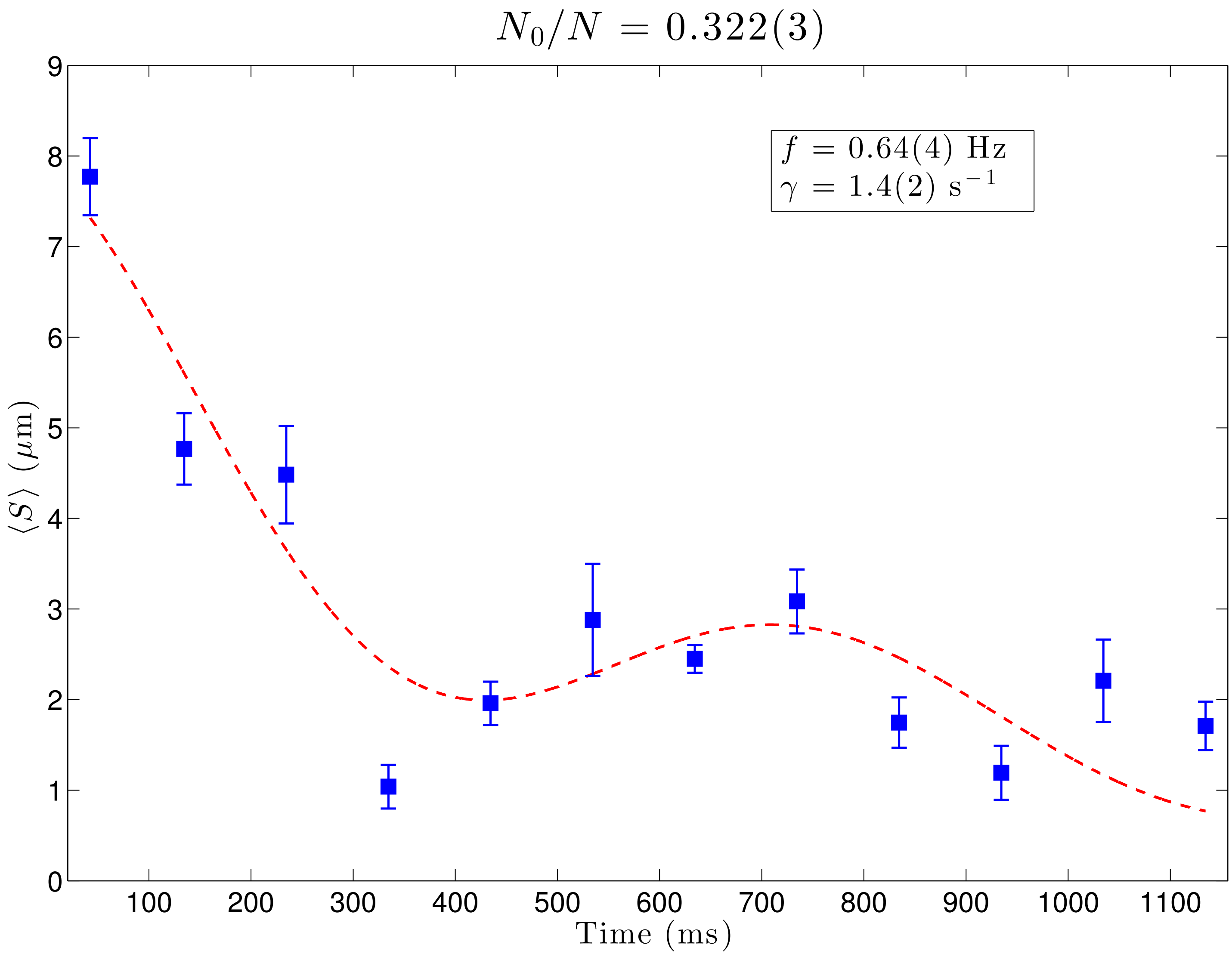

Figure 6.7: Condensate damping for a BEC fraction of $N_0/N = 0.322(3)$, $N = 6.7(1)\times10^5$

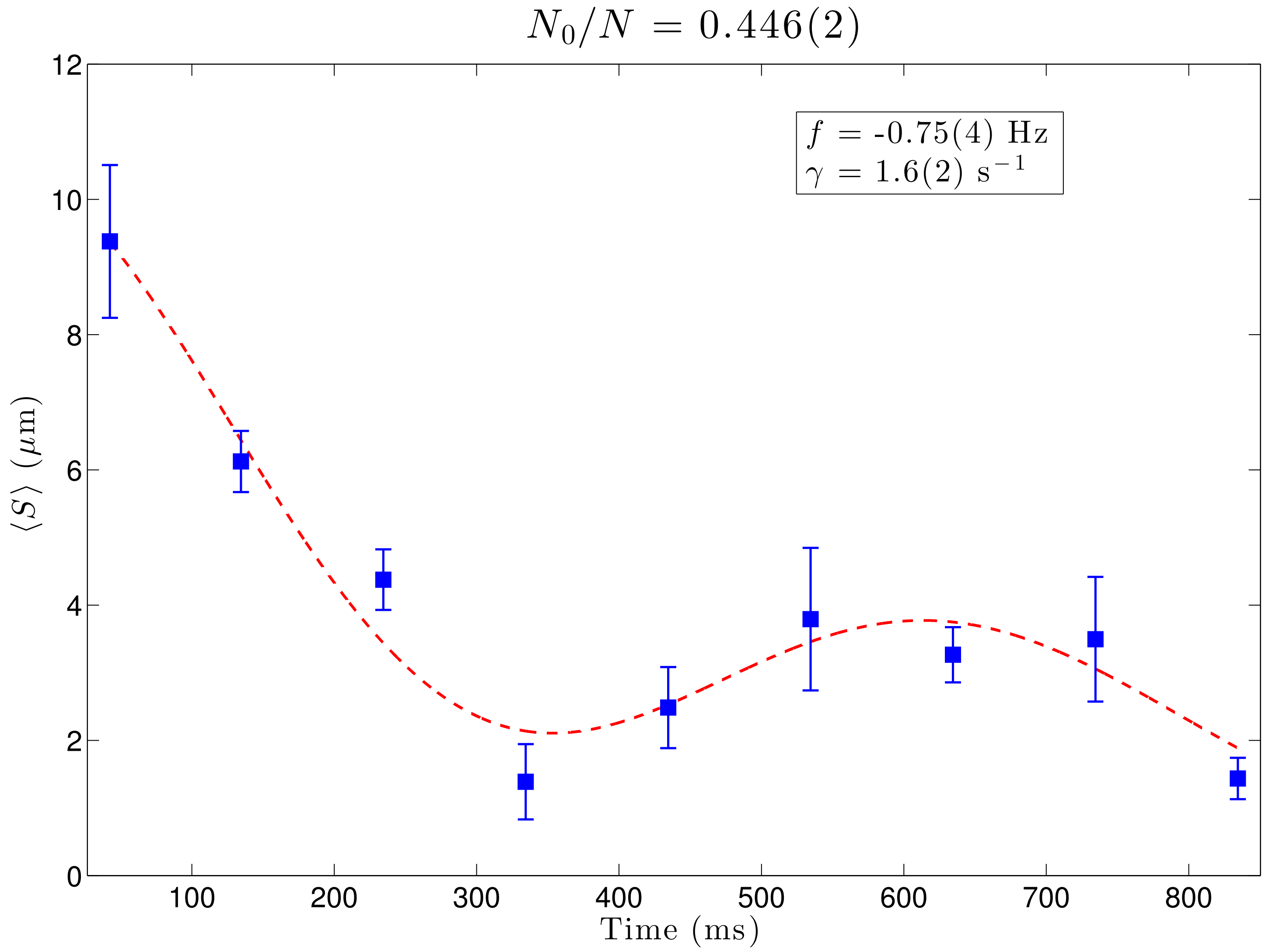

Figure 6.8: Condensate damping for a BEC fraction of $N_0/N = 0.446(2)$, $N = 9.7(1)\times10^5$

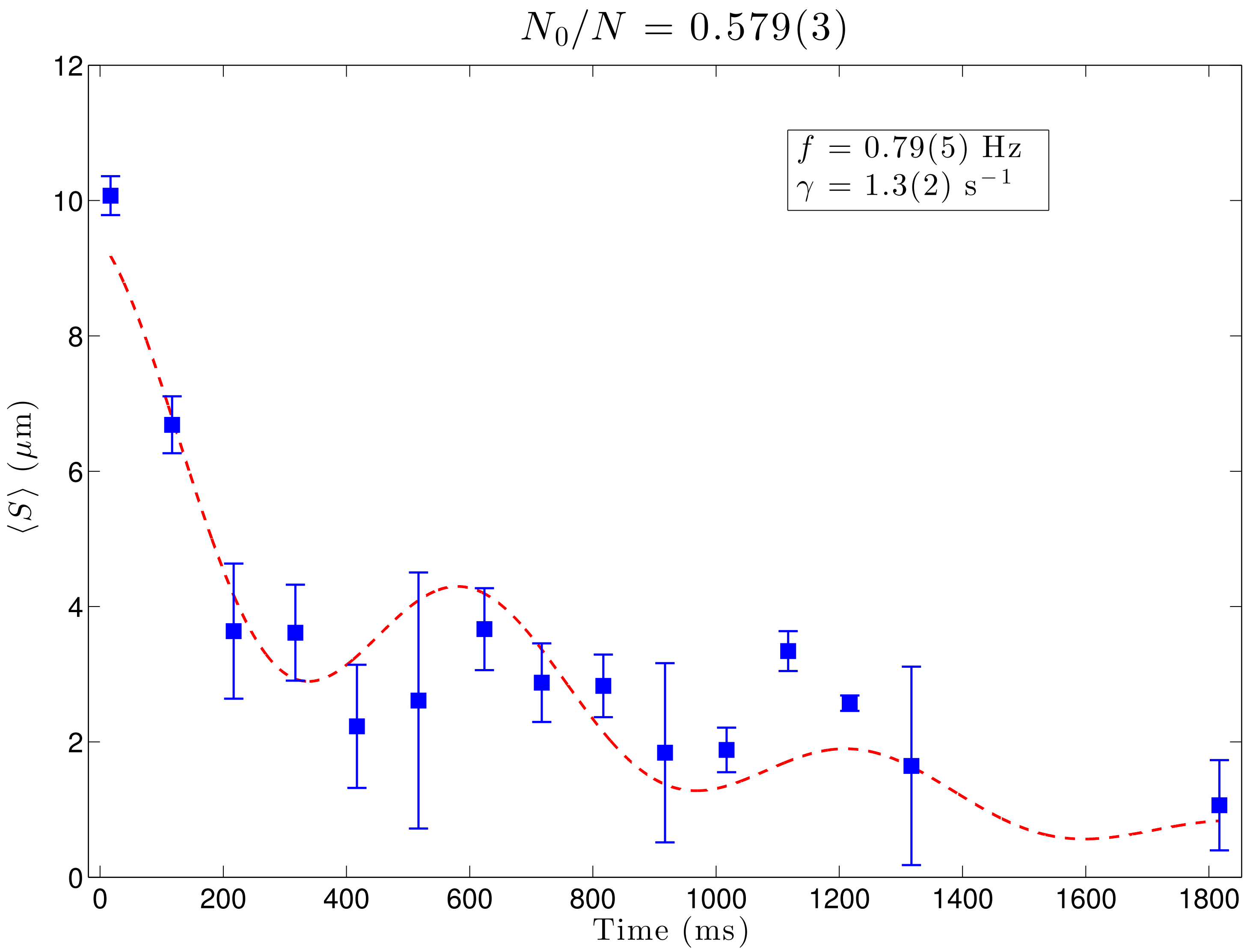

Figure 6.9: Condensate damping for a BEC fraction of $N_0/N = 0.579(3)$, $N = 8.9(1)\times10^5$

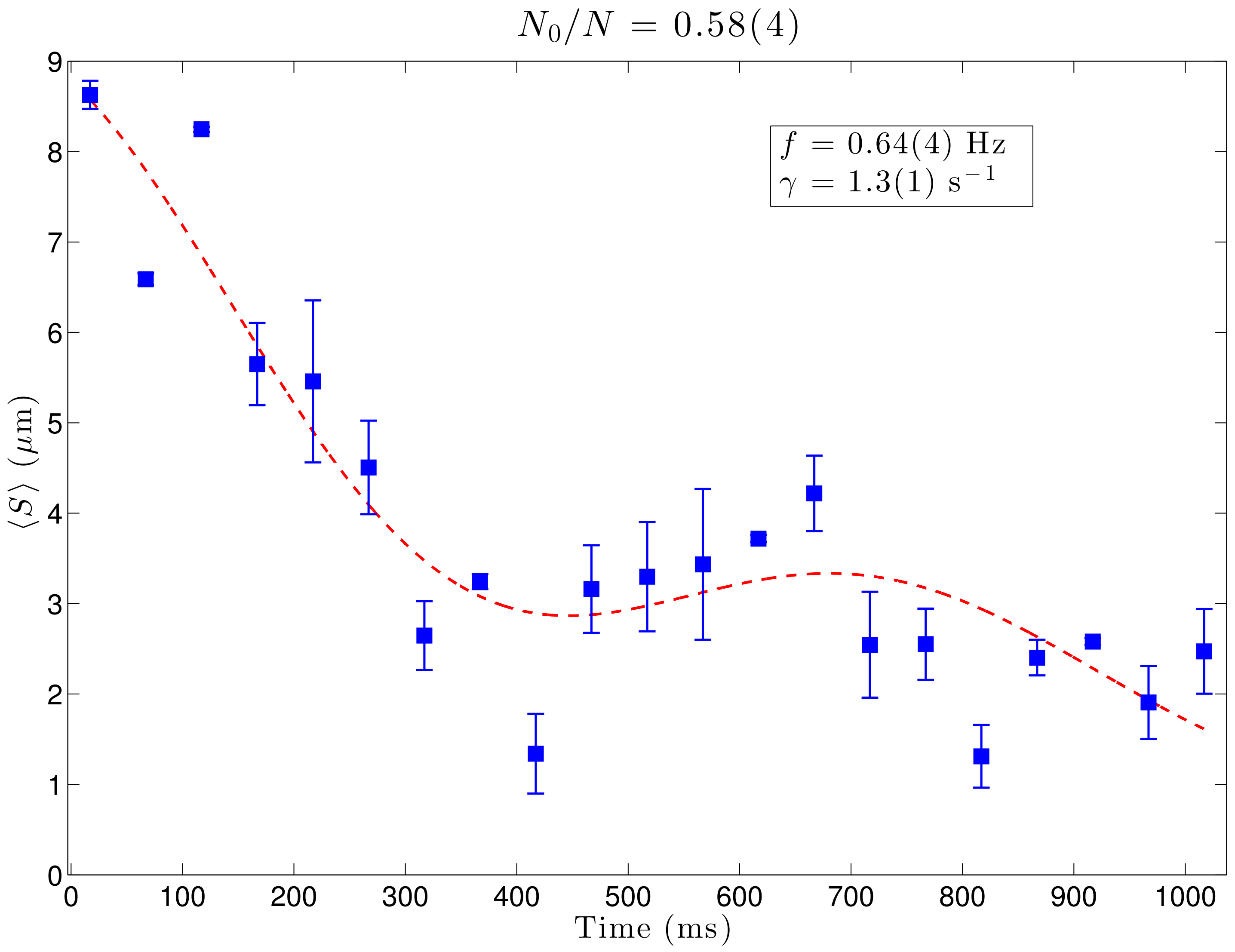

Figure 6.10: Condensate damping for a BEC fraction of $N_0/N = 0.58(4)$, $N = 8.7(2)\times10^5$

Chapter 7

Anharmonic Shearing

Prior to our spherical trap experiments, the apparatus was configured to generate quasi-2D BECs. These quasi-2D condensates are formed using an optical lattice where a 3D condensate is separated into multiple 2D layers. One of the biggest obstacles with the quasi-2D experiments is rooted in our detection procedure. Due to the geometry of our setup, our imaging laser passes through multiple quasi-2D condensates. To image a single layer, we use a special microwave pumping process that allows atoms in a single lattice site to be selectively imaged. This detection technique suffers mainly from two limitations: inefficient state transfer and instability between experimental cycles. Limited transfer efficiencies of roughly 10% were suitable, if not beneficial, for some of our previous experiments [60]. But our microwave pumping method requires that the magnetic field strength at the center of the condensate is consistent between experimental runs. Variations in the field strengths, position of the condensate, or even the phase of the lattice often lead to unusable or inconsistent data that pose more significant issues for some of our subsequent experiments.

Accounting for these problems with our microwave pumping proved to be an extremely difficult task. However, we came up with a solution that circumvented these issues entirely by using the anharmonic shifts in our trap to our advantage. By turning up the strength of the anharmonic terms, we devised a method of spatially separating, or “anharmonically shearing,” quasi-2D condensates on different lattice sites. It is perhaps ironic that we were able to address one problem in our system by enhancing another problem, but the result is a tool that is potentially useful for a variety of experiments. This chapter will first discuss certain key aspects of our quasi-2D setup[1] and some of the detection issues in greater detail as well as describe the anharmonic shearing process.

7.1 Quasi-2D Condensate Formation

Magnetic traps are useful for creating smooth, stable confining potentials but are incapable of providing the tight confinement necessary for a 2D geometry. On the other hand, optical dipole traps are immensely useful for generating complicated and exotic trap geometries for ultracold neutral atoms [25]. Atoms in an optical dipole trap interact with far-detuned light via an induced electric dipole moment. This interaction is attractive for red-detuned light and repulsive for blue-detuned light. A focused, red-detuned laser is ideal for providing quasi-1D confinement, also known as a "cigar trap." Quasi-2D confinement, or a "pancake trap," can be achieved using a variety of methods. One technique uses a holographic plate to generate a blue-detuned beam with a TEM_{01} profile [56, 52]. Another method uses an evanescent wave to create a gravito-optical surface trap [54]. In our experiment, quasi-2D confinement is provided by a 1D optical lattice in which a periodic potential is produced by interfering two laser beams [6]. Superimposing the interference pattern onto a 3D condensate causes it to separate into a series of quasi-2D condensates occupying adjacent lattice sites.

Lattice potentials have a variety of applications, such as understanding condensed matter phenomena [22, 35, 24] or quantum computation [10]. These applications take advantage of the fact that multiple lattice sites are occupied, but for studying a single quasi-2D condensate it is necessary for the depth of the lattice potential to be large enough that intersite interactions are turned off. In practice, 1D optical lattices are often generated using a retroreflected laser beam in which case the spacing between lattice sites (lattice constant) is $\lambda/2$, where λ is the wavelength of the laser. Tunneling is typically an issue if the lattice

---

[1] For a complete treatment of the quasi-2D experimental setup see [61]

constant is small and, in order to study a single quasi-2D condensate, tunneling must be minimized as much as possible. The lattice constant, d, can be changed by varying the angle between two interfering laser beams, θ, where

$$d = \frac{\lambda}{2\sin\left(\frac{\theta}{2}\right)}. \tag{7.1}$$

To maintain the sensitive control of the radial confinement we get from the TOP fields, we use a vertically oriented blue-detuned lattice as depicted in Fig. 7.1. Our lattice beams are 532 nm and interfered at an angle of 8°, which gives a lattice constant of 3.8 μm. It is imperative that we have sensitive control over the lattice beam power in order to adiabatically load the atoms into the lattice. We are afforded precise control of the lattice intensity by adjusting the power transmitted through the first order of an acousto-optic modulator (AOM). This beam is then coupled into a high-power single-mode polarization-maintaining fiber fitted with coreless end caps and cooling fins so that we can inject up to

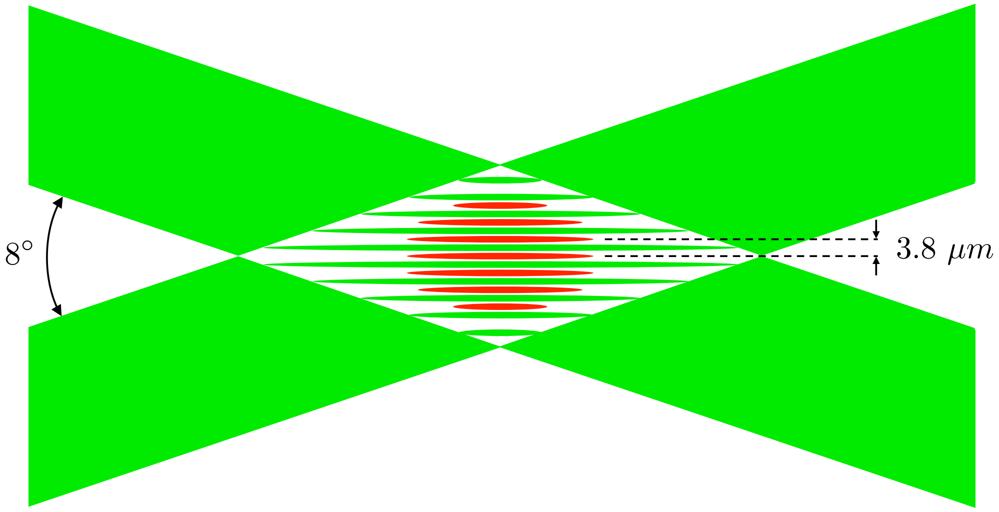

Figure 7.1: Diagram of our lattice beam set up as viewed from the side. The quasi-2D condensates are shown in red and confined to the nodes of the interference pattern. Roughly 10 lattice sites are occupied on average.

2W of power. On the output end of the fiber, we monitor the power using a photodiode, which provides a feedback signal for a power servo connected to the AOM. A diagram of the experimental setup is shown in Fig. 7.2.

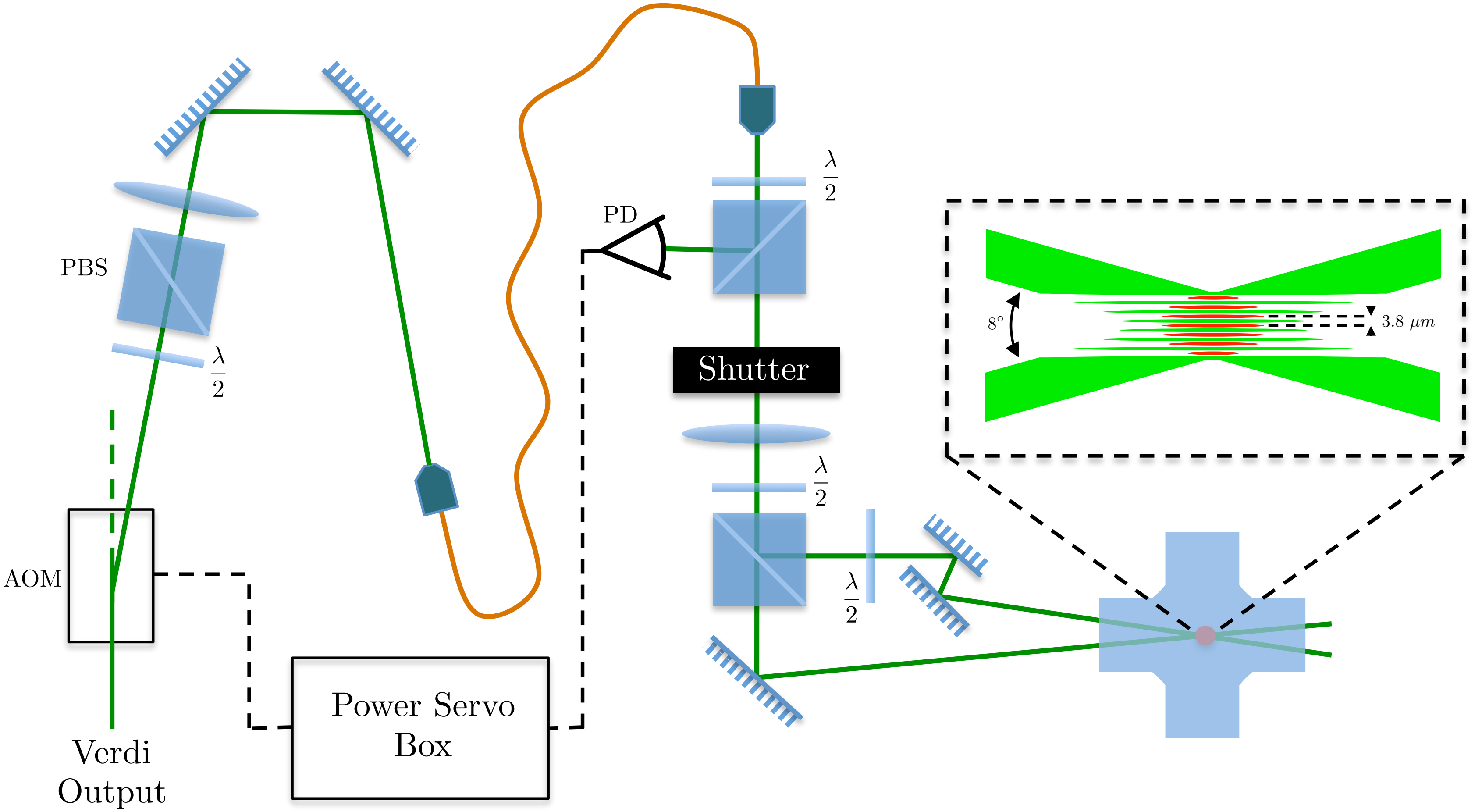

Figure 7.2: Diagram of our lattice beam set up as viewed from the side. The quasi-2D condensates are shown in red and confined to the nodes of the interference pattern. Typically about 10 lattice sites are occupied

Temperature drifts cause the fiber alignment to change, so we optimize the alignment for maximum input power of 2W, but typically work at powers closer to 1.6-1.8W when running the experiment. Optimizing the fiber coupling at a higher power ensures that the dynamic range of the the lattice beam intensity is not limited by small fluctuations in the coupling efficiency. At the output of the fiber, a small amount of power is diverted toward the photodetector that provides an error signal for the feedback on the input power. The remainder of the output is split into two beams with equal power using a polarizing beam splitter (PBS). Each beam has roughly 400 mW of power and are each focused at the center of the trap with horizontal and vertical beam waists of 225 μm and 84 μm respectively.

For most of the experimental sequence, the lattice beam is blocked by a shutter while a 3D condensate is created. Even when the system is idle, we inject most of the available power into the lattice fiber to maintain a stable temperature and alignment. Once the evaporation sequence finishes, the BEC is adiabatically loaded into the lattice by ramping the set point from 0 to 400 mW over the course of 500 ms. After loading the condensate into the lattice, evaporation is no longer possible, partly because our evaporative profile removes atoms from the bottom of the trap but also because of the slow rethermalization rate of 2D clouds. Alignment of the lattice is also simplified since the evaporation is an entirely independent process.

Rough alignment is performed by blocking one of the lattice beams and measuring the condensate displacement once the power is ramped on. The single beam alignment is optimized when the condensate appears to have expanded symmetrically and is not pushed in any particular direction. This procedure is then repeated with the second beam. The second step is to maximize the contrast of the interference at the center of the atoms. Measuring the contrast directly isn't possible because the interference is centered in our vacuum system. Instead, we maximize the trap frequency along the direction of tight confinement, which is proportional to the contrast of the interference pattern. The axial frequency in the lattice is roughly 1.4 kHz, and cannot be determined from conventional slosh mode measurements.

However, modulating the strength of the lattice potential at twice the trap frequency will parametrically heat the atoms and provides a useful tool for determining the trap frequency.

After heating is observed, we measure the width of the cloud and repeat the measurement at a slightly different modulation frequency. The final cloud widths are compared over a range of modulation frequencies and fit with a gaussian to determine the trap frequency. Small tweaks in the alignment, focus, and power balance of the lattice beams are made, repeating the modulation procedure each time, until the trap frequency is maximized. This process can be very time consuming for the initial alignment, but after the maximum trap frequency has been determined it is straightforward to correct for small misalignments.

7.2 Single-Site Detection

Our standard method of imaging uses a microwave transition to pump atoms in a single layer into a state that is resonant with our imaging laser. These experiments used absorption imaging, which was necessary for our state-dependent detection. We take advantage of the quadrupole field gradient, which in these experiments is B'_z =78 G/cm, so that the microwave transition has a spatial dependence. Atoms in a single lattice site are pumped from $|F=1, m=-1\rangle \rightarrow |F=2, m=-1\rangle$, as shown in the level diagram in Fig. 7.3. Once the microwave pulse is applied, we quickly remove the quadrupole and TOP fields and image on an $|F=2\rangle \rightarrow |F'=3\rangle$ cycling transition. We apply a microwave pulse with a gaussian temporal profile that is matched to the width of a single layer in frequency space. The center frequency is resonant with the $|F=1, m=-1\rangle \rightarrow |F=2, m=-1\rangle$ transition, and the width of the envelope is 50 μs. In frequency space, the width of the microwave pulse is approximately 4 kHz, compared to a lattice spacing of 40 kHz. The calculated frequency width of the pulse is shown relative to the lattice spacing and condensate size in Fig. 7.4 Constraints on the width of the gaussian pulse and a maximum microwave power of 30 dBm limits the pumping efficiency to around 10%. Absorption images have a much larger SNR than phase-contrast images, but, for optically thick clouds, the absorption signal will

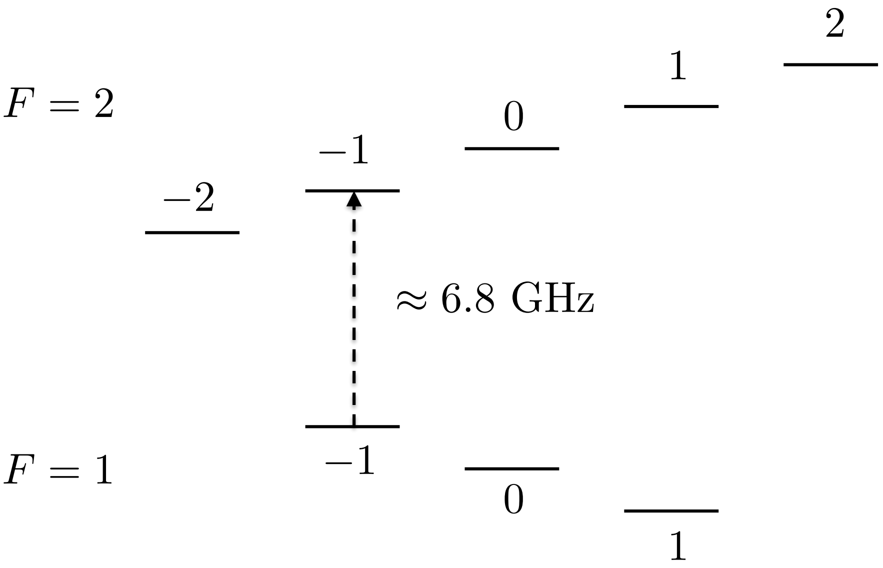

Figure 7.3: Diagram of the energy levels for the $5S_{\frac{1}{2}}$ state of ^{8}7Rb. The microwave transfer is shown with the dotted arrow and is centered at a frequency of approximately 6.8 GHz.

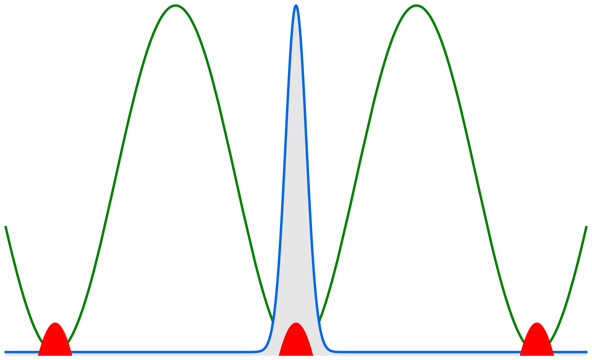

Figure 7.4: Calculation of the microwave transfer pulse (blue) in frequency space relative to the optical lattice (green) and condensate (red) size.

eventually saturate causing image distortion. By transferring only a small percentage of the atoms to a detectable state, nonlinearities associated with large optical depths (ODs) were removed [61, 51].

Small transfer efficiencies were also beneficial for a second detection technique we used for imaging the momentum-space distribution of atoms without normal time-of-flight (TOF) methods. Probing the momentum distribution of a cloud typically requires that the atoms are pumped into an untrapped state, effectively removing the external potential, and waiting for a long time so that the atoms spatially separate by an amount proportional to their individual momenta. TOF methods have a couple drawbacks in practice. Long expansion times come at the cost of image distortions such as vignetting [37], and mean-field energy adds additional momentum for condensates or especially dense clouds. In lower dimensional systems, the momentum-space distribution can be imaged directly by harnessing the mean-field energy. We use a 2D analog of a momentum-space "focusing" technique developed by Shvarchuck et al. [55] for a 1D cigar condensate confined to an optical dipole potential. In their experiment, they abruptly turned off the optical trap and let the atoms expand into a magnetic potential. The magnetic potential, which was used to provide confinement along the elongated dimension, was set up so that the trapping frequency in the direction of the tight confinement produced by the optical trap was twice the trap frequency along the elongated $\hat{z}$ direction. Upon releasing the atoms from the optical trap, the mean-field energy was preferentially transferred to the transverse momentum states, allowing the longitudinal distribution of atoms to fall toward the center of the trap once the mean-field potential had vanished. The aspect ratio of the trap is set so that the time it takes for atoms in the condensate to move to the center of the trap along $\hat{z}$ is the same amount of time it takes for the atoms expand radially and fall back towards the center of the trap in $\hat{r}$, as shown in Fig. 7.5. Probing the condensate after a quarter period of an oscillation along $\hat{z}$, $\frac{1}{4}T_z$, ideally provides the exact momentum distribution, which is described by a delta function, but mean-field effects begin to turn back on as atoms approach the center of the trap. By transferring most of the atoms into an untrapped or antitrapped state, the mean-field effects are vastly diminished resulting in a distribution that closely resembles a delta function.

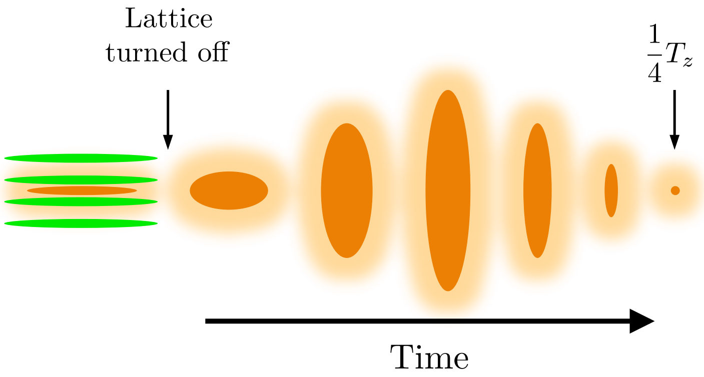

Figure 7.5: Diagram showing the expansion process used for the momentum-space focusing technique. Mean-field energy causes a lower-dimensional condensate to expand in the direction of tight confinement into a magnetic potential with an aspect ratio of 2. After a quarter period of an oscillation along the weakly confined dimension, $\frac{1}{4}T_z$, condensate atoms reach the center of the potential simultaneously giving rise to the delta-function momentum distribution of a condensate. The thermal component is shown to contract with the condensate, which does happen for thermal atoms displaced by the condensate mean-field. But for hot thermal atoms, the width of the distribution should have approximately the same size in coordinate and momentum space.

7.2.1 Spatial Separation Between Lattice Sites

The dominant anharmonic term in our potential is of order zr^2. This means that at different positions directly below the trap, the frequency in the radial plane is shifted. For a 3D experiment, this effect is washed out by oscillations along $\hat{z}$, however if atoms are confined to distinct planes, which are separated in $\hat{z}$, then the anharmonic shift vanishes within each plane but the radial trap frequency is different between planes. Slosh oscillations will eventually dephase between sites and eventually the condensates on each site will be spatially separated in the radial plane, as shown in Fig. 7.6. An example of this dephasing can be seen from the data in Fig. 7.7, where small differences in the slosh phase make the total cloud appear tilted. COM separations that are larger than the condensate diameters allow each condensate to be imaged separately, but require long evolution times with our normal trap settings. Our magnetic trap is configured so that the radial trap frequency is 10

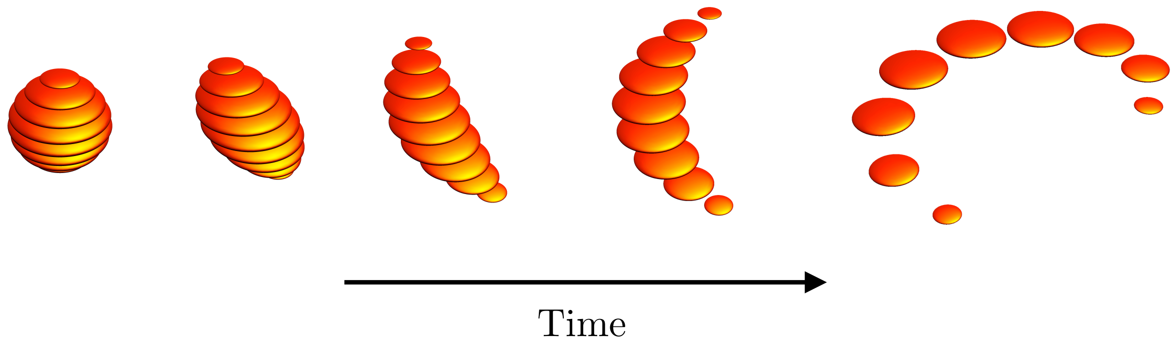

Figure 7.6: Example of intersite dephasing for multiple quasi-2D condensates confined to a 1D optical lattice. Individual layers, viewed from the side, are not resolved. Instead, the entire sample appears "tilted" as the separate vertical layers become slightly offset from each other in the horizontal direction.

Hz, with an intersite frequency difference of $\Delta f = 0.0032Hz$. Waiting for the clouds to fully separate takes nearly a minute in the standard trap configuration. However, the amount of dephasing can be turned up by enhancing the strength of the zr^2 term. By decreasing the TOP bias field strength from 7.4 G to 1 G, the radial trap frequency increases to 19 Hz with an intersite frequency difference of $\Delta f = 0.074Hz$. Such a significant reduction in the strength of the TOP bias field would normally cause a number of issues, such as vertical slosh, or inadvertantly evaporating the cloud because of the small size of the circle of death. But, when the atoms are confined to a lattice, this adjustment can be made very quickly and without having to worry about these problems. Because we want to anharmonically shear the cloud and then let the condensates evolve freely with minimal intersite dephasing, we temporarily ramp the TOP field while the cloud is sloshing, and return the field strength to its original setting before taking data. Fig. 7.8 shows data taken after 2 seconds of evolution in a trap where the TOP field had been reduced to 1 G. In this alternate configuration of the trap, the intersite dephasing has increased by more than a factor of 20 and separate layers can be resolved.

Once the cloud has fully separated, we are able to increase the amount of data acquired

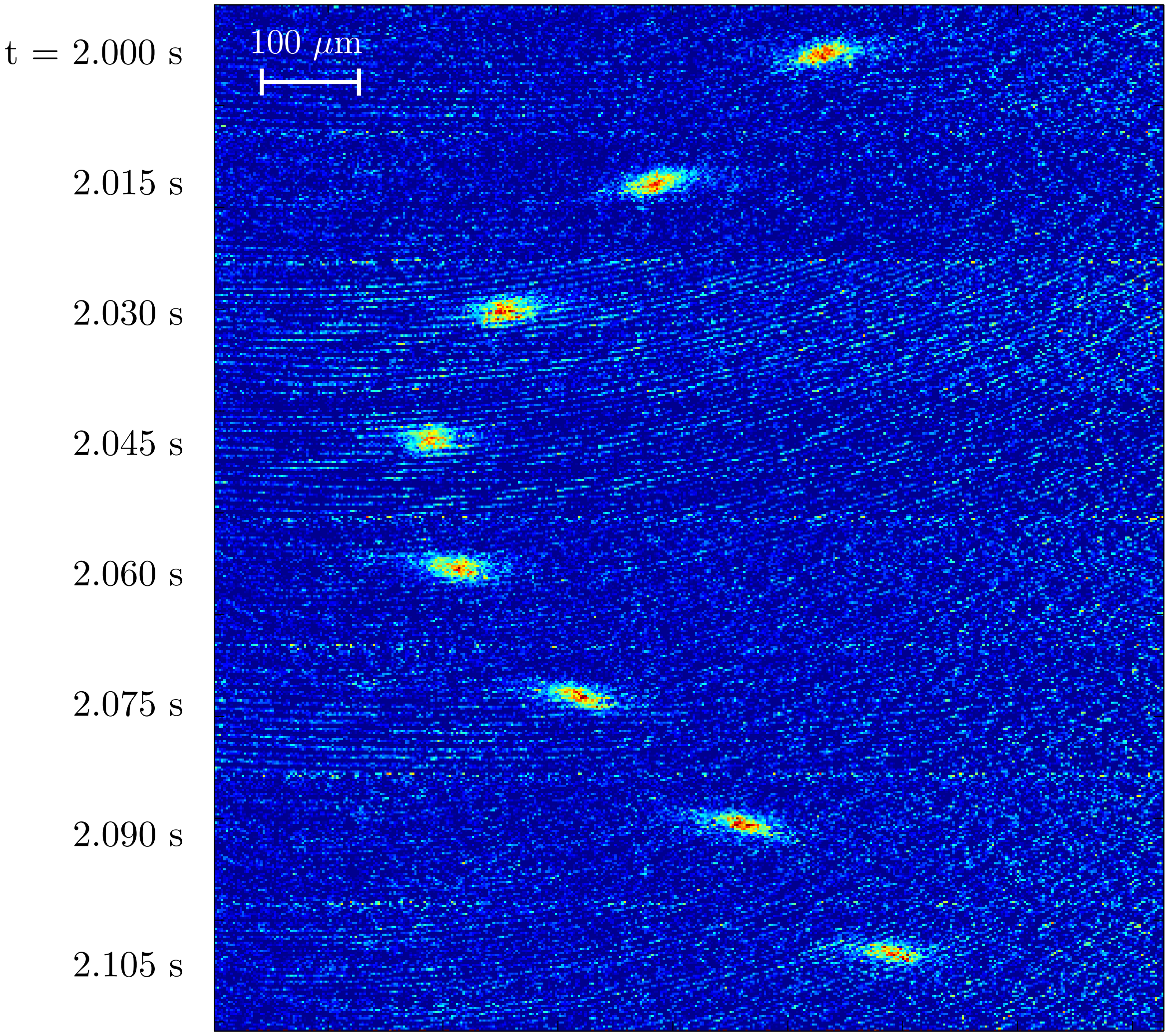

Figure 7.7: Side-view image of intersite dephasing for multiple quasi-2D condensates after a two seconds.

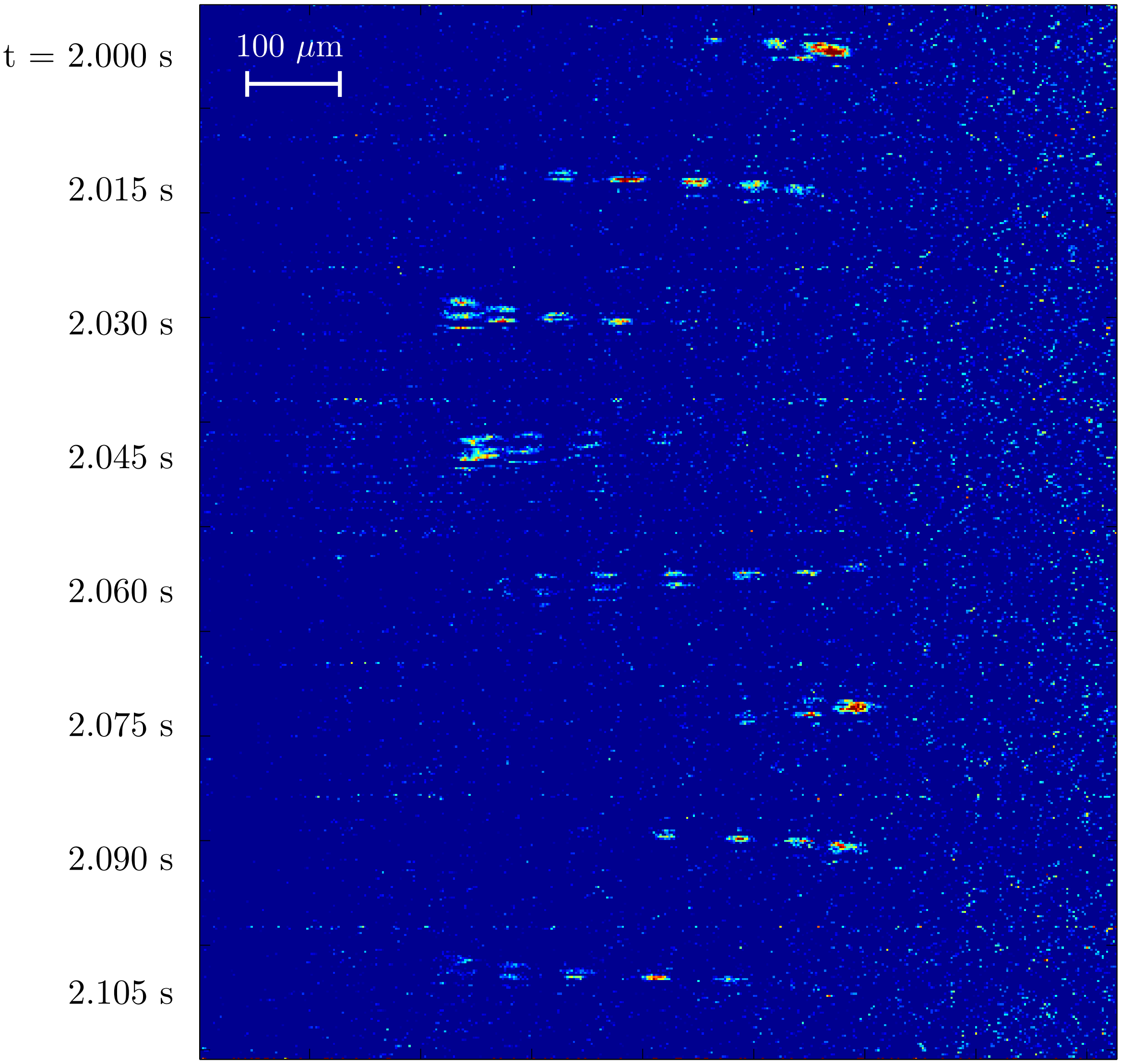

Figure 7.8: Side-view image of intersite dephasing for multiple quasi-2D condensates after two seconds with a TOP field of 1 G, where layers have been fully separated. Separate layers can be resolved, but imaging from the side causes the probe beam to diffract when incident on a condensate, making the individual layers difficult to resolve. The condensates are sloshing in a circular motion, and at different phases of the oscillation the clouds appear to overlap when viewed from the side.

in a single shot by simultaneously imaging all of the layers in the lattice. Because we are not limited to imaging 10% of the cloud, the signal is much larger allowing us to use phase-contrast imaging. Of course, the phase-contrast images shown from the side don't provide a nice source of data. Diffraction from the thin layers can overlap with other layers, and the phase of the oscillations can obscure the measured widths of clouds that are closely aligned along the direction of our imaging beam. Similar issues can arise when imaging from the top, where the individual phases of slosh in each site causes the clouds to overlap.

By driving the slosh mode in a circular motion, the individual slosh oscillations in each lattice site would begin to dephase in such a way that their radial positions don't overlap at any given phase during an oscillation, as depicted in Fig. 7.6. After the cloud has fully separated, the TOP field is ramped back to its initial value of 7.4 G and the intersite dephasing is reduced. Returning the trap to its original parameters also lets us optimize the roundness of the trap at a setting where the intersite dephasing is small enough to allow for much longer evolution times. One issue that can arise during the dephasing process is a change in the isotropy in the radial plane of the trap. In this case, Lissajous patterns start to appear and the final orientation of the clouds depends on the individual phases of sloshing along the two principal axes. For example, if dephasing along the two principal axes is such that the oscillations become linear, then linear slosh motion will persist once the trap has been has been returned to its original configuration. The easiest way to account for this is by varying the evolution time during the anharmonic shearing process such that the cloud trajectories are circular upon ramping the TOP field to the standard setting. In this case, it is actually easier to ramp only the TOP fields without any adjustment to the elliptifier field strength during shearing. This provides a slightly more anisotropic trap as the cloud separates and allows for more controlled adjustement of the final slosh trajectories.

Fig. 7.9 shows some sample images of the cloud as viewed from the top, after the cloud has been anharmonically sheared. In these data, we were measuring the monopole frequency in a 2D cloud, which could be directly compared with the frequency of the slosh mode resulting from the anharmonic shearing.

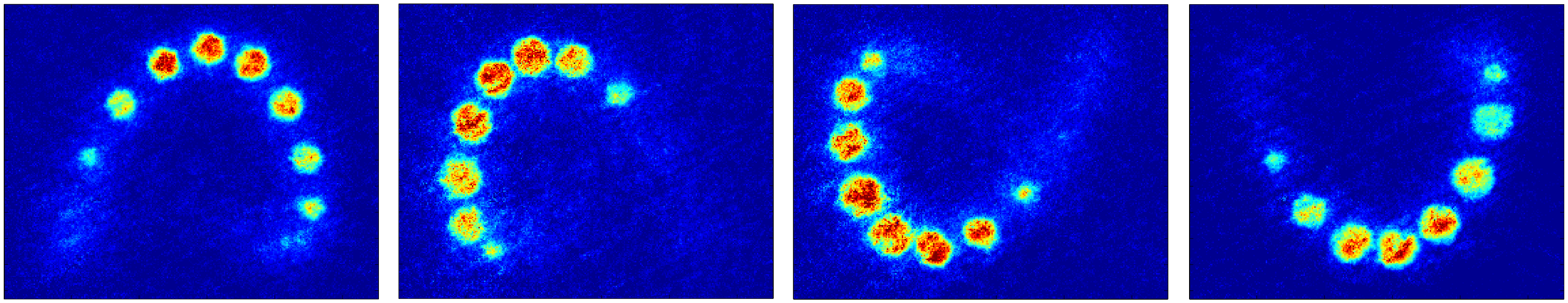

Figure 7.9: Raw data from an experimental realization of the anharmonic shearing effect viewed from the TOP. These data are taken after 2 seconds of evolution in the sheared trap, and are taken in 20 ms intervals.

This anharmonic shearing technique provides a useful method of probing multiple quasi-2D condensates simultaneously without having to worry about the signal being obstructed by their overlap. Data acquisition rates can be sped up dramatically because phase-contrast imaging can be used, and measurements on multiple condensates can be made in a single image. We developed this technique to measure a small, expected shift in the monopole frequency in 2D from a quantum anomaly [44]. However, we did not end up using this approach because we worried that the frequency shift of the monopole mode, which was expected to be 0.1% in our system, would be obscured by any residual parametric driving of the cloud due to any slight asymmetry in our lattice beams.

Bibliography

[1] Data received from Cameron Straatsma.

[2] M H Anderson, J R Ensher, M R Matthews, C E Wieman, and E A Cornell. Observation of bose-einstein condensation in a dilute atomic vapor. Science (New York, N.Y.), 269(5221):198–201, 1995.

[3] M. R. Andrews, D. M. Kurn, H.-J. Miesner, D. S. Durfee, C. G. Townsend, S. Inouye, and W. Ketterle. Propagation of sound in a bose-einstein condensate. Phys. Rev. Lett., 79:553–556, Jul 1997.

[4] M. Badino. Mechanistic slumber vs. statistical insomnia: the early history of Boltzmanns H-theorem (18681877). The European Physical Journal H, 36(3):353–378, October 2011.

[5] T. Bergeman, Gidon Erez, and Harold J. Metcalf. Magnetostatic trapping fields for neutral atoms. Phys. Rev. A, 35:1535–1546, Feb 1987.

[6] Immanuel Bloch. Ultracold quantum gases in optical lattices. Nature Physics, 1(1):23–30, 2005.

[7] L. Boltzmann. ber die Aufstellung und Integration der Gleichungen, welche die Molekularbewegung in Gasen bestimmen. Sitzungsberichte der Akademie der Wissenschaften, Wien, 74:503–552, 1876.

[8] Ludwig Boltzmann. Theoretical physics and philosophical problems : selected writings. Reidel Pub. Co, Dordrecht Boston, 1974.

[9] Ludwig Boltzmann. Lectures on Gas Theory. Dover Publications, City, 2012.

[10] HJ Briegel, T Calarco, D Jaksch, JI Cirac, and P Zoller. Quantum computing with neutral atoms. JOURNAL OF MODERN OPTICS, 47(2-3):415–451, FEB-MAR 2000.

[11] Stephen G . Brush. History of the Kinetic Theory of Gases. pages 1–31.

[12] Ch. Buggle, P. Pedri, W. von Klitzing, and J. Walraven. Shape oscillations in nondegenerate Bose gases: Transition from the collisionless to the hydrodynamic regime. Physical Review A, 72(4):043610, October 2005.

[13] Carlo Cercignani. The Boltzmann Equation and its Applications. Springer-Verlag, New York, 1988.

[14] Carlo Cercignani. Ludwig Boltzmann the man who trusted atoms. Oxford University Press, Oxford, 2006.

[15] F. Chevy, V. Bretin, P. Rosenbusch, K. Madison, and J. Dalibard. Transverse Breathing Mode of an Elongated Bose-Einstein Condensate. Physical Review Letters, 88(25):250402, June 2002.

[16] Kristan L. Corwin, Zheng-Tian Lu, Carter F. Hand, Ryan J. Epstein, and Carl E. Wieman. Frequency-stabilized diode laser with the zeeman shift in an atomic vapor. Appl. Opt., 37(15):3295–3298, May 1998.

[17] F. Dalfovo, S. Giorgini, L. P. Pitaevskii, and S. Stringari. Theory of Bose-Einstein condensation in trapped gases. Review of Modern Physics, 71(3):69, 1999.

[18] Olivier Darrigol. From c-numbers to q-numbers : the classical analogy in the history of quantum theory. University of California Press, Berkeley, 1992.

[19] Wolfgang Dreyer, Wolfgang H. Müller, and Wolf Weiss. Tales of Thermodynamics and Obscure Applications of the Second Law. Continuum Mechanics and Thermodynamics, 12(3):151–184, June 2000.

[20] Jason Remington Ensher. The First Experiments with Bose-Einstein Condensation of ^{87}Rb. PhD thesis, University of Colorado, Boulder, 1998.

[21] Tilman Esslinger, Immanuel Bloch, and Theodor Hänsch. Bose-Einstein condensation in a quadrupole-Ioffe-configuration trap. Physical Review A, 58(4):R2664–R2667, 1998.

[22] Matthew P a Fisher, Peter B Weichman, J Watson, and Daniel S Fisher. Boson localization. Physical Review, 40(1), 1989.

[23] Herbert Goldstein. Classical mechanics. Addison-Wesley Pub. Co, Reading, Mass, 1980.

[24] Markus Greiner, Olaf Mandel, Tilman Esslinger, Theodor W Hänsch, and Immanuel Bloch. Quantum phase transition from a superfluid to a Mott insulator in a gas of ultracold atoms. Nature, 415(6867):39–44, 2002.

[25] R Grimm, M Weidemuller, and YB Ovchinnikov. Optical dipole traps for neutral atoms. In ADVANCES IN ATOMIC MOLECULAR, AND OPTICAL PHYSICS, VOL. 42, volume 42 of ADVANCES IN ATOMIC MOLECULAR AND OPTICAL PHYSICS, pages 95–170. ACADEMIC PRESS INC, 525 B STREET, SUITE 1900, SAN DIEGO, CA 92101-4495 USA, 2000.

[26] D. Guéry-Odelin. Mean-field effects in a trapped gas. Physical Review A, 66(3):033613, September 2002.

[27] D. Guéry-Odelin, J. G. Muga, M. J. Ruiz-Montero, and E. Trizac. Nonequilibrium Solutions of the Boltzmann Equation Under the Action of an External Force. Physical Review Letters, 112(18):1–5, 2014.

[28] D. Guéry-Odelin, J. G. Muga, M. J. Ruiz-Montero, and E. Trizac. Nonequilibrium solutions of the boltzmann equation under the action of an external force. Phys. Rev. Lett., 112:180602, May 2014.

[29] David Guery-Odelin, Francesca Zambelli, Jean Dalibard, and Sandro Stringari. Collective oscillations of a classical gas confined in harmonic traps. Physical Review A, 60(6):4851–4856, 1999.

[30] P C Haljan, I Coddington, P Engels, and E A Cornell. Driving Bose-Einstein-condensate vorticity with a rotating normal cloud. Physical review letters, 87(21):210403, 2001.

[31] Paul C Haljan. Vortices in a Bose-Einstein Condensate. PhD thesis, University of Colorado, Boulder, 2003.

[32] E. Hodby, G. Hechenblaikner, O. M. Marago', J. Arlt, S. Hopkins, and C. J. Foot. Bose-Einstein condensation in a stiff TOP trap with adjustable geometry. page 4, 2000.

[33] Kerson Huang. Statistical mechanics. Wiley, New York, 1987.

[34] B. Jackson and C. Adams. Damping and revivals of collective oscillations in a finite-temperature model of trapped Bose-Einstein condensation. Physical Review A, 63(5):053606, April 2001.

[35] D. Jaksch, C. Bruder, J. I. Cirac, C. W. Gardiner, and P. Zoller. Cold bosonic atoms in optical lattices. page 4, 1998.

[36] Toshiya Kinoshita, Trevor Wenger, and David S. Weiss. A quantum newton's cradle. Nature, 440(7086):900–903, 04 2006.

[37] H J Lewandowski. Coherences and correlations in an ultracold Bose gas. PhD thesis, University of Colorado, Boulder, 2002.

[38] David Lindley. Boltzmann's atom : the great debate that launched a revolution in physics. Free Press, New York, 2001.

[39] Daniel Lobser, Andrew E. Barentine, Heather J. Lewandowski, and Eric A. Cornell. (in preparation).

[40] Michael Robin Matthews. Two-Component Bose-Einstein Condensation. PhD thesis, University of Colorado, Boulder, 1999.

[41] Alan L. Migdall, John V. Prodan, William D. Phillips, Thomas H. Bergeman, and Harold J. Metcalf. First observation of magnetically trapped neutral atoms. Phys. Rev. Lett., 54:2596–2599, Jun 1985.

[42] Aspasia S. Moue. The Thought Experiment of Maxwells Demon and the Origin of Irreversibility. Journal for General Philosophy of Science, 39(1):69–84, July 2008.

[43] C. J. Myatt, N. R. Newbury, R. W. Ghrist, S. Loutzenhiser, and C. E. Wieman. Multiply loaded magneto-optical trap. Opt. Lett., 21(4):290–292, Feb 1996.

[44] Maxim Olshanii, Hélène Perrin, and Vincent Lorent. Example of a quantum anomaly in the physics of ultracold gases. Physical Review Letters, 105(9):5, 2010.

[45] Wolfgang Petrich, Michael H. Anderson, Jason R. Ensher, and Eric A. Cornell. Stable, Tightly Confining Magnetic Trap for Evaporative Cooling of Neutral Atoms. Physical Review Letters, 74(17):0–3, 1995.

[46] L. P. Pitaevskii. Bose-Einstein condensation. Clarendon Press, Oxford New York, 2003.

[47] Noelle Pottier. Nonequilibrium statistical physics : linear irreversible processes. Oxford University Press, Oxford, 2010.

[48] David E. Pritchard. Cooling neutral atoms in a magnetic trap for precision spectroscopy. Phys. Rev. Lett., 51:1336–1339, Oct 1983.

[49] Nick P Proukakis and Brian Jackson. Finite-temperature models of BoseEinstein condensation. Journal of Physics B: Atomic, Molecular and Optical Physics, 41(20):203002, October 2008.

[50] E. L. Raab, M. Prentiss, Alex Cable, Steven Chu, and D. E. Pritchard. Trapping of neutral sodium atoms with radiation pressure. Phys. Rev. Lett., 59:2631–2634, Dec 1987.

[51] Anand Ramanathan, Sérgio R. Muniz, Kevin C. Wright, Russell P. Anderson, William D. Phillips, Kristian Helmerson, and Gretchen K. Campbell. Partial-transfer absorption imaging: A versatile technique for optimal imaging of ultracold gases. Review of Scientific Instruments, 83(8), 2012.

[52] Steffen P. Rath, Tarik Yefsah, Kenneth J. Günter, Marc Cheneau, Rémi Desbuquois, Markus Holzmann, Werner Krauth, and Jean Dalibard. Equilibrium state of a trapped two-dimensional Bose gas. Physical Review A - Atomic, Molecular, and Optical Physics, 82(1):2–6, 2010.

[53] M. Rusch, S. a. Morgan, D. a W Hutchinson, and K. Burnett. Second order theory of excitations in trapped Bose condensates at finite temperatures. Physical Review Letters, 85(23):4844–4847, 2000.

[54] D. Rychtarik, B. Engeser, H. C. Nägerl, and R. Grimm. Two-dimensional Bose-Einstein condensate in an optical surface trap. Physical Review Letters, 92(17):173003–1, 2004.

[55] I Shvarchuck, Ch Buggle, D S Petrov, K Dieckmann, M Zielonkowski, M Kemmann, T G Tiecke, W von Klitzing, G V Shlyapnikov, and J T M Walraven. Bose-Einstein condensation into nonequilibrium States studied by condensate focusing. Physical Review Letters, 89(27):270404, 2002.

[56] N. L. Smith, W. H. Heathcote, G. Hechenblaikner, E. Nugent, and C. J. Foot. Quasi-2D Confinement of a BEC in a Combined Optical and Magnetic Potential. 223:11, 2004.

[57] Vincent S. Steckline. Zermelo, Boltzmann, and the recurrence paradox. Am. J. Phys., 51(10), 1983.

[58] William Thomson. Kinetic Theory of the Dissipation of Energy. Nature, 9:441–444, 1874.

[59] Stephen Thornton. Classical dynamics of particles and systems. Brooks/Cole, Belmont, CA, 2004.

[60] S. Tung, G. Lamporesi, D. Lobser, L. Xia, and E. a. Cornell. Observation of the presuperfluid regime in a two-dimensional bose gas. Physical Review Letters, 105(23):1–4, 2010.

[61] Shih-Kuang Tung. Probing an interacting Bose gas in a quasi-two-dimensional trap. PhD thesis, University of Colorado, Boulder, 2010.

[62] G. E. Uhlenbeck and G. W. Ford. Lectures in Statistical Mechanics. American Mathematical Society, Providence, RI, 1963.

[63] J. Williams and a. Griffin. Damping of condensate collective modes due to equilibration with the noncondensate. Physical Review A, 63(2):023612, January 2001.

Appendix A

Finite Temperature Data

$N_0/N = 0.098(2)$

t (ms)	$\langle S \rangle$ (μm)
234.5	7.1(7)
1034.5	6.0(3)
634.5	3.0(2)
42.5	7.0(2)
434.5	6.0(2)
834.5	4.0(1)
134.5	4.0(1)
1234.5	0.7(4)
534.5	3.0(2)
934.5	4.0(1)
334.5	5.0(2)
734.5	3.4(3)
1134.5	2.0(3)
134.5	5.0(3)
1234.5	5.0(3)
434.5	1.0(3)
1034.5	5.0(1)
634.5	1.6(9)
42.5	10.0(1)
1134.5	5.0(2)
734.5	3.7(2)
334.5	3.0(3)
834.5	3.0(1)
234.5	7.4(6)
534.5	2.9(10)
934.5	2.0(2)
434.5	3.0(2)
1234.5	3.0(2)

$N_0/N = 0.177(2)$

t (ms)	$\langle S \rangle$ (μm)
42.5	9.0(2)
434.5	2.0(1)
834.5	4.0(2)
234.5	5.0(1)
534.5	3.0(1)
734.5	5.4(3)
1034.5	4.0(1)
134.5	5.8(10)
634.5	3.0(1)
934.5	4.0(1)
334.5	3.0(1)
234.5	5.1(4)
734.5	6.0(2)
42.5	7.0(1)
434.5	3.0(2)
1034.5	3.0(1)
634.5	3.6(4)
134.5	6.0(2)
834.5	4.0(2)
334.5	2.0(2)
534.5	5.0(2)
734.5	3.5(9)
934.5	3.0(3)
434.5	2.0(1)
834.5	2.0(2)
134.5	6.0(2)
534.5	3.0(1)
42.5	9.0(1)
634.5	3.1(7)
334.5	1.0(3)
934.5	4.0(1)
234.5	5.0(2)
1034.5	4.0(2)
534.5	3.0(2)
334.5	1.6(10)
734.5	4.0(2)
1034.5	2.9(6)
734.5	3.8(9)

$N_0/N = 0.31(2)$

t (ms)	$\langle S \rangle$ (μm)
164.5	5.0(3)
834.5	1.0(1)
434.5	3.0(1)
64.5	5.2(7)
1034.5	1.8(8)
164.5	6.0(1)
434.5	4.0(1)
834.5	2.0(1)
64.5	4.4(10)
1034.5	0.8(10)
164.5	5.0(2)
434.5	1.7(8)
834.5	2.7(2)
64.5	6.0(1)
634.5	3.4(10)
1234.5	3.0(8)
434.5	2.0(1)
634.5	3.4(4)
1234.5	2.1(9)
1434.5	3.4(2)
634.5	3.0(1)
1234.5	1.1(6)
1434.5	1.6(3)
1634.5	2.0(2)
1834.5	1.8(4)
1634.5	0.8(7)
2034.5	1.2(3)
1834.5	0.5(7)
1434.5	3.1(9)
2034.5	0.9(3)
634.5	4.5(7)
1634.5	1.6(6)
434.5	2.0(1)
834.5	4.0(1)
164.5	7.0(2)

$N_0/N = 0.322(3)$

t (ms)	$\langle S \rangle$ (μm)
42.5	9.0(2)
434.5	1.0(2)
1034.5	3.0(9)
734.5	2.4(9)
134.5	6.0(1)
534.5	2.0(2)
334.5	1.0(2)
934.5	0.9(5)
234.5	6.0(2)
634.5	3.1(8)
1134.5	1.0(1)
834.5	2.0(6)
434.5	2.0(2)
234.5	3.0(1)
634.5	2.0(1)
334.5	2.0(1)
1034.5	2.5(8)
42.5	8.0(1)
1134.5	3.0(1)
734.5	3.1(6)
134.5	6.0(2)
834.5	1.0(1)
934.5	2.0(1)
534.5	4.2(6)
1034.5	2.0(1)

$N_0/N = 0.322(3)$ (cont'd)

t (ms)	$\langle S \rangle$ (μm)
134.5	4.4(8)
334.5	0.3(7)
734.5	3.6(7)
42.5	7.0(1)
234.5	4.0(2)
1134.5	3.0(2)
834.5	1.0(1)
234.5	4.6(8)
434.5	2.5(9)
434.5	1.7(10)
634.5	3.0(1)
934.5	0.8(7)
534.5	1.0(2)
834.5	2.0(1)
334.5	2.0(2)
1134.5	2.0(1)
734.5	2.4(8)
42.5	6.7(9)
634.5	2.0(1)
534.5	3.0(1)
1034.5	1.4(8)
134.5	5.0(2)
234.5	5.0(2)

$N_0/N = 0.446(2)$

t (ms)	$\langle S \rangle$ (μm)
334.5	1.0(3)
834.5	1.6(9)
234.5	5.0(1)
434.5	3.0(1)
634.5	4.9(7)
134.5	6.0(1)
734.5	5.0(1)
534.5	2.0(2)
42.5	7.0(1)
334.5	2.0(2)
734.5	2.4(3)
134.5	7.0(3)
534.5	1.0(1)
834.5	0.0(1)
234.5	4.0(1)
634.5	3.3(9)
434.5	0.0(2)
42.5	9.0(2)
734.5	1.0(1)
334.5	1.0(2)
134.5	7.6(6)
834.5	2.0(1)
534.5	7.0(3)
234.5	5.0(1)
634.5	2.0(2)
434.5	3.0(1)
42.5	10.0(2)
734.5	5.0(9)
534.5	3.0(2)
534.5	4.0(1)
634.5	4.0(1)

$N_0/N = 0.579(3)$

t (ms)	$\langle S \rangle$ (μm)
232	2.7(7)
624	3.0(1)
17	10.0(1)
1317	0.5(8)
417	3.6(9)
917	3.3(8)
117	7.2(4)
717	2.0(1)
1117	4.0(1)
317	2.7(8)
1817	0.2(8)
517	4.8(8)
1017	2.0(1)
617	4.6(6)
1217	2.5(7)
17	11.0(2)
717	3.5(6)
417	1.0(1)
1117	3.0(1)
217	4.62(6)
817	3.2(5)
624	4.0(1)
117	6.6(7)
1317	3.1(5)
317	4.0(1)
917	1.0(10)
517	0.6(3)
817	2.7(7)
1817	2.0(2)
1017	1.9(9)
1217	2.2(10)

$N_0/N = 0.583(4)$

t (ms)	$\langle S \rangle$ (μm)
117	8.3(7)
717	2.0(9)
1017	1.0(1)
317	2.3(2)
17	8.0(2)
617	3.7(9)
917	3.0(1)
217	6.4(4)
817	1.0(5)
417	0.0(1)
517	3.9(6)
267	3.2(4)
967	1.5(5)
567	6.0(1)
67	6.5(10)
867	2.2(4)
467	3.6(5)
167	6.0(1)
167	5.2(3)
667	4.0(1)
367	3.3(5)
767	2.2(5)
617	4.0(1)
117	8.2(8)
1017	3.4(6)
417	2.0(1)

$N_0/N = 0.583(4)$ (cont'd)

t (ms)	$\langle S \rangle$ (μm)
717	3.0(1)
17	9.0(2)
567	4.4(3)
217	5.0(2)
917	2.5(8)
367	3.2(7)
67	7.0(1)
817	2.0(2)
517	2.7(3)
1017	2.5(9)
317	3.0(4)
667	5.0(1)
867	2.6(9)
267	6.0(2)
967	2.0(1)
467	2.7(5)
567	2.0(1)
267	4.1(7)
417	1.8(5)
767	2.9(7)
267	5.0(1)
567	2.0(1)
1017	2.9(10)
567	2.8(9)
667	4.0(8)